Theses and Dissertations

Graduate School

2016

The Dawn of New Quantum Dots: Synthesis and Characterization of Ge1-xSnx Nanocrystals for Tunable Bandgaps.

Richard J. Esteves
Virginia Commonwealth University

The Dawn of New Quantum Dots: Synthesis and Characterization of $Ge_{1-x}Sn_x$ Nanocrystals for Tunable Bandgaps.

A dissertation submitted in partial fulfillment of the requirements for the degree of Doctor of Philosophy at Virginia Commonwealth University.

by

Richard J Alan Esteves

Advisor: Indika U. Arachchige

Assistant Professor, Department of Chemistry

Virginia Commonwealth University

Richmond Virginia, 23284-2006

United States

ACKNOWLEDGEMENTS

The achievements of any individual are, by and large always a group effort. When we see a beautifully designed building, it is only right that credit is given to the architect that painstakingly designed and oversaw its construction. However, the architect's success would be non-existent if not for the people surrounding them. First on the list of people responsible is the person who commissioned the building, without this the building never even exists. Then more existentially, is everyone who help to shape the architect to be the person they are; including their kindergarten teacher who provided the building blocks for curiosity, the parents who nurtured and supported, and the friends who lifted up or beat down every decision ever made by the architect, and every person in-between. Every colleague that help check the designs, the contractors that translated ink on paper to a tangible structure, all the administrators that enable the flow of material, and even the inspectors and officials that seemly did everything possible to hinder the easy and simple construction of the building, only to ensure the best possible outcome. The purpose for this metaphor to convey that I owe everything I have accomplished to a vast group of people from the most important figure in my life, to some whom I only briefly met, and very possibly many who I never even personally crossed paths with. So, if you are reading this and not mentioned directly I would like to say thank you.

To simply thank my parents for their love and support would be an insult to the colossal effort they dedicated to mold and shape me into the person I am today. From an early age my parents recognized my potential and encouraged my development in the realms of science, and helped me to develop a desire to push myself to the limits of my

capabilities and grow. This last bit is almost essential to pursue a Ph.D. and pushing the boundaries of scientific knowledge by even a minuscule amount. My siblings had a strong role in raising me as well, as my parents worked hard every day my sister became a major part of my upbringing. She helped keep track of both my brother and myself, was an excellent caregiver and sometimes had to enforce the rules when it came to homework. My brother was the guiding force for all my hobbies, thinking about it now I must have been an incredibly annoying little brother. From TV shows and video games to sports and Boy Scouts I followed him through all of it. With all that time I spent with him he was able to impart in me many values that I still live by today. Without the influence of each of these people in my life I may never have developed the fortitude to survive the trials that graduate school put me through. "In addition to my family, I must also give credit to all the wonderful mentors that we both interacted with along the way. First and foremost are my Scout leaders throughout the years, Ilene Potoak, Karen and Ed Henses, and the indelible late Doctor Allen Schwartz, all of which taught me more than even some of my most influential teachers. To truly, express my level of gratitude to these amazing people would take far more than the paper and ink this shall be printed on. Next I must mention my Tae Kwon Do instructors, Master Geovany Rayo, Master Lourdes Rayo, and the late Master Agustin Rayo of Lighting Warrior Tae Kwon Do in North Haldon NJ, as well as Senior Chief Master Ismael Aponte who trained all three of the Rayo siblings, my brother and myself. They taught me strength, fortitude and discipline and are some of the most incredibly role models I have ever known.

I consider myself incredibly lucky with regard to the path I have taken through graduate school. If someone were to ask me for advice on selecting a graduate school

for research, I would tell someone to not only consider the school and facilities but to take a close look at the potential research advisors. A bad match of student and advisor or a lack of any interesting topics can easily make for a terrible time in graduate school. I had none of this advice, I applied to VCU almost completely blindly. When I first met with Dr. Indika Arachchige I was instantly interested in the $Ge_{1-x}Sn_x$ project and after I fulfilled my duty of checking out enough other professors I immediately scheduled another appointment. I knew that I wanted to be on this project developing a completely new material, and I knew I wanted the rare experience of getting to help build and start up a lab. I can still remember the look of surprise on Dr. Arachchige's face when I sat down and told him right off that bat that I wanted to join his group and I am incredibly thankful that he said yes. From the very beginning Dr. Arachchige has provided an insurmountable amount of guidance, and as my knowledge expanded he always listened to my ideas and either encouraged me to pursue or advised me to not stray out of our main focus. The result is what I believe to be a very strong relationship based on mutual respect. Dr. Arachchige has afforded me more experience than I could have ever expected to gain in graduate school tenure which I intend to take with me through the rest of my life.

Last but not at all least I must thank all my academic peers and friends that I have made along the way. First and foremost is one of my best friends and greatest rivals in life Ms. Heather Boyce, with whom I have developed an unbreakable amount of respect for throughout our quest of knowledge and success. She made endless lab reports and all night study sessions enjoyable through our tireless debating and bickering. Even while we were both pursuing Ph. D's in different fields and in different cities she has always made time to help proofread or help me check my work. My lab mates have also been

invaluable throughout my graduate school career. Both Lamia Nahar M.S. and Dr. Xiaonan Gao have been with me from the very beginning; sharing lab responsibilities, checking each other's work, preparing for presentations and providing guidance in research. Dr. Kulugammana Ranmohotii, a postdoc in our group was a great influence for me early in my graduate career, he worked efficiently and also had elegant presentation skills, setting a great example for me to live up to. One of the more recent additions to our lab, Venkatesh Tallapally and I recently co-authored a very satisfying paper thanks to countless hours of work he put in. I wish great luck to the two newest members of the lab Ebtesam Ealdgham and Dilhara Liyange, who will be following up on my work with $Ge_{1-x}Sn_x$ and hope they can take it further than I ever could.

There are many people who I have not mentioned, I have not forgotten you but at this rate if I do not conclude I won't finish in time to graduate. So thank you to any and all who have ever helped me along the way. If you are ever in need I will gladly return the favor.

TABLE OF CONTENTS

List of Figures

List of Tables

ABSTRACT

The Dawn of New Quantum Dots: Synthesis and Characterization of $Ge_{1-x}Sn_x$ Nanocrystals for Tunable Bandgaps.

by

Richard J Alan Esteves

A dissertation submitted in partial fulfillment of the requirements for the degree of Doctor of Philosophy at Virginia Commonwealth University.

Advisor: Indika U. Arachchige

Assistant Professor, Department of Chemistry

$Ge_{1-x}Sn_x$ alloys are among a small class of benign semiconductors with composition tunable bandgaps in the near-infrared spectrum. As the amount of Sn is increased the band energy decreases and a transition from indirect to direct band structure occurs. Hence, they are prime candidates for fabrication of Si-compatible electronic and photonic devices, field effect transistors, and novel charge storage device applications. Success has been achieved with the growth of $Ge_{1-x}Sn_x$ thin film alloys with Sn compositions up to 34%. However, the synthesis of nanocrystalline alloys has proven difficult due to larger discrepancies (~14%) in lattice constants. Moreover, little is known about the chemical factors that govern the growth of $Ge_{1-x}Sn_x$ nanoalloys and the

effects of quantum confinement on structure and optical properties. A synthesis has been developed to produce phase pure $Ge_{1-x}Sn_x$ nanoalloys which provides control over both size and composition. Three sets of $Ge_{1-x}Sn_x$ nanocrystals have been studied, 15–23 nm, 3.4–4.6 nm and 1.5–2.5 nm with Sn compositions from x = 0.000–0.279. Synthetic parameters were explored to control the nucleation and growth as well as the factors that have led to the elimination of undesired metallic impurities. The structural analysis of all nanocrystals suggests the diamond cubic structure typically reported for $Ge_{1-x}Sn_x$ thin films and nanocrystalline alloys. As-synthesized $Ge_{1-x}Sn_x$ nanoalloys exhibit high thermal stability and moderate resistance against sintering up to 400–500 °C and are devoid of crystalline and amorphous elemental Sn impurities.

The largest set of nanocrystals (15–23 nm) were useful in determining the compositional dependence on lattice parameters as studied using powder X-ray diffraction and Raman spectroscopy. Systematic expansion of the cubic Ge lattice with increasing Sn composition was confirmed suggesting homogenous distribution of Sn and Ge in the nanocrystals. High resolution scanning transmission electron microscopy energy dispersive spectroscopy elemental maps, support the structural homogeneity and lack of Sn segregation. The next size set (3.4-4.6 nm) revealed quantum size effects and resulted in bandgaps significantly blue shifted from bulk Ge. Tauc analysis suggests indirect energy gaps from 1.31-0.75 eV and direct energy gaps from 1.47-0.95 eV for x = 0.000-0.116 compositions. The third set (1.5-2.5 nm) were studied to elucidate photoluminescence (PL) and push the limits of quantum confinement in $Ge_{1-x}Sn_x$ nanocrystals. The ultra-small $Ge_{1-x}Sn_x$ QDs (1.5-2.5 nm), for the first-time, exhibit energy gaps in the visible spectrum with composition dependent absorption and

emission properties. Solid-state absorption and emission spectra indicate strong confinement effects with absorption onsets ranging from 1.55-2.16 eV and (PL) peak maxima from 1.72-2.05 eV (620-720 nm) for x = 0.018-0.236.7, Ab initio hybrid functional calculations are in close agreement with the experimental results, confirming measured nanocrystal sizes and compositions.

Temperature dependent time resolved PL spectroscopy was utilized to study the carrier dynamics of as-synthesized 1.5-2.5 nm nanocrystals, which suggest slow decay (3 − 27 µs) of PL at 15 K, likely due to slow recombination of spin-forbidden dark excitons and carriers trapped at surface states, and at least one order of magnitude faster recombination with increasing Sn concentration to 23.6 %. Increasing temperature to 295 K led to three orders of magnitude faster decay (9 − 28 ns) owing to the thermal activation of bright excitons and carrier de-trapping from surface states. A possible mechanism for the origin of visible PL has been proposed based on detailed carrier dynamics studies supported by first principle calculations. The versatile synthesis of $Ge_{1-x}Sn_x$ nanocrystals has been achieved with control over size, shape, and composition. Optical studies demonstrated improved light-matter interactions as a function of size and composition making $Ge_{1-x}Sn_x$ nanocrystals promising in visible to near infrared (IR) optoelectronic applications.

CHAPTER 1

INTRODUCTION

The technological revolution that has occurred over the past few decades was made possible by the development of semiconducting transistors. Most prominently, the history of our current technology can be traced back to the first transistor made by Bell labs in 1948.[1] This germanium based device demonstrated the ability to switch a current on and off on demand. The entire device was close in size to a baseball while its modern-day predecessors are smaller than most living cells. Following the first transistor, development research into semiconductors began to explode. The advent of the integrated circuit (IC) came the following decade with the important switch from germanium to silicon coming just a few months after that.[2, 3] From there, the size of transistors decreased exponentially, allowing for more powerful and compact chips. This trend is beautifully explained through Moore's Law which states that the number of transistors on a chip will double roughly every two years.[4] Moore's Law held strong for almost 40 years, and most of those advances were made on the back of doped silicon crystals. In recent years, a point was reached where at the small device size, silicon could no longer maintain its semiconducting behavior.[5] Semiconductor device research is constantly adjusting to avoid disappointing Moore's law.[6] Many new materials and techniques have been explored and implemented, some with great success.[3] However, as the trend of size reduction continues it has become more evident that new

considerations are necessary as our production methods have exceeded the physical and electronic limits of current materials.[5]

Being able to efficiently produce new nanoscale materials has become essential to maintaining the exponential growth of technology. Current nanoscale transistors are most commonly made through lithograph techniques which have many draw backs, such as; limited material types, harsh chemicals, resolution restrictions on feature size, and a top-down production methodology that wastes material.[7] Switching to a bottom-up method of chip assembly can help reduce not only the thickness of the semiconductor junctions but of the entire transistor assembly. This can be accomplished by having a full toolbox of nanomaterials that can then be constructed in any way desired.

1.1   Semiconductors

Semiconductors are a class of materials that have a small to moderate gap between their valance band and conduction band, typically between 0.3 – 3.8 eV.[8] In a simplified sense, a materials bandgap is a function of its buildings blocks, molecular bonding configuration. Every bonded two atom system has electrons distributed through their highest occupied molecular orbitals (HOMO) and lowest unoccupied molecular orbitals (LUMO). The energy levels and spins of these electrons are defined by orbital levels, bonding type and selection rules.[2, 3, 9] As the number of bonded atoms increases, new slightly offset energy levels will be created due to the Pauli exclusion principle.[9] The case of a 'few' atoms bonded will be discussed further in the section 1.3 under quantum confinement.[8] When the number of bonded atoms increases and a certain level of periodicity is reached within an interaction range, the energy levels become so

heavily stacked that each electron pair no longer has a unique quantum number and instead become part of the continuous energy band. The HOMO electrons become the valence band and the LUMO levels become the conduction band. A material's electronic and optical properties are then classified by the gap between the band levels (Figure 1.1).[2, 3, 9]
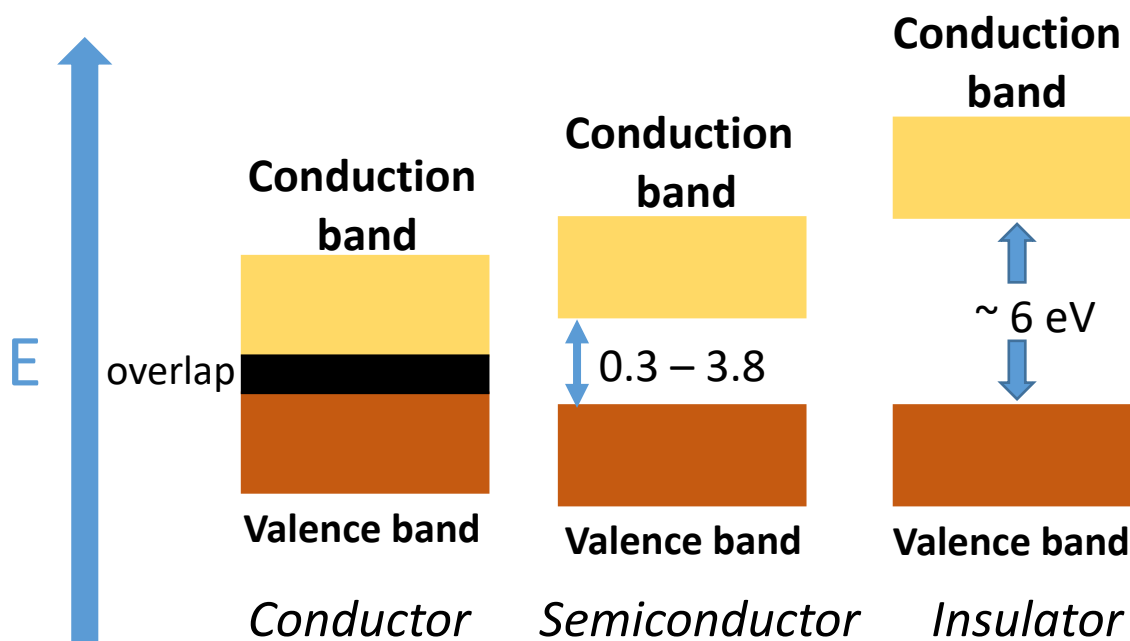
Figure 1.1. Schematic demonstrating the energy gap difference between conductors, semiconductors and insulators, E = Energy.

In the case of metals, the bands overlap and electrons in the valence band can flow freely through the conduction band resulting in a zero bandgap. The partially filled conduction band allows for free flow of electrons giving the material its conductive properties.[3] In a semiconductor, the gap is a defined energetic difference that an electron must first be excited across in order to reach the conduction band. Generating

an excitation across the gap can be achieved through an absorbed photon or an applied current allowing for conduction of a current.[3] When this gap becomes significantly large, the probability of exciting an electron to the conduction band is prohibitively small. A material is considered an insulator when its gap is sufficiently large that they resist conduction even with applied thermal energy or current.[3] Each material type serves an important role in electronic devices and encompasses its own fields of research.

In order for an electron to be excited across the bandgap the incident photon must have an energy higher than the gap. When this condition is met, an electron from the valance band jumps to the conduction band leaving a positively charged hole behind.[8] When incorporated into a circuit, the electron-hole pair can become charge carriers allowing for their extraction for current creation. If the electron-hole pair are not separated they remain in an electrostatically bound state called an exciton. The properties of an exciton have important implications when developing semiconducting devices such as solar panels and LEDs.[10] Excitons have what is referred to as the Bohr radius (a_B), which is the physical distance within the crystal structure that the electron and hole can be separated. That distance is defined by certain material properties and can be characterized by equation 1.1 where ε is the dielectric coefficient, e is the elementary charge m_e^* is the electron mass and m_h^* is the hole mass. [10] Typically, the

$$a_B = \frac{h^2 \varepsilon}{e^2} \left[\frac{1}{m_e^*} + \frac{1}{m_h^*} \right] \tag{1.1}$$

Bohr radius of different materials ranges from 1-100 nm depending on the ε, m_h^* and m_e^*. This must all be considered when designing any semiconductor device to ensure optimal efficiency. In addition, there are two types of semiconductors, direct bandgaps

and indirect bandgaps, with each type being classified by the requirements for photo excitation (Figure 1.2).[2, 3, 8, 9]
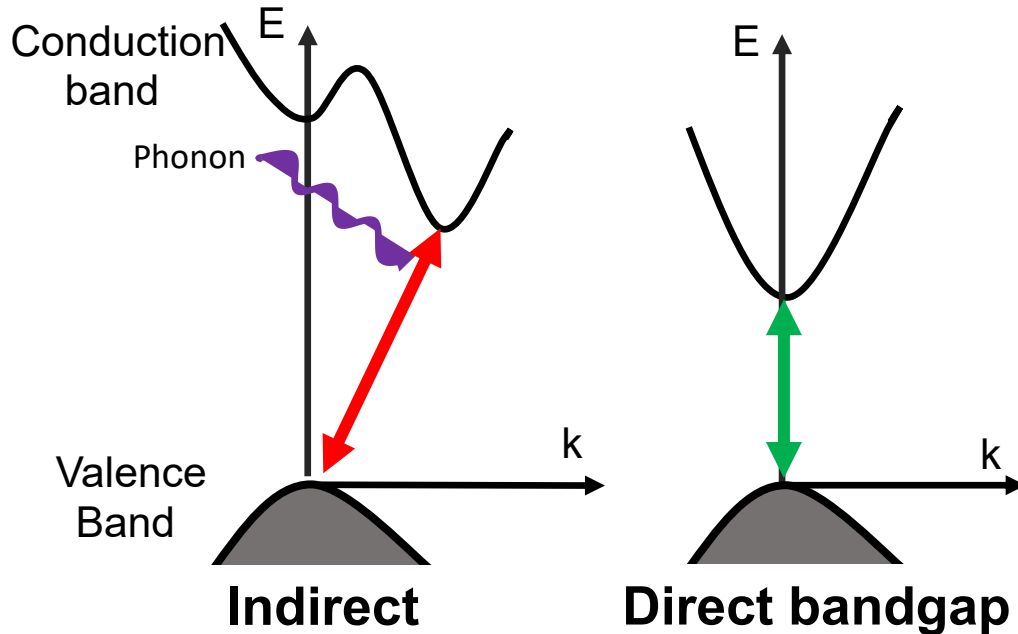
Figure 1.2. Indirect and Direct bandgap structures illustrating the differences in momentum space of the lowest point in the conduction band from the peak of the valence band, E= Energy.

Indirect bandgap semiconductors are typically considered to be less desirable due to the low probability of transitions across the bandgap. The reason for this is based on the alignment of the lowest point in the conduction band being in a different momentum space than the higher point of the valence band.[8, 9] In order to excite an electron across an indirect bandgap, there is a required change in momentum, however since photons do not carry momentum a phonon interaction is required. Phonons are lattice vibrations and in comparisons to incident photons occur in relatively small quantities.[8-10] Combined with the fact a photon and a phonon still have to interact, the

chances of exciting an electron across an indirect bandgap are fairly low relative to that of a direct bandgap. The same applies for the relaxation of an excited electron from the conduction band back down to the valance band.[8-10]

Exciting an electron across a direct bandgap is far simpler in comparison. In a direct bandgap, the lowest point of the conduction band is in the same momentum plane as the highest point in the valance band. Without the need of changing momentum electrons can easily be excited across the gap by any photon on sufficient energy. As such, direct bandgap semiconductors readily absorb incident light, and given the appropriate scenario reemit a photon.[8-10] Examples of both types of semiconductors can be found in Table 1.1.[8]

Table 1.1 Semiconductor Properties and Applications[8]

Compound	Bandgap (eV)	Type*	Structure	Lattice spacing (Å)	Applications
InSb	0.17	d	Zinc blend	6.48	
InAs	0.36	d	Zinc blend	6.06	
InP	1.28	d	Zinc blend	5.87	transistors
GaSb	0.69	d		6.10	Thermal imaging devices
GaAs	1.43	d	Zinc blend	5.65	Integrated circuits, displays
GaP	2.25	i	Zinc blend	5.45	LEDs
ZnTe	2.28	d	Zinc blend	6.10	
ZnSe	2.58	d	Zinc blend	5.67	LEDs
ZnS	3.80	d	Wurtzite	3.81	Phosphors
CdTe	1.50	d	Zinc blend	6.48	Photovoltaic cells
CdSe	1.74	d	Wurtzite	4.30	Photovoltaic cells
CdS	2.53	d	Wurtzite	4.14	Photovoltaic cells
PbTe	0.29	d	NaCl	6.46	Infrared sensors
PdSe	0.26	d	NaCl	6.12	Infrared sensors
PdS	0.37	d	NaCl	5.94	Infrared sensors
Ge	0.67	i	Diamond	5.66	Power electronics
Si	1.1	i	Diamond	5.43	Integrated circuits

* d. direct bandgap; i. indirect bandgap

Regardless of the type of bandgap the application of semiconductors requires high quality crystals and a strong consideration of surface and interface chemistry. Any crystal defects or impurities can lead to significant changes in charge transport behavior.[2, 3, 8, 10] However, by carefully controlling the impurities, we can adjust the charge transport properties and optimize for the desired application. High quality single crystal silicon is produced using the Czochralski method,[1] which can then be cut into thin wafers and selectively doped as needed. These methods are incredibly well developed due to our massive reliance on silicon for so many semiconducting applications. However, silicon is an indirect bandgap semiconductor, meaning its efficiency in any absorption or emission based applications is less than ideal. For these other applications, there is a full complement of known direct bandgap semiconductors available, a few of which are listed in Table 1.1. The integration of these other semiconductors into current technology is somewhat problematic due to difference in lattice structures and spacing. Additionally, many of them contain either rare or highly toxic elements making them difficult to commercialize.[11-13] This means there is still a drive for a highly efficient, non-toxic, direct gap semiconductor that will be capable of seamless integration into current technology, i.e., silicon compatible.

1.2   Group IV Semiconductor Alloys

To ensure monolithic integration, one strategy is to use a material with similar crystal structures and chemistry. Both silicon and germanium are highly compatible with each other but as previously mentioned, have indirect bandgaps.[14] It is possible however, by expanding the crystal structures, to induce a transition from indirect

bandgap to direct bandgap.[15-18] As the spacing between atoms increases the changes

in orbital overlaps and density of states results in alterations in the bandgap.[9] This effect

can be achieved through epitaxy but this requires extra costs and the use of undesirable

substrates. Another approach to expanding the lattice is by exploiting Vegard's law[19]

and directly alloying larger atoms into the crystal. While there are plenty of options

available on the periodic table, one atom stands out from the rest for this purpose. Tin is

in the same group, has similar chemistry to both elements, has a known matching cubic

structure, is fairly cheap and abundant, and is environmentally friendly.

1.2.1 $Ge_{1-x}Sn_x$ and $Si_{1-x}Sn_x$ alloys

The incorporation of elemental tin into an alloy with germanium or silicon is a

topic that has been studied for around 30 years.[20, 21] With the biggest strides only being

made in the past decade. Strong experimental proof has been able to back up

theoretical calculations.[22-25] Early work focused on establishing the theoretical

background for the alloying effects and developing a synthesis that is able to produce

high quality films.[14, 15, 26-29] Theoretical studies have shown that a direct gap can be

induced in both silicon and germanium with the incorporation of ~11-25% tin,

unfortunately the large discrepancy in atomic size makes the practical production of the

alloys at that high composition difficult. In fact, there has yet to a synthetic method

reported that can successfully produce a homogenous $Si_{1-x}Sn_x$ alloy, instead tin tends to

segregate into dots within the silicon matrix. In contrast, attempts at producing $Ge_{1-x}Sn_x$

homogenous alloys have been fairly successful with control over composition and

systematic changes in optical properties achieved.[15, 23, 25, 26, 28-32] Atwater et al, were

9

able to implement a low temperature atomic deposition method to grow $Ge_{1-x}Sn_x$ alloys, with as much at 34% Sn, epitaxially on a germanium substrate.[14, 33] These techniques have been refined over the years, with different variations of precursors and deposition methods. The one constant, due to the low temperature synthesis, is the need for an epitaxial substrate to not only grow the material but also to cap it so that it can be annealed to produce a high quality crystal.[23] The need for a sandwich type structure not only increases cost of production but more importantly has a detrimental effect on the desired changes to the band structure.[34] While the electronic effects of Sn incorporation are still a factor, as previously mentioned the expansion of the lattice relative to that of pure germanium is still highly important.[18, 35] The use of epitaxy for growth resulted in compressively strained films that deviated from Vegard's law, this led to continual discrepancies between the experimentally determined point of cross over from indirect to direct bandgap and the experimental findings. As such, for many years the amount of tin required to induce the transition was always controversial with reports ranging from 5% all the way up to 21%.[23-25, 28, 30, 31, 36, 37]

1.2.2 Elucidating the direct gap transition in $Ge_{1-x}Sn_x$

One method to determine whether or not a material has transitioned from an indirect to a direct bandgap is through photoluminescence measurements. Since the process of excitation and relaxation in a direct gap is far more efficient, a dramatic increase in quantum yield should be observed after the cross over point. Experimental studies have shown this effect in tensile strained Ge films[38, 39] and is high quality $Ge_{1-x}Sn_x$ alloy films.[23] Numerous studies have explored the transition with respect to,

doping, strain, excitation density, temperature and composition. In pure germanium there is still a direct bandgap, it is just difficult to observe experimentally.[38] The direct bandgap can be measured by ensuring all energy levels below it, from the indirect band, are filled, this can be achieved by doping or high excitation densities.[18] The addition of tin however, lowers the direct gap to a lower energy than that of the indirect gap making it the most favored transition. While multiple studies have shown an increase in photoluminescence when reaching the 'critical point' where the amount of tin is enough to induce the transition most of these were done on compressively strained films. Some of the standout reports were able etch away the epitaxial buffer layers resulting in relaxed $Ge_{1-x}Sn_x$ alloys. These studies were able to show a direct correlation between strained samples retaining an indirect gap and the formation of a direct bandgap upon relaxation, these effects can be seen in Figure 1.3.[23, 25, 37, 40]

While the expansion of the crystal lattice is a driving effect in the transition from indirect to direct bandgap it is not the only one. When the lattice expansion is achieved by tin incorporation we must also consider the merging of electronic properties, especially since tin has a bandgap that is sufficiently small that it almost always acts like a metal.[41, 42] Since, in a homogenous $Ge_{1-x}Sn_x$ alloy the crystal structure is pure diamond like cubic, we can expect tin to behave as its semimetal form α-Sn which has a band gap of 0.009 eV.[42] From this point any mention of tin should be considered as α-Sn or considered as atoms being substitutionally doped into a Ge lattice. Any mention of tin's metallic allotrope β-Sn will be clearly noted and for the most part has little bearing on the topic at hand, aside from ensuring it is not produced.
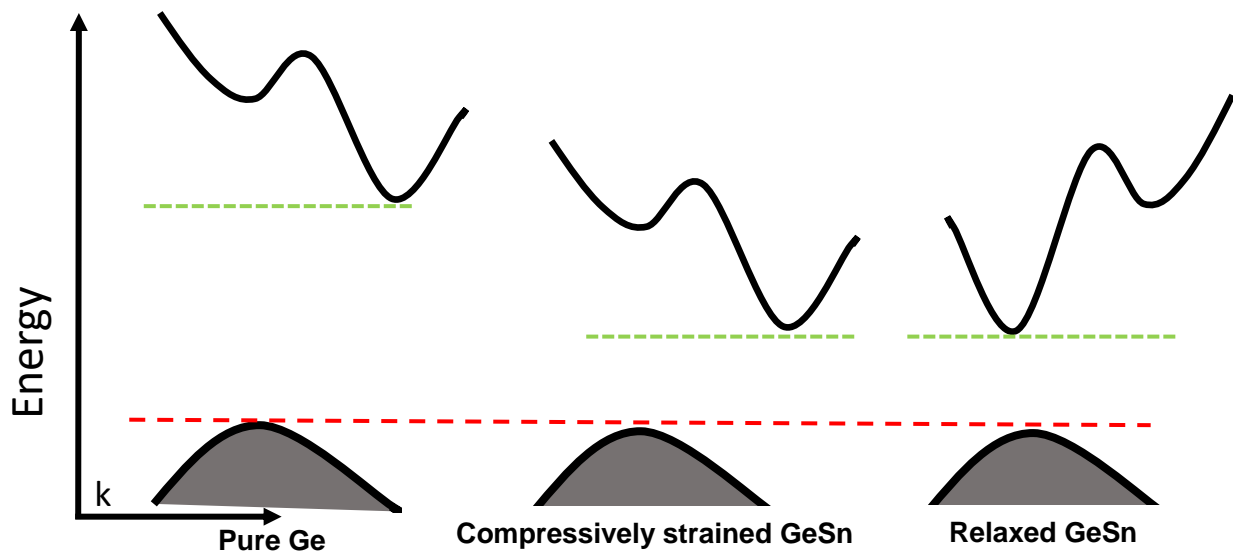
Figure 1.3.   A schematic of the different band structures for Ge, compressively strain Ge$_{1-x}$Sn$_x$ and fully relaxed.

It is important to note that the bandgap energy with respect to alloy composition has a nearly linear relationship, which has been calculated and reported extensively for thin films.[15, 23, 24, 28, 43, 44] Consequently, the bandgaps of Ge$_{1-x}$Sn$_x$ films decrease rapidly from 0.67 eV of pure single crystalline germanium down to values of ~0.30 eV for Ge$_{1-x}$Sn$_x$ alloys with more than 20% Sn[14, 28]. While a material with a tunable bandgap is desirable, the effective range of this of Ge$_{1-x}$Sn$_x$ very limited uses, mostly infrared detection for which highly effective commercial devices are already available. In order to produce Ge$_{1-x}$Sn$_x$ alloys that have higher bandgaps more suitable for absorption and emission applications, quantum confinement effect can be exploited.

1.3   Quantum Confinement

The concept of quantum confinement is very often looked at from the top down approach. It is defined by the reduction in a materials size smaller than that of the Bohr radius of the material, where the Bohr radius is the distance an excited election can travel from its corresponding hole as discussed in section 1.1. When this condition is met, the particle in a box model becomes relevant for excitons when considering the size vs energy relationship. In section 1.1, I describe the transformation of HOMO-LUMO energy to bandgap as the periodicity of a material increases. The range where quantum confinement come into play is a midpoint where there is still some periodicity but, there are still well separated 'quantum' energy levels (Figure 1.4).[10, 45]
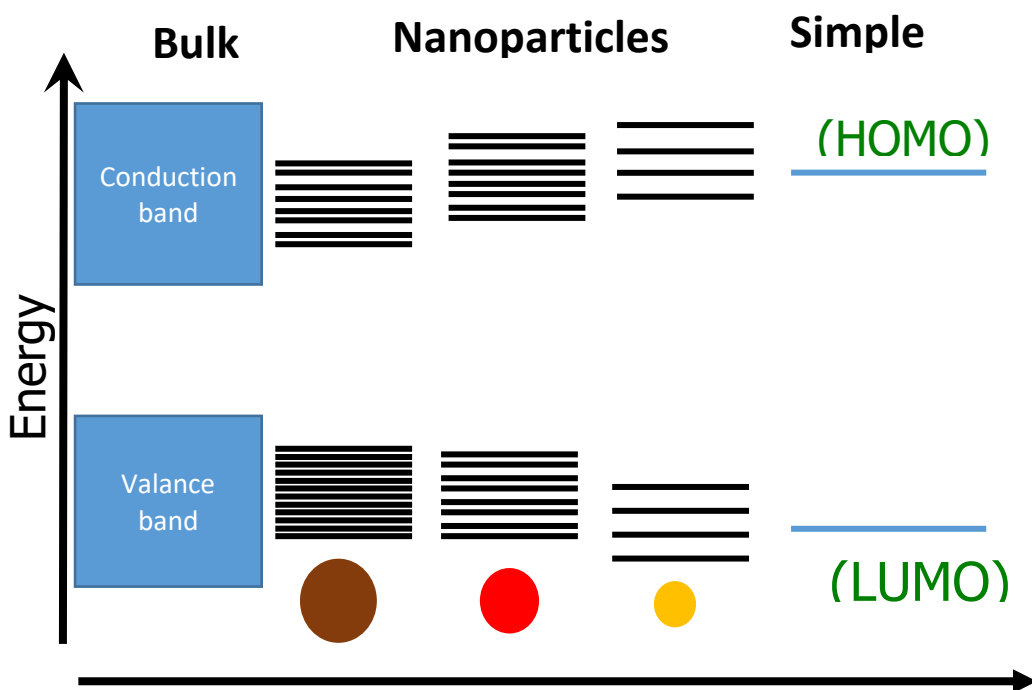
Figure 1.4.   Evolution of energy levels from discreet atomic bonding too continuous energy bands of bulk materials.

As seen in figure 1.4 the energy separation between the valence band and conduction band increases as particle size decreases. This is in part due less overlapping orbitals and also because the holes and electrons are physically confined in a much smaller area. These changes in energy (ΔE) in the confinement range can be modeled with equation 1.2.[8]

$$\Delta E = \frac{h^2 \pi^2}{2R^2} \left[\frac{1}{m_e^*} + \frac{1}{m_h^*} \right] - \frac{1.8e^2}{\epsilon R} \tag{1.2}$$

This equation uses a few assumptions on charge carrier masses and dielectric constant values and as such does not make for a valid model to compare calculated values and experimental. It does however provide a decent estimate of the changes to bandgap energy with respect to particle size and confinement effects. The ability to tune the gap energy of a material as a function of size and shape is one of the major driving forcing behind the development of semiconducting nanoparticles.[45] The size at which confinement effects are observed is highly dependent on material properties and can range from 2.2 to 50 nm.[8] Thus, development of diverse synthesis methods is important to advancing semiconductor research.

1.4   Synthesis of Nanomaterials

The production of materials on the nanoscale is a challenging task, the high surface to volume ratio inherent at the nanoscale leads to extremely reactive and unstable surfaces.[8, 10, 45] The two major categories of synthesis techniques are top-down and bottom-up.[7] Top-down methods start with a bulk material and destructively break them apart either through a physical or chemical method. Bottom-up methods

utilize coalescence of atoms to build up particles from scratch. Each has its own advantages and disadvantages, top-down tend to be easily scalable but produce non-uniform particles, bottom-up methods are more versatile can produce higher quality particles but are typically require complicated chemistry and are difficult to scale up.

1.4.1 Top-down Approaches

One of the simplest ways to produce nanoparticles is by physically bashing a piece of material into smaller and smaller bits.[46] Ball milling is one of the most effective ways to achieve a repetitive physical crushing. A ball mill is simply a cylinder with some ball bearing inside it (typically all stainless steel unless another material is required), a powdered material is then loaded into it and the cylinder is rotated. As the ball bearing crash around there constantly collide with the material, with other ball bearing, and with the cylinder walls. All of these collisions break down the material into progressively smaller pieces. The issues with ball milling are many; particle size control is possible but is fairly limited based on the material, particle shape and dispersity is nearly impossible to control, and high energy collision can generate heat altering the material being worked.[47] For these reasons it is less than ideal to produce nanoparticles for semiconducting applications.

Etching methods are far more suitable for producing nanoscale semiconductors. Chemical etching and ion beam techniques both provide a high level of precision and control. In fact, ion beam and lithography are highly prevalent in the fabrication of nanostructured semiconducting devices.[7] Focused beam techniques are great for controlled etching of a surface; the beams typically consist of highly energized atoms

that blast away the surface of the material, this is expensive and a prohibitively slow process. Combining election beam with lithography allows for patterning of much larger areas at once. Lithography is limited by two major factors, one is resolution and the other is only two-dimensional control.

1.4.2 Bottom-up Techniques

Bottom-up synthesis methods are many and diverse, there are various vapor phase reactions, solution based, solid state, and solid liquid vapor interface. These methods have been developed to produce a multitude of high quality semiconducting nanostructures such as rods, wires, and particles off all shapes and sizes.[8] The techniques all vary drastically but, share a common growth mechanism. While the finer points of the mechanism all vary on a basic level they all follow the same recipe of a supersaturation of precursor coalescing to form the end product. [48, 49]

1.4.2.1   Laser Techniques

There are a few variations of laser ablation methods, the most common involving blasting a surface with a high-power laser resulting in a mini explosion. Despite starting with a bulk form the desired material this method is still considered bottom up. The bulk target material is simply a source of precursor atoms; the laser strike creates a mini high energy explosion.[48] The explosion creates a cloud of super-heated atoms, as the atoms travel away from the source they rapidly cool and begin to nucleate into nanoparticles. The atmosphere in which this takes place can be used to control the chemistry and the size of the final product. The rate of flow of carrier gas can change how long it takes for the atoms to cool, providing control of the particle size. The type of carrier gas can be

16

selected for desired chemical changes, such as using an iron target with a high oxygen content atmosphere to produce iron oxides.[50]

Alternately, laser pyrolysis can also be utilized with vapor phase precursors allowing for even greater control over chemistry. In this case highly volatile chemicals are sealed in a transparent vessel, the laser is shot through and the laser decomposes the precursor.[51] Similar to the solid state method a cloud of vaporized atoms form and begin to coalesce.

Lasing methods are an effective method to produce high volumes of nanoparticles but is not without faults. The lasing process produces incredibly high temperatures, while the high temps can ensure highly crystalline product it also limits available chemistries and growth control. In addition, surface passivation is difficult to control and typically require a post synthetic step.

1.4.2.2 Vapor Deposition

Akin to laser pyrolysis, vapor deposition methods utilize volatile chemical precursors in a finely controlled environment. Chemical vapor deposition, molecular beam epitaxy and atomic layer deposition are incredibly sophisticated techniques that require highly specialized and expensive equipment.[7, 48] The control gained by these methods often make them worth the expense. These techniques are primarily used for the production of thin films but through proper selection of substrate can be used to selectively grow quantum dots or nanowires. The growth of nanowires through vapor deposition is typically accomplished through the use of a hetero-catalyst particle a solid-liquid-vapor reaction.[52] In this reaction the vaporized precursor begins to deposit and

17

react with the seed particle and form an amalgam melt, as the concentration of the precursor in the melt increases it eventually reaches supersaturation. The precipitation then begins between the substrate and seed particle, as growth propagates the seed particle is lifted as the wire get longer (Figure 1.5). The width of the wire can be controlled by the seed particle size and the length of the wires by growth time. This technique can even be applied to producing various types of wires such as hetero-structures of alternating and even repeating material types, core shell wires and tree like branched structures.[52]
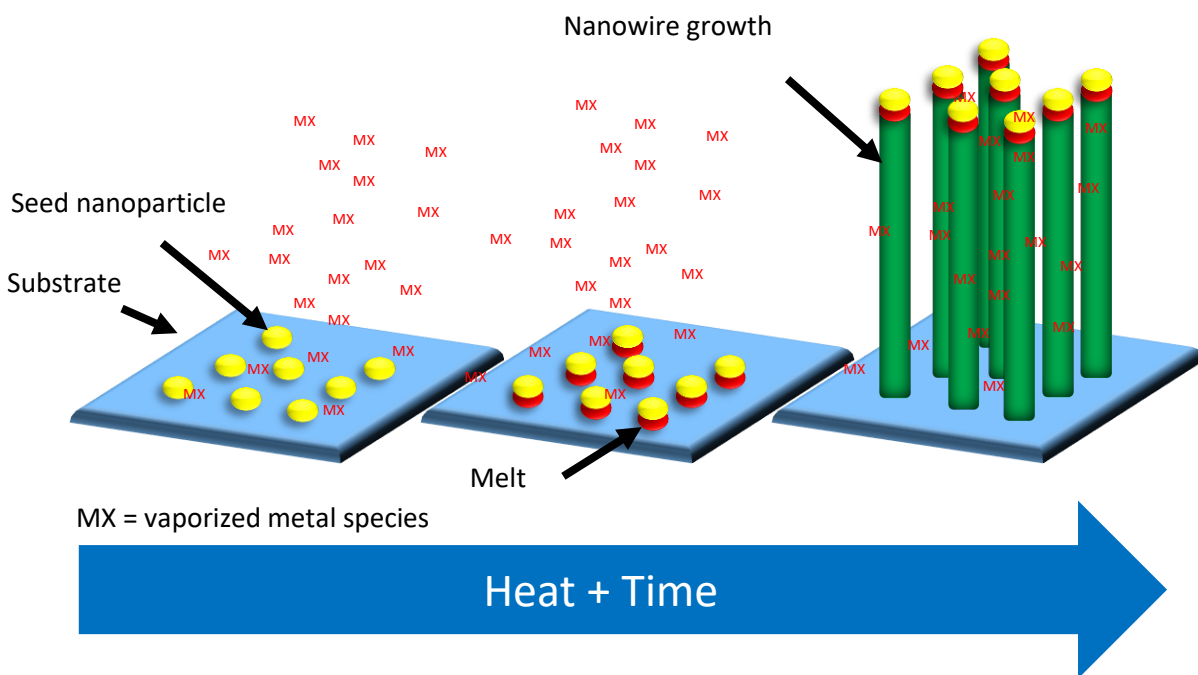
Figure 1.5. Diagram of nanowire growth through the use of vapor deposition techniques following the solid-liquid-vapor mechanism.

1.4.2.2   Wet Chemical and Colloidal Synthesis

Producing nanomaterials in a solution phase synthesis provides maximum control of variables and almost endless possible chemistries. The solvent can be

18

selected for solubility of the desired precursor, surfactants can be added to aid in growth control/surface passivation, temperature and pressure can help control crystallinity, and reducing agents can be used to decompose precursors and control the nucleation.

Solution based syntheses can be broken down into two main categories, aqueous and non-aqueous. Water works as an incredibly versatile solvent for nanoparticle synthesis due to its ability to dissolve an all kinds of metal salts, oxidizing agents, reducing agents, and surfactants, and to top it all off water is the most abundant and the environmentally friendly solvent available. In fact, noble metal nanoparticles are some of the most highly studied and understood for these reasons and an extensive number of synthesis have been developed for metal nanoparticles in aqueous systems with control over size, shape and composition.[53-55] The limits to reactions in an aqueous medium are reactivity and temperature which limit its use in synthesis of semiconducting nanoparticles. The reactivity problem is two-fold; first, while there is no shortage of water soluble precursors, not all will be sufficiently reactive enough to initiate a reaction, second, if the target compound is sensitive to oxidation, water is a poor choice of solvent. The issue of temperature is a matter of ensuring a crystalline product. Many semiconducting compounds have crystallization temperature higher than the boiling point of water and with high pressure hydrothermal bombs do not even reach the appropriate temperatures. Switching to a non-aqueous solvent allows for a wider breadth of reactive precursors and makes much higher temperatures available.

High boiling point solvents are available with all sorts different chemical functionalities. Long chain alkanes, alkenes, alkyl-amines, alkyl-thiols, and alkyl-phosphines not only allow for high reaction temperatures but also act as great growth

controlling surfactants and passivating ligands.[8, 49] Reaction temperatures from 150-350 °C combined with swift injection of chemical reactants produce a high degree of super saturation to exploit the classical La Mer nucleation model (Figure 1.6).[49] Since super
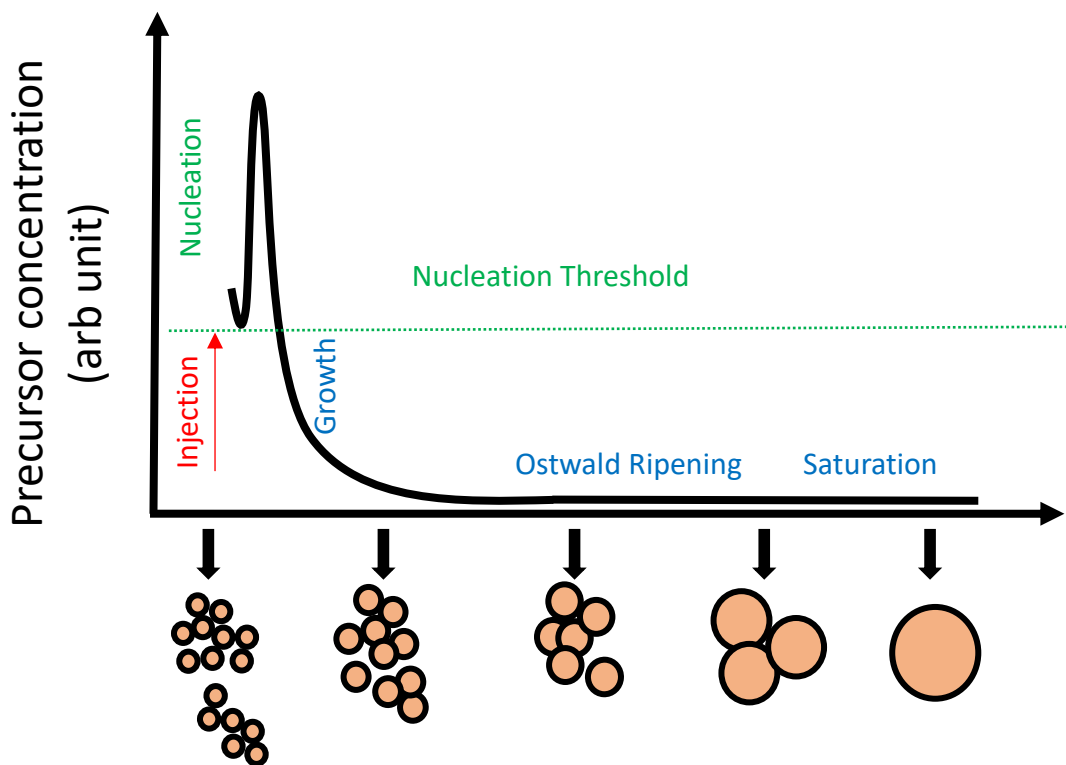
Figure 1.6. Schematic of La Mer style nucleation and growth mechanism during colloidal synthesis of nanoparticles.[49]

saturation of a solution is an unstable high energy state, the atomic precursors begin to coalesce, in order to reduce the concentration of the solution. As the reaction progresses, the coalescing begins too slow until all the precursor diminishes. Once all the precursor is consumed growth does not necessarily stop, in this next stage of growth, called Ostwald ripening,[49] smaller crystal with high energy surface sacrifice themselves. The sacrificial crystals effectively dissolve and then redeposit the atoms

onto a nearby, typically larger crystal. This process is driven by the lowering surface energies of the nanocrystals. Ripening can have a number of different effects on particle morphology. Typically, as a system ripens size dispersity can decrease leading monodispersity in the size distribution, depending on the crystal lattice ripening can also produce directional growth. Exploiting this directional growth can lead to production of rods, cubes, tetrapods, and a slew of other shapes.[8] Alternatively, in lieu of Ostwald ripening, small crystals can undergo sintering to form larger particles. Depending on of attachment occurs the resultant particles can vary drastically. If a simple coalescence occurs all of the crystallites can connect randomly resulting in a polycrystalline particle with a large degree of defects within it. On the other hand, if the lattices of each individual crystal match up before fusing it is possible for the resultant particle to grow into a single crystal.[49] Oriented attachment can also produce nano-rods and other morphologies.

1.5 $Ge_{1-x}Sn_x$ Nanomaterials

As previously mentioned studies on $Ge_{1-x}Sn_x$ have slowly been gaining traction. One reason for the slow progress is the lack of any stable bulk phase of $Ge_{1-x}Sn_x$, a quick look at any phase diagram for the alloy will shows a complete lack of elemental solubility. Thin film production overcomes this through non-equilibrium growth techniques and epitaxy.

The first $Ge_{1-x}Sn_x$ nanostructures were produce through a top-down synthesis. First high-quality thin films were produced ~ 30 nm thick. Then a reactive ion etching was employed targeted at etching pure Ge. The etching is able to remove the

germanium capping layers while still slowly etching the $Ge_{1-x}Sn_x$ layer. The differential

etching rates results in disk like structures $Ge_{1-x}Sn_x$ supported on thin germanium

pillars. Longer etching times can completely destroy the pillar support producing a

completely released a $Ge_{1-x}Sn_x$ disk.[23] Unfortunately, these disks are only confined to

the nanoscale in one dimension and do not display any quantum confinement, and the

separated disks are just dropped randomly onto the remaining substrate for minimum

usability. This process can been seen in figure 1.7.[23]
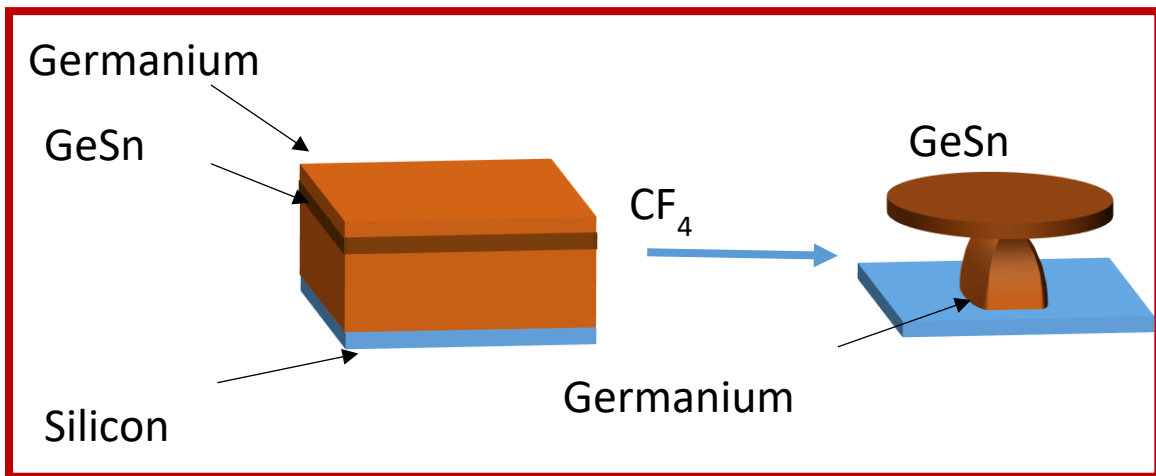
Figure 1.7. Illustration of top-down dry etching method to produce relaxed $Ge_{1-x}Sn_x$

structures.[23]

1.5.1   Epitaxy Free Synthesis of $Ge_{1-x}Sn_x$

To date, there have only been only nine reports published on $Ge_{1-x}Sn_x$

nanostructures (excluding studies on pure Ge or Sn) produced through a bottom up

synthesis.[51, 56-63] Three of them are the focus of this dissertation and are thoroughly

discussed in Chapters 3-5.[57, 59, 62] The others are each fairly unique in their approach to

synthesis and exploration of material properties.

The first synthesis of $Ge_{1-x}Sn_x$ nanoparticles was reported as just one small part of a larger study exploring the doping of Ge nanoparticles.[61] The authors initially developed a method to produce pure germanium nanocrystals with size control and well passivated surfaces. This was one of the first studies that reported confinement induced size dependent photo-physical properties of Ge nanoparticles.[64] In a follow up study the authors exchanged some of the GeI_2 precursor with an alternate metal halide. The authors reported doping with 7 different elements and had varying levels of success at incorporation. For the incorporation of Sn only 1% was achieved, any attempts at adding more Sn resulted in a phase separated product. They were however able to demonstrate that the photoluminescence of a quantum confined Ge can be shifted with the addition of Sn into the crystal. [61]

The next report took a completely different synthetic approach. The authors utilized vapor precursors with laser induced pyrolysis and explored the nanoparticles for Li intercalation for battery application.[51] Composition was easily controlled by adjusting the partial pressures of the Ge (tetramethyl germanium) and Sn (tetramethyl tin) precursors in the reaction chamber. No mention was made of attempting to control the outcome of the reaction through variations in the laser power or pulse time. The as-produced particles were well characterized through X-ray diffraction (XRD), X-ray photoelectron spectroscopy, transmission electron microscopy and energy dispersive spectroscopy. Alloy nanoparticles were produced with up to 40% Sn incorporated, based on XRD measurements. However, only particles with up to 5% Sn were produced in the absence of β-Sn.[51] This is likely due to the lack of control over the nucleation process during the lasing process. While not relevant for the application explored this

23

synthesis also has the down side of providing no surface passivation meaning it is not well suited for the production size controlled semiconducting particles for optical properties.

Microwave synthesis was utilized to produce $Ge_{1-x}Sn_x$ nanowires through the thermal decomposition of hexamethyldisilylamides of Ge and Sn. Two reports demonstrated a seed catalyzed growth of nanowires in a single pot reaction. The Ge and Sn precursors were loaded into a microwave tube with oleylamine as the solvent, a preheat step created Sn at 170 °C seed particles followed by wire growth during microwave heating up to 270 °C.[58, 60] Neither composition nor size control was gained through this method and the study did not probe any semiconducting properties.

More recently, a study on $Ge_{1-x}Sn_x$ nanowires produced via chemical vapor deposition was reported.[56] Here, instead of an in-situ generated Sn seed, the wire growth was catalyzed by AuAg alloy nanoparticles. The AuAg ally seeds allowed for greater incorporation of Sn without any surface segregation or precipitation of β-Sn in the system. Photoluminescence studies point to a cross over from indirect to direct bandgap behavior[56] but the wires are too large to produce quantum confinement effects.

Production of size and composition controlled homogenous $Ge_{1-x}Sn_x$ alloy nanoparticles was finally achieved through carefully controlled reactions in alky-amine solvents. This approach developed by researchers at Los Alamos National Laboratory combined the GeI_2-amine disproportionation with thermal deposition of hexamethyldisilylamido-Sn for unmatched control over particle size ranging from 7 nm to 12 nm with compositions up to 42% Sn.[63] This synthesis was able to overcome

material instability through temperature and concentration control of the nucleation stage and strong surface passivation in following the growth stages. These concepts are discussed further in Chapter 3. Given the narrow size dispersity achieved in this study and control over alloy composition, the optical properties were probed. Size dependent confinement induced blue shifting was observed confirmed at a given Sn concentration and concentration dependent red shifting at a given size. Both absorption and photoluminescence measurements were employed in this study with energy gaps reported in the near to far infrared region of the electromagnetic spectrum.[63]

1.6   Thesis Statement

There are three primary goals to be explored within this dissertation in order to increase the energy range of $Ge_{1-x}Sn_x$ alloys into a more technologically viable region. First is the development of a wet colloidal synthesis to produce $Ge_{1-x}Sn_x$ nanocrystals and perform initial physical and optical characterization to understand structure properties relationships (Goal 1). Second is to improve synthetic control to produce ultra-small particles in order to further probe the limits of quantum confinement in $Ge_{1-x}Sn_x$ nanocrystals and elucidate their luminescent properties (Goal 2). The third goal is to use ultra-fast spectroscopy to preform in-depth analysis of the exciton fine structure and carrier dynamics in $Ge_{1-x}Sn_x$ nanocrystals providing key information to guide the development of device structures. (Goal 3).

At the onset of this work in 2012, there was zero reports on nanoscale synthesis of $Ge_{1-x}Sn_x$ alloys and at the time of its inception all approaches to synthesis were novel. The choice of pursuing a colloidal route for the synthesis of $Ge_{1-x}Sn_x$

nanocrystals is twofold. First is to exploit control over nucleation and growth kinetic in order to overcome difficulties in forming a homogenous alloy. Second is to precisely control the size and shape common in colloidal methods to produce crystals with low size dispersity and small enough to elucidate size dependent absorption and emission properties.

The development of high-quality pure Ge nanocrystals produced by Lee et. al.[65] and Ruddy et. al.[64] provided important ground work for synthesis and understanding the properties of $Ge_{1-x}Sn_x$ nanoparticles. For Goal 1, these syntheses provide a decent starting point however addition of Sn complicates all stages of the synthesis. As such, manipulating the nucleation and growth kinetics are integral in producing alloy nanocrystals without any single element impurities. With the lack of any $Ge_{1-x}Sn_x$ nanocrystalline research to start from, the initial goal was simply producing nanocrystals of any size or shape and fulling characterizing them. Starting by synthesizing nanocrystals larger than 10 nm provides a base for much easier physical characterization. Below that size, broadening of diffraction features can obscure structural determination and even hide impurities. Acquiring elemental maps through electron microscopy, while possible, is much more difficult for smaller particles and requires more advance instruments. Utilizing a larger set of nanocrystals enables more rapid development of the synthesis to and understanding factors that lead to control over nucleation, crystal size, dispersity, and composition. With a better understanding of synthetic controls a set of quantum confined $Ge_{1-x}Sn_x$ nanocrystals can then be produced to probe the opto-electronic properties of the material across different

composition of Sn. Without confinement, the energy gap decreases very rapidly as a function of Sn into a range where characterization is limited (Goal 1).

Goal 1 successfully achieved the development of quantum confined $Ge_{1-x}Sn_x$ nanocrystals with energy gaps greatly blue shifted from thin film counter parts of similar compositions. However, to better understand the changes to the nature of the energy gap emission properties need to be observed and studied. Reducing the size of nanocrystals is a common strategy for improving luminescent properties. Further adjustments to the synthesis resulted in the production of ultra-small $Ge_{1-x}Sn_x$ nanocrystals. Physical characterization at this size range is difficult but a combination of X-ray diffraction and HRTEM provides significant proof of structure and compositions. Strong quantum confinement effects result in an incredibly high energy gap while maintaining the tunability vs Sn composition as reveled by photoluminescence measurements (Goal 2)

Simple absorption and emission studies are great for determining size and composition dependent changes on the energy gap. However, more in-depth methods are needed to understand the exciton fine structure. Time resolved photoluminescence measurements provide significant detail into the relaxation path of an excited electron. Combined with variable temperature spectroscopy it is possible to decipher what type of energy states the excitations are relaxing through. Understanding the exciton fine structure and the carrier dynamics are an integral part of being able to design a device that requires extraction of photoexcited charge carriers from the nanocrystal (Goal 3).

Gaining control of size and composition is vital to fully understanding the photophysical properties of $Ge_{1-x}Sn_x$ alloy nanocrystals. The first part of dissertation

successfully developed a synthetic method with control over size and composition. (Goal 1). The section utilized the synthetic control in-order to probe the extent of confinements effects possible and elucidate visible photoluminescence in $Ge_{1-x}Sn_x$ nanocrystals (Goal 2). Advances spectroscopy methods were able to provide a significant understanding the photo-induced charge carriers and fine structure of the energy gap in-order to help guide future device development (Goal 3).

CHAPTER 2

CHARACTERIZAION TECHNIQUES

In order to fully understand a material's properties a full range of characterization techniques must be employed. A combination of physical, optical and chemical characterizations were necessary to elucidate the structure-property relations in nanocrystalline products. When considering nanomaterials understanding the crystal structure is of great importance, especially for semiconducting purposes. Powder X-ray diffraction (XRD) is incredibly useful for this purpose and can not only confirm structure but also identify any crystalline side products or impurities. Size estimates can also be garnered from the applying the Scherrer equation to XRD data with significant line broadening. For more accurate size measurements, transmission electron microscopy (TEM) can provide physical images of individual nanoparticles. High resolution TEM (HRTEM) can be used to image lattice fringes and confirm crystal structure. While crystal structures typically indicate well defined stoichiometry, nanoparticles can deviate and certain alloys still require secondary confirmation of composition. There are two major techniques to determine the composition of nanoparticles: energy dispersive spectroscopy (EDS) and inductively coupled plasma optical emission spectrometry (ICP-OES). EDS is a semi-quantitative technique but is highly favored because it is non-destructive and can be performed in-situ in either a scanning electron microscope or a TEM. In fact, the true power of EDS is when it is coupled with HRTEM allowing for the elemental mapping of individual nanoparticles. In contrast, ICP-OES is highly accurate analytical technique but requires destruction of the analyte and only provides a sample

average. An important aspect of producing high quality nanomaterials is their surface chemistry and functionalization. Techniques such as thermogravimetric analysis (TGA), Raman, and x-ray photoelectron spectroscopy (XPS) all provide different insights into surface chemistry and functionalization of the surface. The final piece of the puzzle is to determine optical and electronic properties to match with the physical characterization. Optical absorption measurements are performed on both colloidally dispersed particles and solid powders through solution UV-Vis and diffuse reflectance spectroscopy, respectively. Photoluminescence measurements combined with absorption are used to determine energy gaps and the extent of quantum confinement. Time resolved, temperature dependent, and excitation density measurements provide important insight into the carrier dynamics of excitons in the semiconductor nanocrystals.

2.1 Powder X-ray Diffraction

Powder X-ray diffraction (XRD) is useful tool for understanding the crystal phases and structures of materials. Crystal structures are defined as a periodic arrangement of atoms with identical repeating units. A wide script of describers have been developed for crystal systems including orientation, symmetry, unit cells, atomic arrangements, and atomic distances.[66, 67] While many elements and compounds share similar crystal arrangements they still differ based on atomic composition and bonding type. These variations give each crystal is unique 'fingerprint' that can be observed as an X-ray diffraction pattern.

The two most important components to an XRD instrument are an X-ray source and a detector. The first X-ray diffraction experiment was accomplished by placing a

crystal between the source and detector, this experiment confirmed for the first time not only the periodic nature of crystals but also the wave nature of X-rays. Since then many advances have been made in X-ray crystallography, from the types of X-ray sources to measurement techniques and detection methods. An X-ray 'tube' has been the standard device for producing X-rays for quite some time now with improvements always being made. A standard X-ray tube consists of four main components, a tungsten filament, a metal target (Mo, Cu, Fe, Co, Cr), a beryllium window, and a cooling apparatus (Figure 2.1).[66, 67] The tungsten filament is used to produce an electron beam by running an extremely high accelerating voltage through it (20,000 V- 60,000 V) where the filament is the cathode and the metal target is anode separated by a vacuum. As the high-
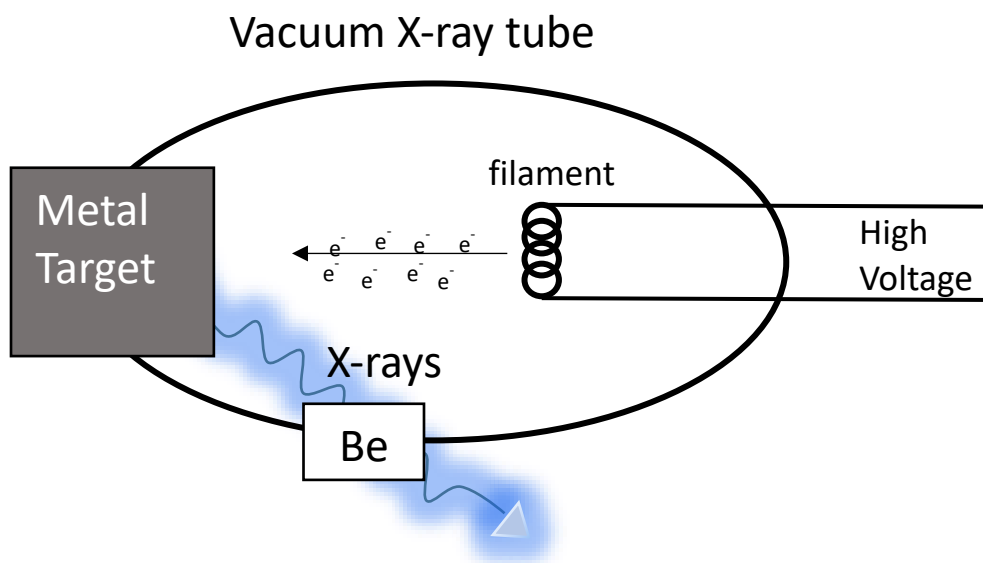
Vacuum X-ray tube

Figure 2.1. Diagram of a standard vacuum X-ray tube.[66]

energy electron beam bombards the metal target its atoms become ionized. If the electrons have enough energy they are able to kick an electron out of the metal's K

31

shell creating a highly unstable hole (Figure 2.2).[66, 67] To fill this vacancy an electron from one of the outer shells, L or M fall to the K shell and in the process, emit energy in the form of X-rays. The wavelength emitted is constant for a given element and shell to shell transfer. When an electron falls from the M shell to fill the vacancy, the emitted X-rays are labeled as K_β, these X-rays are of relatively low every most are reabsorbed before even making it out of the metal target.[66, 67] The important X-rays are K_α, produced from L to K transitions. Since K_α is a defined energy for every element, sources can be
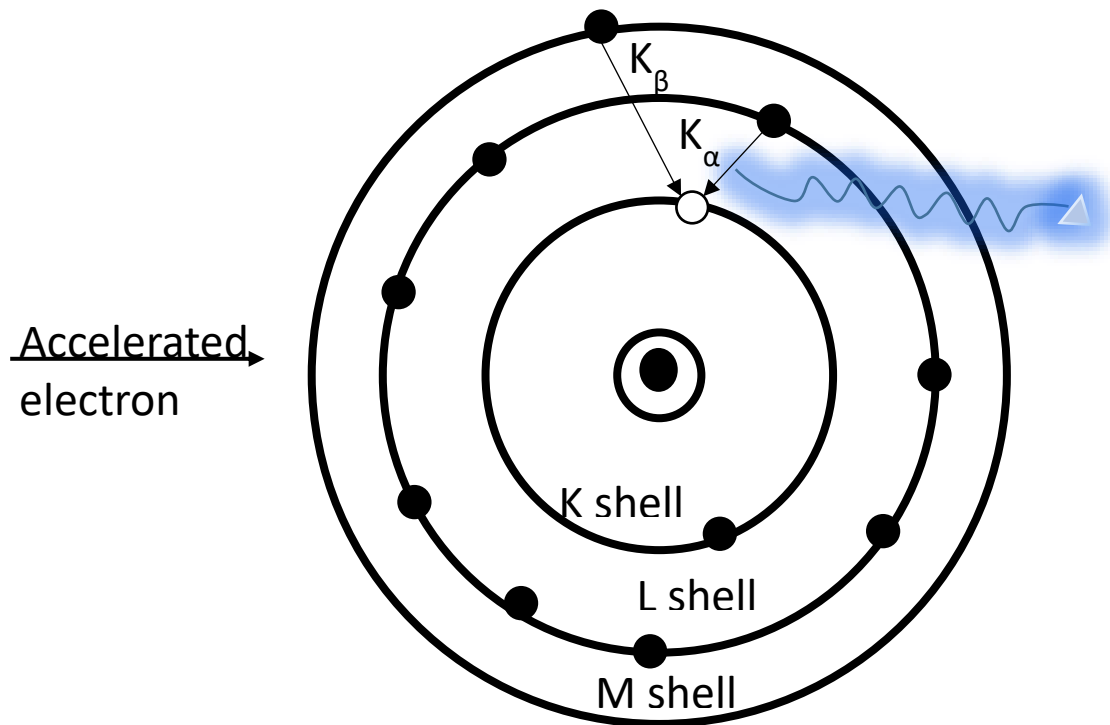
Figure 2.2. Electronic shell diagram of electronic transitions for X-ray production.[66, 67]

selected to best fit the application. The X-rays are emitted in all directions from the target and in order to control them only a small section of the tube is designed to allow them to escape. A small widow, made out a material with a low X-ray cross section,

typically beryllium, is used to create a directional source.[66, 67] The last component which is not pictured in Figure 2.1 is critical to the function of the X-ray tube however has nothing to do with X-rays itself. Modern X-ray tubes are run at such high voltages that if the metal target is not constantly cool it will heat up enough to begin to melt, destroying the tube.

With a well-defined directional X-ray source, it is possible to control the angle of incidence. Being able to control the angle of X-ray incidence is of key importance in determining the atomic spacing through diffraction. When X-rays collide with the surface of a crystal scattering occurs in every direction. Many of the X-rays will make it past the surface and penetrate the crystal for a significant depth. If we consider exactly two beams incident to the crystal (Figure 2.3),[66, 67] one striking a surface atom (A) and
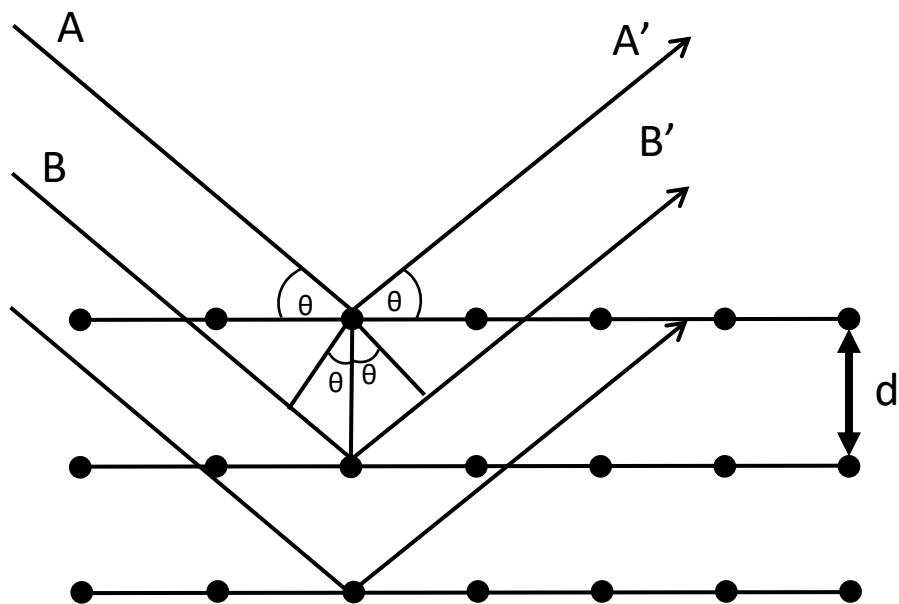
Figure 2.3. Diffraction of X-rays by parallel crystal planes.[66, 67]

the other striking an atom in the next to top plane (B), we can start to build the picture of diffraction. If both beams reflect elastically at an angle equal to incidence it is clear to see that B will travel further than A. Depending on how much father B travels it can end up in-phase or out of phase with A. When the distance traveled results in A' and B' being in phase, the amplitude of the wave increases.[66, 67] When the rays are out of phase the amplitude decreases, in some cases resulting in complete destructive interference such as when d is equal to ¼ of the wavelength of the X-rays. Only when AA' and BB' are in phase the scattering of the X-rays is considered a diffracted beam. Knowing the conditions which lead to coherent diffraction allows us to apply the Bragg Law (equation 2.1) where n is the order of reflection, λ is the wavelength of the X-ray, d is the distance between planes and θ is the angle between the incident beam and the surface to the crystal.[66, 67]

$$n\lambda = 2d\ Sin\theta \tag{2.1}$$

The narrow line widths of diffraction peaks are a result of interfering waves produced across thousands of planes canceling out diffraction from non-Bragg angles. In nanocrystals, there are not enough lattice planes to create beneficial interference, resulting in a broadening of the diffraction peaks. The Scherrer equation (2.2) takes advantage of the line broadening to determine the size of a crystal. The crystal size is t, λ is the wavelength of the X-ray, B is the FWHM of the peak and θ is the diffraction angle.

$$t = \frac{0.9\ \lambda}{B\ \cos\theta} \tag{2.2}$$

Samples in this study were analyzed using a Philips X'Pert Pro, running Cu Kα monochromatized radiation with a wavelength of λ = 1.5418 Å. All samples were in powder form and loaded onto a low background Si sample holder with a spinning stage to improve sample averaging. Instrumental line broadening was measured with a Si standard and accounted for in any calculations.

2.2   Transmission Electron Microscopy

When talking about semiconducting nanocrystals one of the most substantial topics is size dependent properties. As such, properly determining the size of nanocrystals is a fairly significant part of any study. There are multiple ways to accomplish size determination including light scattering, spectroscopy, diffraction, however most of these only provide a 'virtual' size of the sample. Transmission electron microscopy (TEM) stands out in its ability to provide an actually 'physical' representation of particle size. In addition to size, the images produced by TEM show the morphology and structure of nanoparticle, something the previously mentioned techniques cannot accomplish. High resolution TEM has the power to resolve crystal lattice arrangements and even individual atoms which can be combined with X-ray spectroscopy to provide elemental identification.

The electron source in a TEM is basically the same as in an X-ray tube (Figure 2.1). A tungsten filament is heated up with extreme high voltage (80-400 kV) under vacuum resulting in the emission of electrons. Unlike in an X-ray tube, in which the electrons are used to produce X-rays, in a TEM the electrons are focused through a series of magnetic lenses to directly probe a sample.[68] In basic imaging, the electron

beam is spread out across a sample, some of the electrons are blocked by the sample and a negative is created by the unimpeded electrons. The disadvantages to this method lay in sample thickness, and attenuation coefficients of elements. To provide the best possible contrast the sample holder needs to be incredibly thin with a low electron cross section, in most cases, a think carbon film from 3-30 nm supported by a copper mesh is sufficient for this purpose. When the electron beam, a host of interaction are possible and essentially all occur concurrently (Figure 2.4).[68] The numerous interactions are what make a TEM instrument so versatile, with proper control of the beam through focusing lenses and detection methods a slew of information can be gathered from a single sample in a single session. First is obviously TEM basic imaging as already described, in which transmitted electrons strike a detector below the sample. By changing the focus of the beam post sample interaction, it is possible to detect scattered and more importantly diffracted electrons for selected area electron diffraction (SAED) patterns providing information of crystal structure. Since the sample is being bombarded with high energy electrons, some the atoms will undergo excitations and emit X-rays in the same manor they are produced in X-ray tubes.[68] The X-rays produced are unique to each element and can be used to a determine composition
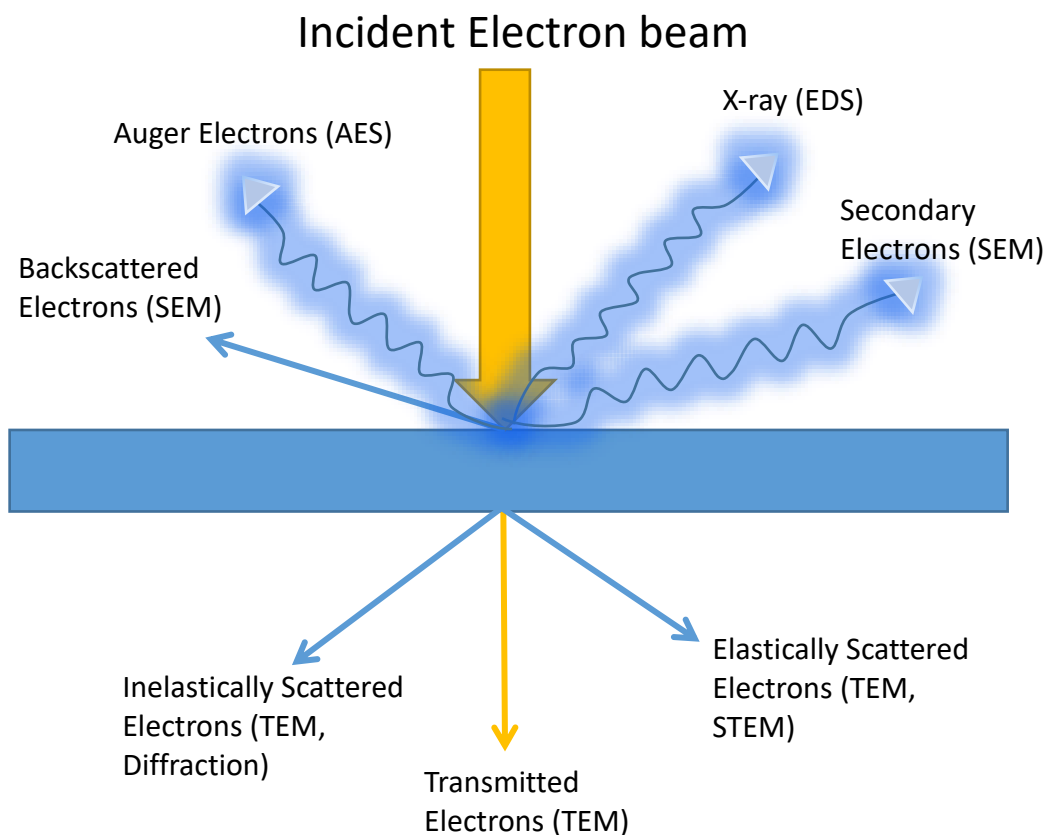
Figure 2.4. Simplified scheme of possible interactions of an electron beam with a target substrate.

through Energy Dispersive spectroscopy (EDS) with a detector positions above the sample.[68] Some electrons are backscattered or reemitted from the sample these are typically not used in a TEM but are important for scanning electron microscopy (SEM).

Multiple instruments have been used in this study to acquire basic imaging, HRTEM, diffraction, and elemental maps. A Zeiss Libra 120 was utilized to acquire low resolution images at 120 kV as well as SAED. Elemental maps were acquired with a FEI Titan 8300 microscope equipped with a Gatan 794 multiscan camera operating at 200 kV. HRTEM was conducted on a separate FEI Titan 8300 electron microscope

operating at 300 kV. All samples were prepared by dropping a dilute solution of nanocrystals dispersed in CCl_4 onto an ultra-thin carbon coated Cu TEM grid after the removal of the Formvar layer.

2.3   Energy Dispersive Spectroscopy

To determine the average composition of a sample we can employ EDS within a SEM or TEM, which can monitor a much larger area of sample at once. EDS measures X-rays emitted from excited atoms, since each element has unique atomic energy levels it is possible to qualitatively analyze elemental composition.[68] The emission of X-rays from substrates has already been described in sections 2.1 and 2.2 and Figure 2.4. The electron beams used for imaging in TEM and SEM are simultaneously also exciting the sample and subsequently inducing X-ray emission. The limitations of EDS are based on the energy of the incident electrons, range of the detectors, and spectral overlap.

In this study, dried powder samples of nanocrystals were spread onto a conductive carbon tape attached to an aluminum stub. No other sample prep was needed before loading the samples into the instrument. EDS measurements were performed in a Hitachi SU-70 running at 20 kV accelerating voltage and averaged over five separate areas.

2.4   X-ray Photoelectron Spectroscopy

Nanocrystals are notorious for large surface to volume rations with as much as 40-60% of atoms being on the particle surface. The surface chemistry play a central role in many nanoparticle properties. One of the most powerful techniques for surface

38

analysis is X-ray photoelectron spectroscopy (XPS). XPS is one of the few methods of identifying atomic composition, oxidation state of the elements, and detail on their bonding environment. Further, even though it is primarily a surface technique, the penetration depth is around 5-10 nm. Therefore, in small enough nanocrystals, both the surface and the bulk of the particle is measured.[69]

In XPS an X-ray tub (Figure 2.1) is used as a source of X-rays to bombard a surface, as the X-ray photons collide with atomic electrons they are kicked out as photoelectrons. The energy required to kick out said electrons is equivalent to the electrons binding energy allowing for differentiation between elements, individual orbitals, and chemical environment. A high level of vacuum is necessary for XPS to ensure accurate measurements. Not only will stray gaseous molecules produce interfering signal but they can contaminate the substrate surface and more importantly attenuate the X-rays reducing the overall sensitivity of a measurement.[69] The requirement of ultra-high vacuum has driven the design of XPS instruments. Sample are loaded through a preparing chamber which pumps samples down in order to make sure
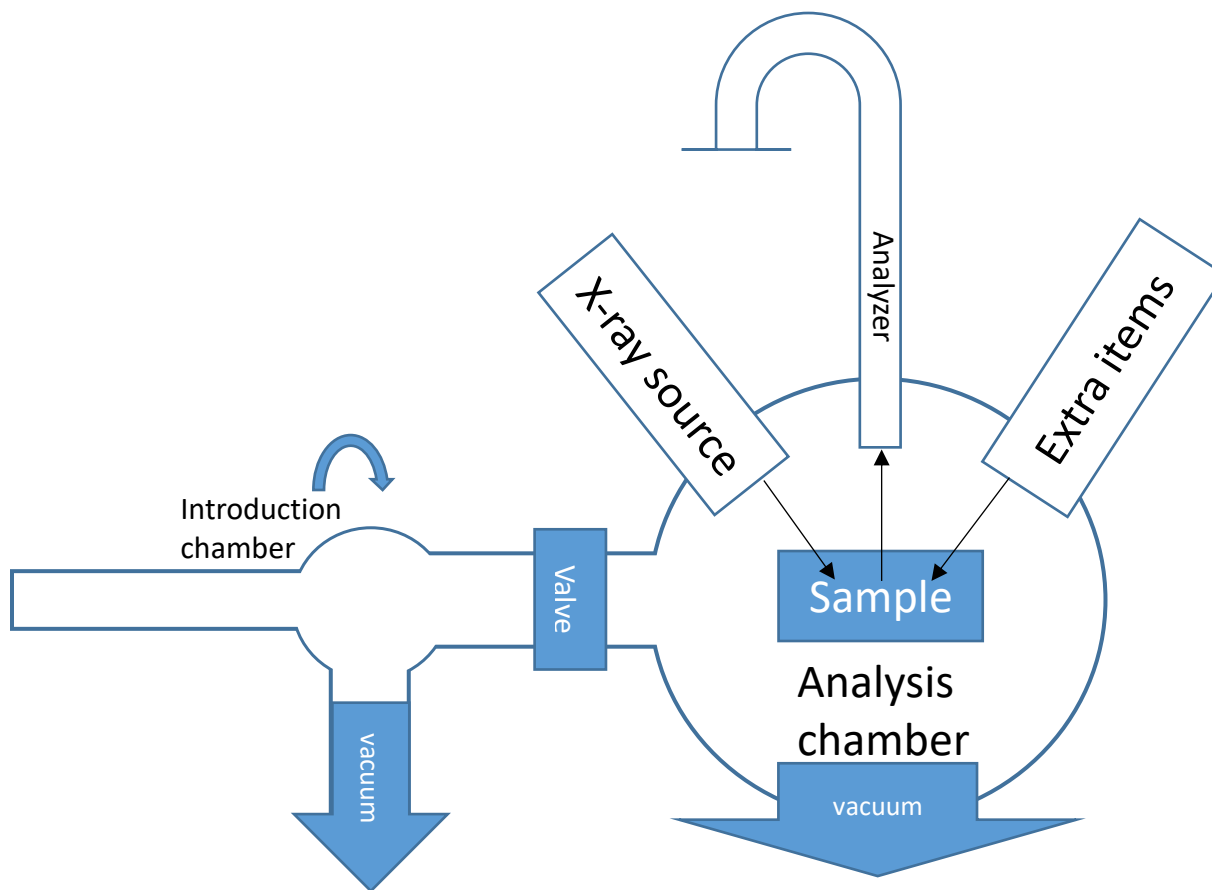
Figure 2.5. Diagram of X-ray photoelectron spectrometer with a hemispherical detector.[69]

any outgassing of the sample does not contaminate the analysis chamber (Figure 2.5).[69] The analysis chamber is kept under a constant level of ultra-high vacuum, however is equipped with certain extra items such as ion beams for etching and Ar flow for charge control. The X-ray source of choice is typically Al Kα due to its production of high energy and narrow line width. The high-energy nature of the photoelectrons being analyzed requires a method to adequately resolve closely spaced peaks and maintain sensitivity. The hemispherical analyzer is able to switch between the desired effects though variable voltage which will affect the path length of the electron for detection.[69]

The studies conducted herein were performed with a Thermofisher ESCALAB 250 equipped with Al κα source. Dried nanocrystal powders were pressed onto indium foil and taped to an aluminum sample holder with conductive carbon tape. To minimize atmospheric contamination and oxidation samples were stored and prepared in a glove box and loaded into the instrument with an air free sample loader. Charge correction was done with adventitious carbon and double checked against indium.

2.5   Raman Spectroscopy

Molecular vibrations can provide substantial information on chemical makeup of a sample. Raman is a unique type of spectroscopy in that it does not measure, absorption or emission of the probing photons. Instead, Raman measures changes in energy of scattered photons. The scattering is caused by the photons interaction with a molecules vibrational induced dipoles. Since molecular vibration are well known for many compounds, organic and inorganic, Raman can be used to monitor nanoparticle systems for surface ligands, unwanted amorphous impurities, and even changes in composition.[70]

One of the biggest limitations in Raman spectroscopy is the fundamental physics behind the measurement. Interactions of photons with phonon's have a very low probability which is exacerbated by how infrequent phonon are in comparison to incident photons. To ensure a reasonable signal is collected it is necessary to input extremely high intensity of photon, for this reason Raman instruments employ laser sources (Figure 2.6).[70] As the photons strike the sample some of them are inelastically scattered, the scattered light is then channeled through a grating and the change in

41
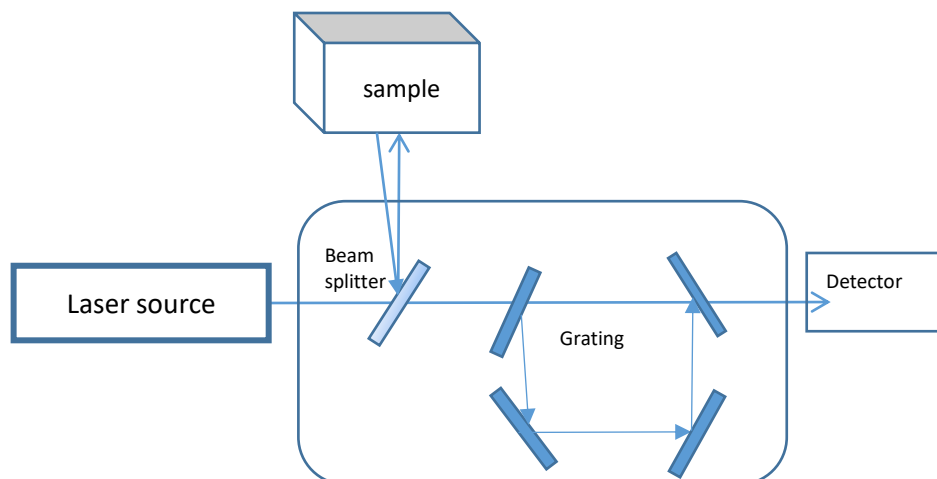
Figure 2.6. Block diagram of Raman spectrometer.

energy with respect to the incident beam, called the Raman shift, is measured. The

power behind this lays in the dependency on vibrational modes. If the molecules being

examined are visualized as two balls connected by a spring it is easy to understand

why. The Raman shift will be proportional to the frequency and amplitude of the

vibrations between the two balls.[70] If the mass of one of the balls changes or the

distance between them the frequency will decrease resulting in a smaller Raman shift.

The same effect will be seen if one of the balls confined, possibly by an extra bond from

an outside source. Powdered samples were analyzed with a 532 nm laser in a Horiba

LABram HR Evolution Confocal Raman Spectrometer. Samples were placed on an

aluminum substrate and monitored at full laser strength to probe the structural changes

in the nanocrystals.

2.6   UV-Visible absorption spectroscopy

Probing the optical transitions of compounds and materials though Uv-Vis is one of the oldest practices to study chemical physics. A compounds energy levels, HOMO-LUMO for molecules and bandgaps for materials, are studied by scanning across the Uv-Vis region and monitoring light input vs transmitted light. This is accomplished by a series of mirrors and beam splitters allowing to simultaneous measurements of a sample against a reference (Figure 2.7). The difference between the two is taken as the absorption value. Historically, the measurement is performed with the analyte dissolved in an optically transparent solvent. The absorption can then be related to the concentration of the analyte (c), the path length through the solution (*l*), and the molar absorptivity of the analyte (ε) by the Beer-Lambert Law (equation 2.3).[8]

$$A = \varepsilon l c \qquad\qquad (2.3)$$

In semiconductors, the onset of this absorption can be equated to the bandgap of the materials. The energy below the onset does not have high enough energy to induce excitation from valance band to the conduction band, beyond that point the absorption can be related to the density of states. In the case of nanocrystals, this technique can be utilized to explore the changes in gap energy as a function of crystal size and quantum confinement.
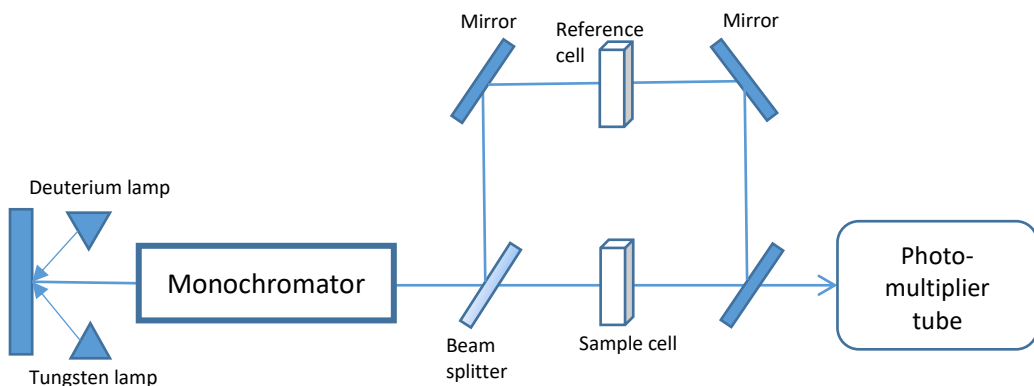
Figure 2.7. Schematic of a multi-source double beam Uv-visable spectrometer.

All solution based measurement were performed soon after the isolation of new prepared nanocrystals. The samples were dissolved in CCl_4 and transferred to a quartz cuvette. Spectra were collected in a Cary 6000i UV-Vis-NIR spectrometer (Agilent Technologies).

2.7   Diffuse Reflectance Spectroscopy

From a practical standpoint, very few semiconducting applications utilize colloidal solutions. To have a better understanding of light mater interactions of an aggregated solid we can employ diffuse reflectance spectroscopy. When light is interacting with a solid powder scattering in the form of reflectance and diffraction will occur in addition to absorption. The reflected light is recollected and can be evaluated by the Kubelka-Munk remission function (equation 2.4).[71, 72] The percent reflectance (R) is equated to a form of a pseudo-absorption coefficient (K/S) with this method, similar to that obtained through transmission experiments.[72]

$$f_{KM}(R) = \frac{(1-R)^2}{2R} = \frac{K}{S}$$

(2.4)

The Kubelka-Munk function is only one method of estimating the band gap and does not account for the type of transition occurring. Tauc formulas have been developed to account for absorption probabilities based on crystal momentum and photon-phonon interactions.[9] In applying the Tauc equation to reflectance data the k/s term from the Kubelka-Munk formula is used as the absorption coefficient (α).[59, 72] The proportionality between the absorption in semiconductors $(\alpha h v)$ and the density of states $(h v - E\_g)^{1/n}$ can be seen in equation 2.5. Where (hv) is the energy of an incident photon, (A) is proportionality coefficient, and (E$_g$) is the bandgap. The value of the exponent (n) is dependent on the interband transition being modeled, 1/3 for indirect forbidden, ½ for allowed indirect, 2 for allowed direct, and 2/3 for forbidden direct.[9, 73]

$$(\alpha h v)^n = A \, (h v - E_g) \tag{2.5}$$

The Tauc equation was never meant for application to nanocrystals since it was developed for bulk semiconductors with continuous band energies. While it has been accepted in nanocrystalline literature,[59, 65] the results of such analysis should be taken with careful consideration. In this study energy-gaps were estimated by Tauc and Kubelka-Munk through linear extrapolation of the absorption onset back to the baseline the nanocrystals were dispersed in a non-absorbing medium (BaSO$_4$) so that scattering is minimized. Measurements were performed with a Cary 6000i UV-Vis-NIR spectrometer (Agilent Technologies) equipped with an internal DRA 2500 integrating sphere.

2.8   Photoluminescence Spectroscopy

The process of photoluminescence occurs when a photon is released during the relaxation of an electron from an excited state back to its ground state. The initial excitation can be cause through photon absorption, thermal excitement, chemical reaction, or by an applied electrical current. In the case of semiconducting nanocrystals photo and electrical excitement are of the greatest interest due to their applicability for devices such as solar cells, LEDs, and detectors.[10, 74] This section will however focus on the emission process and mostly ignore the method of excitation other than its relevance to the instrumentation used for measurements. Typically, there are many electronic states involved in the excitation and emission process due to vibrational and rotational energy levels. When excitation occurs from a singlet ground state (S_0) an electron is bumped into an excited singlet state (S_1), the relaxation of the electron from S_1 back to S_0 through the release of a photon is called fluorescence (Figure 2.8). The energy of the released photon will correspond directly to the energy-gap between the two states and occurs fairly rapidly typically on the order nano-micro second time scales. However, there photoemission is not the only pathway an excited electron can relax through. If the excitation energy exceeds that of the energy-gap the excited electron must first relax from the higher energy levels through a non-radiative process.[74, 75] One form of non-radiative relaxation is through the release of heat energy in the form of molecular vibration. In addition to relaxing from elevation singlet states,
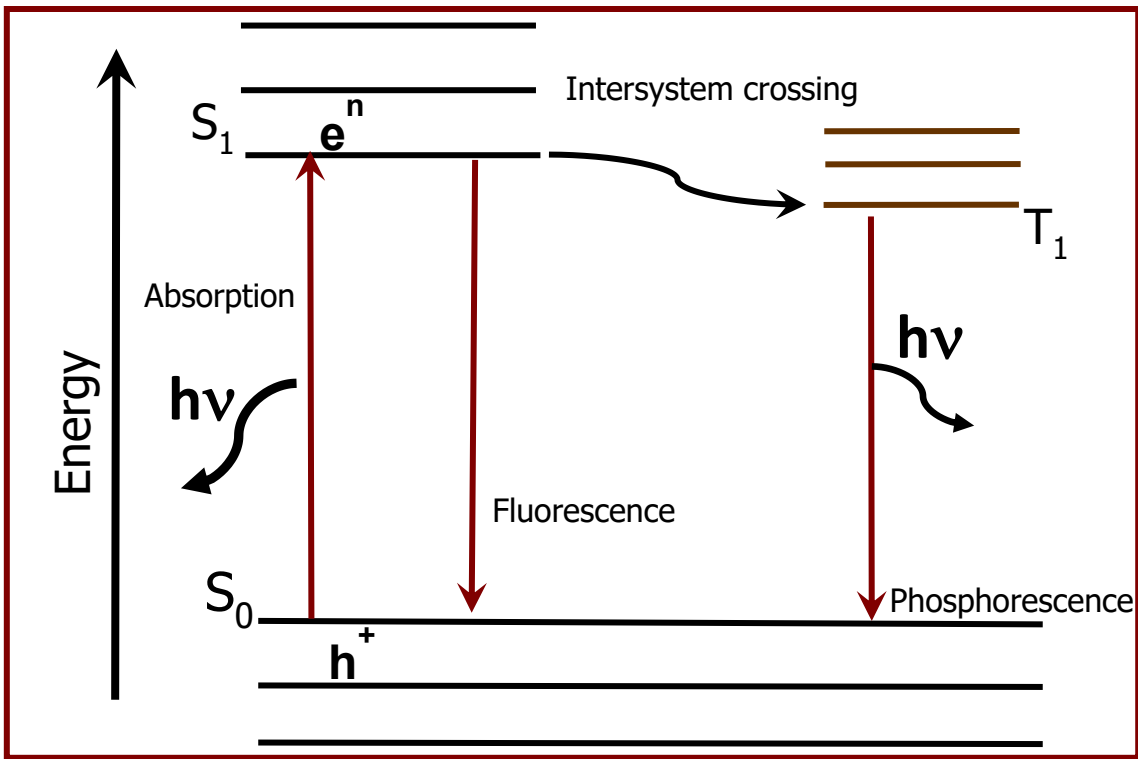
Figure 2.8. Simple diagram of photoluminescence mechanism, including absorption, fluorescence and phosphorescence.

non-radiative processes can result in intersystem crossing to an excited triplet state (T_1). Triplet states are typically caused by impurities or defects and have a lower energy than the S_1 state. The process of intersystem crossing and subsequent phosphorescence results in much longer lifetimes for the excited states, upwards of 3-5 orders of magnitude greater than that of fluorescence.

Photoluminescence (PL) measurements of quantum confined nanocrystals are used to probe size and composition dependent optical properties, carrier dynamics and fine structure of energy gaps.[57, 76] A complete understanding of energy levels and excitonic behavior is advantageous in the design of semiconducting devices. Basic

steady state measurements only provide glimpse into the photoluminescence properties. Ultra-fast spectroscopy can be employed for time resolved measurements. When combined with temperature and excitation density studies it is possible to develop a comprehensive understanding of a nanocrystals light-mater interactions. In this study, nanocrystals were deposited on a Si wafer, excited with a Ti:sapphire laser at 385 nm wavelength and PL spectra were acquired with a liquid N_2 cooled charge coupled device (CCD) camera. Temperature was controlled with liquid helium cooled cold finger and time resolved measurement were collected with a Hamamatsu streak camera with 25 ps temporal resolution.

CHAPTER 3

Nanocrystalline Group IV Alloy Semiconductors: Synthesis and Characterization of Ge$_{1-x}$Sn$_x$ Quantum Dots for Tunable Bandgaps.

3.1   INTRODUCTION

The bandgaps of semiconductor materials can be manipulated through alloying and size reduction to tune the nature and energy of optical transitions.[9, 77, 78] When considering the nature of the energy gaps, semiconductors are classified as indirect or direct while the latter is preferred due to high efficiency in absorption and emission.[79] Currently, many of the leading direct-gap semiconductors are comprised of Group II/VI,[80, 81] III/V, or IV/VI[82] elements, such as CdSe,[78, 83] InAs[80, 81] and PbSe.[82] Nanostructured solids of such materials are well studied and at the forefront of developing technologies. However, the use of toxic heavy metals has become a major concern and efforts to find substitute benign materials have become a major focus in recent years.[11-13]

Group IV semiconductors such as Si and Ge are well known indirect-gap materials with low toxicity, and through band engineering an indirect to direct gap transition can be achieved.[14-17, 23-25, 29, 36] For instance, applying tensile strain to the crystal lattice has been shown to reduce the band energy, just as the compressive strain leads to an increase in energy.[9, 84, 85] The direct gap Γ valley shrinks faster than the indirect gap L valley as the tensile strain is increased, resulting in a truly direct-gap semiconductor.[23, 24, 29] One method to engineer tensile strain is through epitaxial growth on a substrate having larger

lattice constant and another approach is *via* direct incorporation of Sn atoms to produce a homogenous Group IV alloy.[24, 25, 86] In addition to the effects of strain on the nature of the energy gaps, significant dependence of band energies as a function of Sn composition has been reported.[15, 28, 32] As such, the binary alloys of Group IV semiconductors, $Si_{1-x}Sn_x$ and $Ge_{1-x}Sn_x$, have shown promise to create an optimal direct-gap materials with low toxicity, high optical stability, and compatibility with existing Si based technologies.[14, 23, 24, 30]

Thin films of $Ge_{1-x}Sn_x$ alloys produced *via* chemical vapor deposition and molecular beam epitaxy are well studied and exhibit tunable band energies in the mid IR region.[14, 23, 24, 27, 28, 37] Unfortunately, the synthesis of homogenous alloys has proven difficult due to large discrepancies in lattice constants.[15, 37] However, many issues in the fabrication of homogenous alloys were resolved through low temperature, non-equilibrium growth processes.[14, 15, 28, 87] In $Ge_{1-x}Sn_x$ thin films, an indirect-to-direct crossover has been theoretically examined with values ranging from 10-15%[14, 15, 28] in early studies. More recently, the accepted crossover values are considered to be in between 6.3% to 11%[23-26, 30, 31] with strong experimental evidences confirming the transition occurs for Sn concentrations over 7.1%.[23-25] However, the incorporation of Sn (bandgap = 0.09 eV)[42] makes the direct energy gaps of such alloys narrower and closer to metallic behavior, limiting their potential in a number of optical applications.

The synthesis of colloidal $Ge_{1-x}Sn_x$ nanocrystals (NCs) has the potential to increase fundamental energy gaps owing to the effects of quantum confinement.[77] Taking advantage of the low temperature synthesis, high surface energies, and the passivating ligands present in many NC systems, it is possible to overcome the Sn segregation

without sacrificing the desired tensile strain. High quality, solution processable $Ge_{1-x}Sn_x$ NCs have huge potential in a wide range of applications, such as field-effect transistors,[5, 88, 89] lithium ion batteries,[51] bio-imaging,[12] lasers,[17] and optical detectors.[90, 91] Reduction of crystallite size below the Bohr radius (11.5 nm for Ge)[92] has been reported to blue shift the absorption onset as high as 1.6 eV for single element Ge NCs with a diameter of 2.3 ± 0.4 nm.[64] Such a wide range of bandgap tunability is highly advantageous for applications such as solar absorption, optical detectors and biosensors. Additionally, $Ge_{1-x}Sn_x$ alloys are compatible with current Si technologies allowing for easy monolithic integration. However, to date, only two production methods for $Ge_{1-x}Sn_x$ NCs have been reported. Ruddy et al. utilized a wet chemical method to achieve $Ge_{1-x}Sn_x$ NCs with 1% Sn incorporation.[61] Cho et al. exploited the photolysis of gas phase precursors to produce $Ge_{1-x}Sn_x$ NCs with x = 1-5%, without the presence of β-Sn.[51] While both successfully incorporated Sn into nanocrystalline Ge, neither reported comprehensive studies to evaluate physical properties versus composition, nor achieved Sn concentrations required for indirect to direct transition observed in corresponding thin film nanostructures.[23, 24, 51, 61]

Herein, we report a wet-colloidal strategy to produce high quality $Ge_{1-x}Sn_x$ NCs with sizes in the range of 15–23 nm and 3.4–4.6 nm and wider tunability of Sn compositions (x=0.000–0.279). We show by controlling the precursor concentration and reduction temperature, a method has been developed to produce homogenous $Ge_{1-x}Sn_x$ nanoalloys devoid of elemental Sn impurities. The larger $Ge_{1-x}Sn_x$ NCs (15–23 nm) exhibit a non-linear expansion of the Ge lattice owing to lattice mismatch and possible strain effects, but exhibit weak confinement effects. In contrast, smaller $Ge_{1-x}Sn_x$ NCs (3.4–4.6 nm)

display strong size confinement with composition tunable indirect energy gaps from 1.31 to 0.75 eV and direct energy gaps from 1.47 to 0.95 eV (x=0.00–0.116). Interestingly, as-synthesized $Ge_{1-x}Sn_x$ nanoalloys demonstrate high thermal stability and moderate resistance against sintering up to 400–500°C.

3.2 EXPERIMENTAL SECTION

3.2.1 Materials.

Germanium diiodide (99.99+ %) and tin dichloride (>99.9985 % Ultra Dry) were purchased from Strem and Alfa Aesar, respectively. Germanium tetraiodide (>95%) was purchased from Gelest. N-butyllithium (BuLi) 1.6 M in hexane, 1-octadecene (ODE, 90%), and oleylamine (OLA, 80-90%) were purchased from Acros. Common solvents such as toluene, chloroform, acetone, carbon tetrachloride, and methanol were ACS grade and purchased from Fisher or Acros. A Schlenk line was utilized to dry OLA and ODE by heating at 120 °C under vacuum for one hour, dried solvents were then stored under N_2 atmosphere. Methanol and acetone were dried over molecular sieves prior to use. All other solvents were used as received. (*Caution: Alkyl-lithium compounds such as n-butyllithium are highly reactive pyrophoric chemical. Only properly trained personnel should handle these chemicals under strict air free protocol.*)

3.2.2 Synthesis of Ge NCs.

The single element Ge NCs were prepared by employing a modified literature procedure.[64] Briefly, in 4 mL of OLA, different ratios of GeI_2/GeI_4 were loaded according to the desired NC size: 0.6 mmol of GeI_4 was used to produce 3.4 ± 0.40 nm NCs and

0.03 mmol of GeI_2/0.57mmol of GeI_4 for 23 nm NCs.[64] Reactants were mixed in a N_2 glove box and sealed in a 3-neck flask with a condenser, septum, and thermocouple attached before transferring to a Schenk line and connecting to a digitally controlled heating mantle. The mixture was then degased under vacuum at 115 °C for 15 min., followed by switching to N_2 flow and outgassing through an oil bubbler for additional 15 min., prior to increasing the temperature to 200 °C. Immediately upon reaching 200 °C, a stock solution of 0.9 mL BuLi in 3 mL of ODE, sealed in an air tight vial was injected. The reaction mixture was then heated to 300 °C and held there for 1 h prior to isolation of the NCs.

3.2.3 Synthesis of $Ge_{1-x}Sn_x$ Alloy NCs.

In a typical synthesis of $Ge_{1-x}Sn_x$ nanoalloys, appropriate amounts of GeI_2 and $SnCl_2$ (Table 3.1) were combined in a 3-neck flask with either 20 mL (for 4.1–4.6 nm NCs) or 10 mL (for 15–17 nm NCs) of OLA. The set up was transferred out of the glove box, connected to a Schlenk line, and heated under vacuum to 120 °C to produce a homogeneous orange color solution. Then, the reaction was flushed with nitrogen for 15 min. and the temperature was ramped up to 230 °C, at which point 0.80 mL of BuLi in 3.0 mL of ODE (sealed in an air tight vial) was swiftly injected. The injection caused a temperature drop to ~210 °C and the mixture was reheated to 300 °C. Finally, the reaction was held at 300 °C for 0 and 10 min for the growth of 4.1–4.6 nm and 15–17 nm $Ge_{1-x}Sn_x$ NCs, respectively.

Table 3.1. The molar ratio of GeI_2 and $SnCl_2$ and corresponding concentrations of Sn used in the synthesis of 15–17 nm (10 mL of OLA) and 4.1–4.6 nm (20 mL of OLA) $Ge_{1-x}Sn_x$ alloy nanocrystals.

Nominal Composition	GeI_2 (mmol)	$SnCl_2$ (mmol)	10 mL OLA (µM Sn)	20 mL OLA (µM Sn)
$Ge_{0.98}Sn_{0.02}$	0.59	0.12	1.2	0.6
$Ge_{0.95}Sn_{0.05}$	0.57	0.03	3.0	1.5
$Ge_{0.90}Sn_{0.10}$	0.54	0.06	6.0	3.0
$Ge_{0.85}Sn_{0.15}$	0.51	0.09	9.0	4.5
$Ge_{0.80}Sn_{0.20}$	0.48	0.12	12.0	6.0
$Ge_{0.75}Sn_{0.25}$	0.45	0.15	15.0	7.5

3.2.4 Isolation and Purification.

Following the synthesis, the reaction flask was cooled by blowing compressed air until the temperature dropped below 120 °C, typically around 100-80 °C. The crude reaction mixture was transferred to a centrifuge tube containing 10 mL of toluene. Then, 60 mL of freshly distilled methanol was added and the mixture was centrifuged for 5 min to obtain a solid brown colored pellet. The supernatant was discarded and the precipitate was purified by dispersing in toluene and subsequent precipitation with a mixture of methanol/acetone (1:1 v:v) twice.

3.2.5 Characterization.

A PANanalytical X'Pert PRO X-Ray diffractometer calibrated with Si standard and equipped with a Cu Kα anode (κα= 1.54 Å) radiation was used for the powder X-ray

diffraction (PXRD) measurements. Purified NCs were deposited on to a low background sample holder and diffraction patterns were collected at 45 kV and 40 mA operating conditions. Crystallite size was estimated from the diffraction patterns using the Scherrer calculation[93] on the (111), (220), and (311) reflections, after making appropriate corrections for instrumental broadening using Si standard. Diffuse reflectance (DRA) and UV-visible-NIR absorption measurements were recorded using a Cary 6000i spectrophotometer (Agilent Technologies) in the double beam mode for solution measurements and using an internal DRA 2500 attachment for solid sample measurements mixed in a $BaSO_4$ matrix. Diffuse reflectance fast Fourier transform infra-red spectroscopy (DRFTIR) was performed using a Nicolet Nexus 670 FT-IR with an AVATAR diffuse reflectance accessory, on NC samples mixed with KBr powder. Raman spectra were taken with a Thermo Scientific DXR Smart Raman equipped with a 532 nm laser. X-ray photoelectron spectroscopy was performed using a Thermofisher ESCALAB 250 equipped with Al κα source; powdered samples were pressed on indium foil purchased from Sigma Aldrich. Elemental compositions were obtained by inductively coupled plasma optical emission spectroscopy (ICP-OES) and energy dispersive spectroscopy (EDS). EDS was obtained in a Hitachi FE-SEM Su-70 scanning electron microscope (SEM) operating at 20 KeV with an in-situ EDAX detector. Dried NCs were adhered to an aluminum stub with double sided carbon tape prior to the analysis. The Sn compositions were determined by averaging the atomic percentages of Sn acquired from 5 individual spots per sample. ICP-OES was performed with a Varian VISTA-MPX monitoring 5 wavelengths for both elements. For ICP-OES analysis, $Ge_{1-x}Sn_x$ NCs were dissolved by heating in a mixture of concentrated tartaric acid/nitric acid (2:1). Typically,

~1 mg of $Ge_{1-x}Sn_x$ NCs was loaded into a glass vial followed by 2.00 mL of concentrated tartaric acid and 1.00 mL of concentrated nitric acid. The mixture was heated for 2-5 hours until all the powder was dissolved. The calibration standards were purchased from Inorganic Ventures. Transmission electron micrographs (TEM) were recorded using a Zeiss Libra 120 microscope operating at an accelerating voltage of 120 kV. High resolution TEM (HRTEM) and scanning-TEM (STEM) analyses were performed on a FEI Titan 8300 electron microscope equipped with a Gatan 794 multi-scan camera operating at 300 kV. TEM samples were prepared by drop casting ~5 µL of NCs, dispersed in CCl_4, onto a carbon coated copper grids and evaporating the solvent. Thermogravimetric analyses (TGA) were performed on dry powders under nitrogen flow with a ramp rate of 10 °C/minute using a TA TGA (Q5000) instrument.

3.3 RESULTS AND DISSCUSION

3.3.1 Size Control and the Elimination of Metallic Sn Impurities.

The production of single element Ge NCs has been extensively studied over the years.[61, 64, 65, 92, 94-98] However, only two studies on the synthesis of $Ge_{1-x}Sn_x$ alloy NCs have been reported to date, neither of which provide an in-depth analysis on the nature of the binary nucleation.[51, 61] As such, following the work done by Ruddy et al.[61, 64] a colloidal synthetic strategy was developed to produce single element Ge and $Ge_{1-x}Sn_x$ alloy NCs. To eliminate the formation of undesirable β-Sn byproduct, control over nucleation and growth was achieved by reducing the probability of homogeneous Sn nucleation through increased solvent volume and rapid reduction of the metal precursors. As a solution of GeI_2 in oleylamine (OLA) was heated above 200 °C, it progressively

darkened from a light yellow to orange and then to deep red. The reddening of the solution is consistent with the formation of germanium amide-iodide complex.[64] Upon injection of the reducing agent, n-butyllithium (BuLi), at 230 °C the solution immediately turned brownish-red indicating the formation of Ge^o seed nuclei. As the temperature was increased to 300 °C, the solution lost its red tint and progressed to light or dark brown. The one hour that the solution was held at 300 °C was found necessary to provide sufficient crystallization for pure Ge NCs of all sizes. When introducing $SnCl_2$ into the system, dramatic changes in the nucleation and growth kinetics have occurred due to a) the large lattice mismatch between cubic Sn and Ge,[15] b) competition between homo-heterogeneous nucleation, c) the thermal stability of β-Sn versus that of α-Sn^{41} and d) lower crystallization temperature of Sn. It is assumed that the lattice mismatch between α-Sn and Ge is resolved in NCs due to the high fraction of surface atoms being able to expand or contract in order to tolerate the strain and the presence of capping ligands that can effectively stabilize the NC surface.

Recently, $Ge_{0.60}Sn_{0.40}$ NCs were produced by laser photolysis,[51] however significant amounts of β-Sn were present in the as-prepared samples. The highest concentration of Sn incorporated by photolysis without any β-Sn was x = 0.05.[51] We attribute this to the lack of control over the nucleation environment in the localized heating zone. Since α-Sn is not stable above 13 °C, it is essential that Sn does not form any stable nuclei or tetragonal β-Sn will preferentially grow instead of the Sn atoms incorporating into cubic Ge nuclei. A wet chemical synthesis has allowed us to overcome the formation of β-Sn by manipulating the nucleation stage of the synthesis. To ensure no Sn nuclei are formed, the overall concentration of $SnCl_2$ was kept low and the nucleation temperature was kept

slightly below the melting point of β-Sn. The low concentration of $SnCl_2$ has led to the formation of cubic $Ge_{1-x}Sn_x$ nanoalloys without any detectable Sn impurities. In this study, $SnCl_2$ concentrations (Table 3.1) used were 2–10 times lower than those employed by Ruddy et al. (~0.8–16.8 μM).[61] It is likely that the low concentration of $SnCl_2$ reduces the probability of homogeneous Sn nucleation. In contrast, at high concentration of Sn (>15.0 μM of $SnCl_2$), β-Sn was often formed (Figure 3.1) due to higher stability of β-Sn over α-Sn at high temperature conditions. Moreover, the rapid reduction of $SnCl_2$ by BuLi is found to be essential for the successful growth of homogenous nanoalloys. Increasing the nucleation temperature from 200 to 230 °C has sufficiently increased the reactivity of BuLi, which ensures the rapid and complete co-reduction of Ge and Sn precursors into homogeneous alloy nuclei. It is likely that the injection at 230 °C, just below the melting point of Sn, further reduces the probability for stable β-Sn nuclei to form. In addition, the 1 h. at 300 °C needed for sufficient crystallization of Ge NCs was unnecessary for $Ge_{1-x}Sn_x$ nanoalloys. Since the time required to ramp the temperature from 210 to 300 °C (~7–8 min) has proved sufficient to produce highly crystalline $Ge_{1-x}Sn_x$ nanoalloys, it is likely that Sn reduces the energy required for crystallization and growth events relative to those of pure Ge.
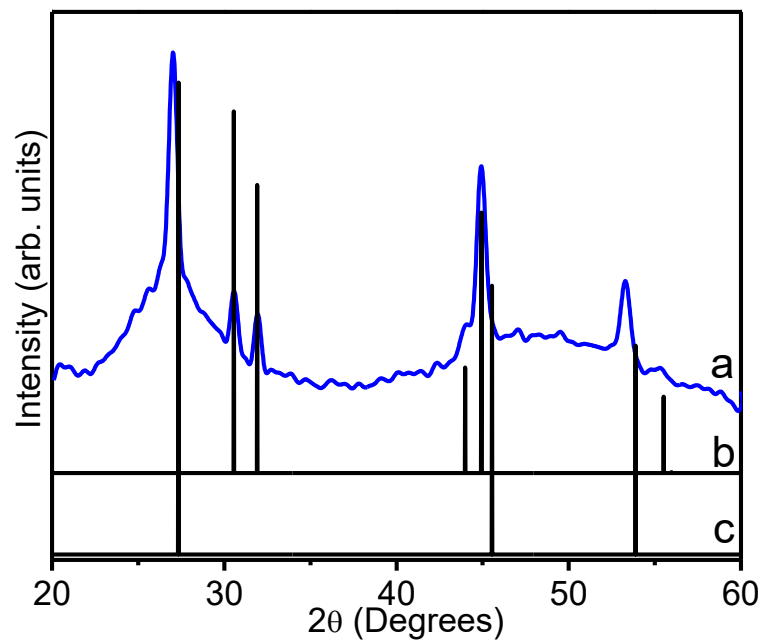
Figure 3.1. (a) Powder X-ray diffraction pattern of the $Ge_{1-x}Sn_x$ nanocrystals prepared by reduction of GeI_2 and $SnCl_2$ in 4 mL of oleylamine (Sn concentration =16.8 μM) at 200 °C. High concentrations of Sn (>15 μM) leads to phase segregation and formation of thermodynamically stable β-Sn impurities. The PDF patterns of (b) tetragonal β-Sn (PDF# 00-004-0673) and (c) cubic Ge (PDF# 01-089-5011) and are also shown.

Scheme 3.1. An illustration of the synthesis of $Ge_{1-x}Sn_x$ alloy NCs. Fast chemical co-reduction of precursor halides dissolved in oleylamine (OLA), followed by the growth of resulting alloy nuclei at 300ºC has been successfully utilized to produce homogeneous $Ge_{1-x}Sn_x$ nanoalloys.

GeI$_2$
SnCl$_2$ GeI$_2$
GeI$_2$ GeI$_2$
GeI$_2$
GeI$_2$ SnCl$_2$
GeI$_2$

GeI$_2$ and SnCl$_2$
in OLA [Sn]<15.0 μM

230 °C

GeI-NHR
SnCl$_2$ GeI$_2$
Ge(NHR)$_2$
SnI-NHR
GeI$_2$

Ge/Sn-amide
complexes

BuLi + ODE

Ge^0 Ge^0 Ge^0
Sn^0 Ge^0
Ge^0 Ge^0 Ge^0
Ge^0 Sn^0

$Ge_{1-x}Sn_x$ seed nuclei
~205-215 °C

300 °C
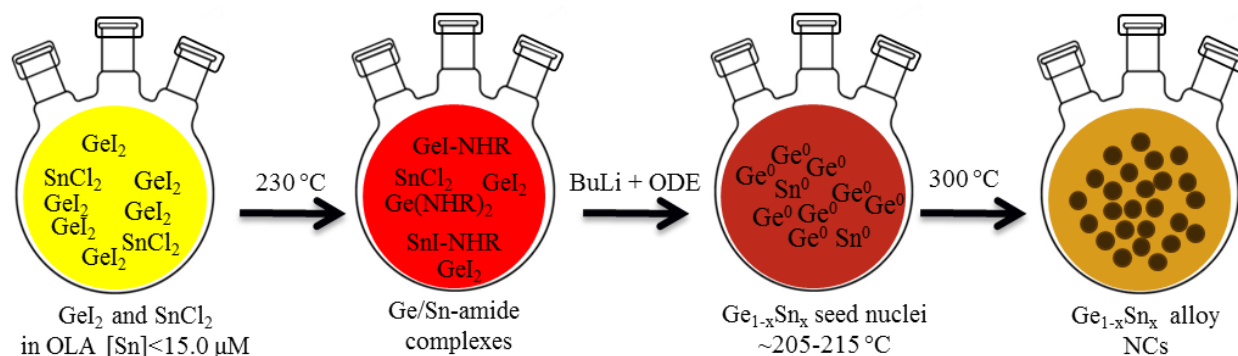
$Ge_{1-x}Sn_x$ alloy
NCs

3.3.2 Structural Properties and Thermo-Stability of $Ge_{1-x}Sn_x$ Nanoalloys.

Initially, NCs with crystal size ranging from 15–17 nm were produced to adequately study the changes in structural characteristics. Subsequently, the efforts were shifted to produce smaller NCs (3.4–4.6 nm) to probe both the effects of quantum confinement and Sn alloying on optical properties. Phase pure $Ge_{1-x}Sn_x$ NCs (15–17 nm) with compositions in the range of x=0.050–0.279 were successfully produced by co-reduction of GeI$_2$ and SnCl$_2$ at 230 °C, followed by the growth of resulting nuclei at 300 °C for 10 min (Table 3.1). To confirm the structural homogeneity of alloy NCs and the absence of the undesirable by-products, Powder X-ray diffraction (PXRD) was utilized. Diffraction patterns suggest the incorporation of Sn into Ge, based on an expansion of the cubic Ge lattice (Vegard's Law).[19] This effect has been clearly observed *via* a shift in Bragg reflections to lower 2θ angles with increasing Sn composition (Figure 3.2A). However, the NCs do deviate from Vegard's Law, which can be attributed to minor strain in the Ge$_1$-

$_x$Sn$_x$ alloy lattice possibly caused by the alloy disorder.[86, 99] Occasionally, a small peak is observed near 26° 2θ, attributable to GeO$_2$, which we ascribe to surface oxidation. The lattice parameters calculated from PXRD patterns are shown in Figure 3.2B and Table 3.2 further reflecting an expansion of the cubic Ge lattice.
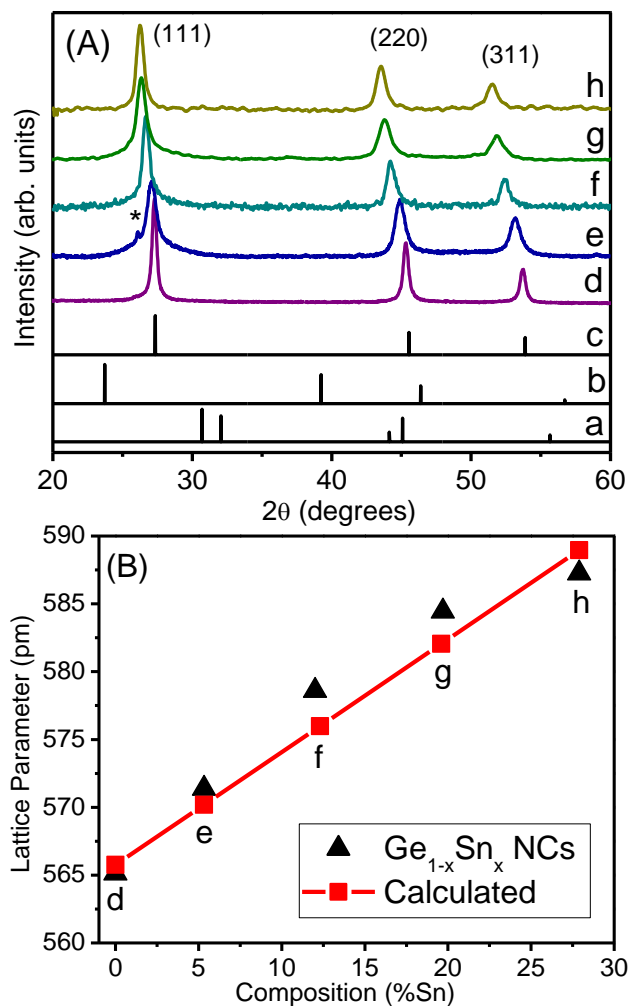
Figure 3.2. (A) PXRD patterns of the diamond-like cubic $Ge_{1-x}Sn_x$ NCs with crystallites in the range of 15–23 nm: (a) β-Sn PDF# 00-004-0673 (b) α-Sn PDF# 01-086-2266 (c) Ge PDF# 01-089-5011, (d) x=0.000, (e) x= 0.050, (f) x=0.120, (g) x=0.197, (h) x=0.279. Elemental compositions were obtained from inductively coupled plasma optical emission spectroscopy (ICP-OES). Occasionally, a small peak is observed at 2θ =26.1° that can be attributed to minor degree of GeO_2 formation from surface oxidation. (B) A plot illustrating the lattice parameters obtained for $Ge_{1-x}Sn_x$ alloy NCs (black triangles) based on PXRD patterns and theoretical lattice parameters calculated based on the composition using Vegard's law[19] (red squares).

Table 3.2. Elemental composition and crystallite size of larger (15-23 nm) $Ge_{1-x}Sn_x$ alloy nanocrystals prepared by co-reduction of GeI_2 and $SnCl_2$ in 10 mL of oleylamine at 230 °C followed by growth at 300 °C for 10 min. Lattice parameters calculated based on the diffraction patterns are also shown.

Sample	Sn composition (x)[a]	Atomic % Sn[b]	Crystallite Size[c] (nm)	Lattice Parameter (Å)
Ge	0	0	23.1	565
$Ge_{0.950}Sn_{0.050}$	0.050 ±0.006	5.32 ±0.61	17.1	571
$Ge_{0.880}Sn_{0.120}$	0.120 ±0.006	8.20 ± 0.70	16.2	578
$Ge_{0.803}Sn_{0.197}$	0.197 ± 0.005	13.74 ± 1.40	15.8	584
$Ge_{0.721}Sn_{0.279}$	0.279 ±0.004	23.21± 0.85	15.7	587

[a] Elemental compositions were obtained as mol % Sn from ICP-OES averaging 3 measurements per sample.

[b] Atomic compositions were obtained from SEM/EDS, atomic percentage averaged from 5 spots per sample.

[c] Calculated using the Scherer equation after applying appropriate correction for instrumental broadening using a Si standard.

Raman spectroscopy was employed to further study the effects of Sn alloying on NC lattice. Bulk Ge exhibits a Raman peak at 300 cm^{-1} that corresponds to the LO phonon mode of Ge-Ge bonds. The incorporation of Sn causes a red shift of Ge-Ge optical phonon mode due to the heavier Sn atoms and longer Ge-Sn bonds, with a linear dependence on Sn composition expected for strain free $Ge_{1-x}Sn_x$ alloys.[23, 86, 99] In contrast, pure Ge NCs exhibit a Raman peak at 293.6 cm^{-1} in close agreement with the confinement induced shifting of Ge-Ge phonon mode as reported in the literature.[100] Therefore, the combined effects of quantum confinement and Sn induced shifting cannot be decoupled preventing quantification of any strain present in the alloy lattice. However, a clear red shift of the Ge-Sn phonon mode (292.2-286.7 cm^{-1} for x = 0.050-0.279) is observed with increasing Sn content for alloy NCs with similar diameters (15-17 nm), which is likely attributed to strain in the alloy lattice (Figure 3.3). The broadening of Ge-Sn peak is consistent with the increasing alloy disorder with increasing Sn composition.[86, 99] Currently, further studies are under way to better control and understand the strain in as-prepared nanoalloys *via* post synthetic modification. Moreover, no specific signals were observed in the Raman spectra that correspond to surface ligands (Figure 3.4). Nonetheless, two broad Raman bands were observed at 1347 cm^{-1} and 1570 cm^{-1}, which can be attributed to amorphous carbon produced via laser induced decomposition of the organic surfactants.[101] Consistent with PXRD analysis, the minor peaks observed at 437 cm^{-1}, 550 cm^{-1}, and 880 cm^{-1} are assigned to small amount of GeO_2 produced via surface oxidation.[102] However, peaks corresponding to SnO_x species were not found in any of the NC samples.
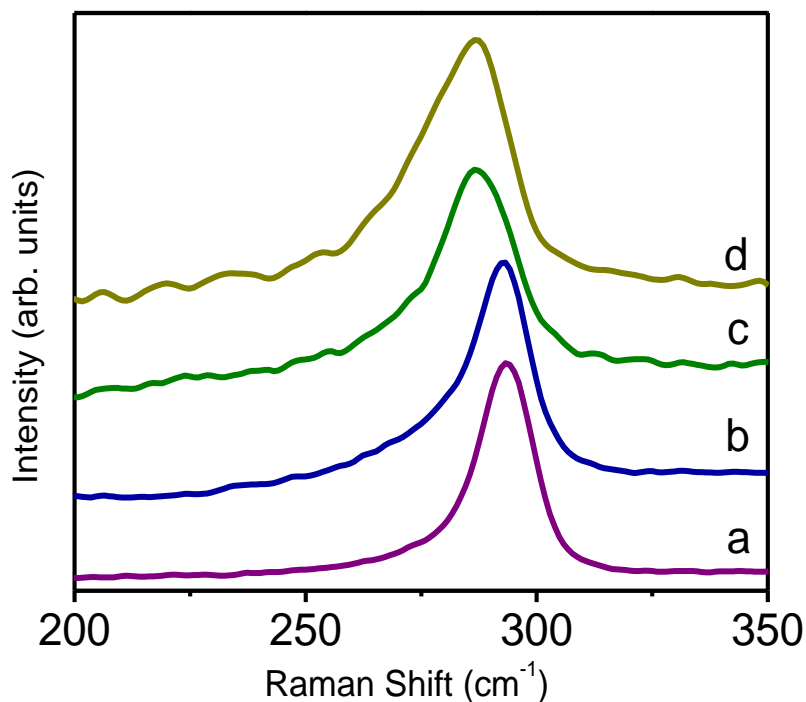
Figure 3.3 Raman spectra of $Ge_{1-x}Sn_x$ alloy NCs with crystallite size in the range of 15-17 nm and varying Sn compositions: (a) x= 0.000, (b) x= 0.050, (c) x= 0.120 and (d) x= 0.279. Elemental compositions were obtained from ICP-OES. Spectra are normalized to clearly demonstrate the shifting of LO phonon mode of Ge-Ge and Ge-Sn bonds.
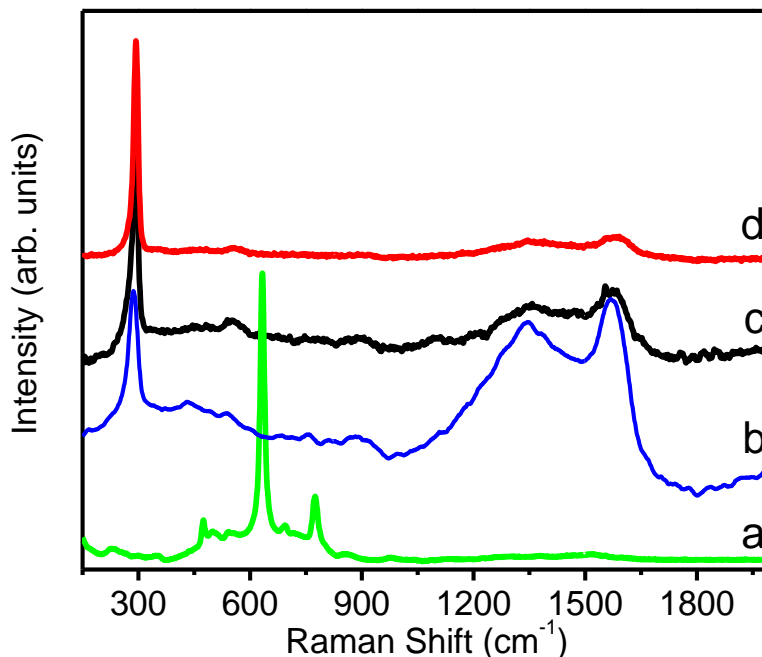
Figure 3.4. Raman spectra of (a) SnO_2 powder (> 99.99% obtained from Sigma-Aldrich) along with $Ge_{1-x}Sn_x$ nanocrystals with crystallite size in the range of 15-23 nm and Sn compositions of (b) x = 0.279, (c) x = 0.050, and (d) x = 0.00. The elemental compositions were obtained from ICP-OES analysis.

It is significant to note that the diffraction patterns suggest that even in the NCs with a high Sn content (x=0.279), only cubic $Ge_{1-x}Sn_x$ peaks are present and both α-Sn and β-Sn are not detected. This represents the highest Sn composition achieved for $Ge_{1-x}Sn_x$ NCs without phase segregation.[51, 61] Lack of Bragg reflections corresponding to α- or β-Sn suggests that the NCs are homogenous alloys and not core/shell-type heterostructures. Furthermore, since β-Sn has a low crystallization temperature it is expected that if any Sn had formed on its own it would be highly crystalline. As such, the potential for the presence of amorphous Sn is extremely low. However, we did observe the growth of β-Sn through PXRD similar to the previous reports on $Ge_{1-x}Sn_x$ NCs[51, 61]

(Figure 3.1). Details about the factors that led to successful elimination of β-Sn are discussed in the previous section. While those previous studies achieved x=0.01 and x=0.05 $Ge_{1-x}Sn_x$ without β-Sn, the colloidal route reported here has accomplished Sn concentrations as high as x=0.279 for phase pure $Ge_{1-x}Sn_x$ nanoalloys. Low resolution transmission electron microscopy (LRTEM) images of 15–17 nm NCs indicate wide dispersity of spherical particles. Two distinct populations of NCs were observed in the as-prepared samples (Figure 3.5), larger NCs ranging from 10–20 nm and smaller NCs ranging from 2–6 nm. The formation of two populations could be a result of smaller particles being formed during the rapid nucleation process and incomplete growth into larger crystallites during the shorter growth time (10 min.) employed in the synthesis.
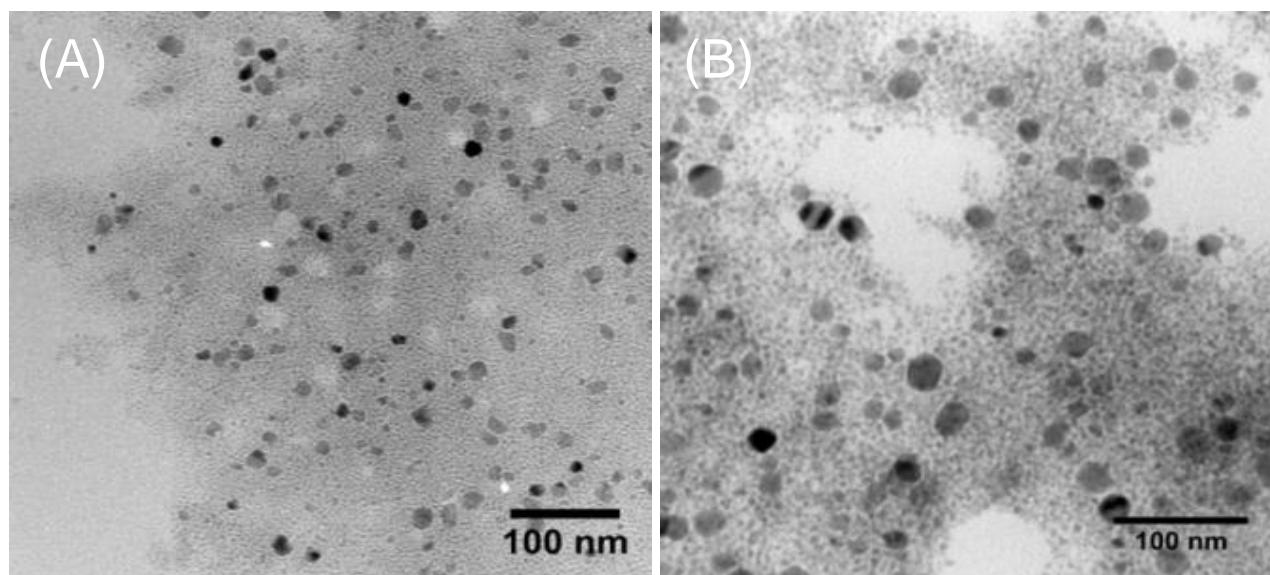
Figure 3.5. Transmission electron micrographs of the larger $Ge_{0.880}Sn_{0.120}$ alloy nanocrystals prepared by co-reduction of GeI_2 and $SnCl_2$ in 10.0 mL of oleylamine at 230 °C (A, B). Samples were polydisperse with two distinct populations of NCs: larger NCs with size ranging from 10–23 nm and smaller NCs with size in the range of 2–6 nm.

The solid state DRFTIR spectra obtained for as-prepared alloy NCs (15–23 nm) were converted to absorption using the Kubelka-Munk remission function.[71, 77] The incorporation of Sn significantly red shifts the absorption band onsets of $Ge_{1-x}Sn_x$ NCs relative to single element Ge NCs (Figure 3.6). Mid IR bandgaps of 0.41–0.26 eV were obtained for x= 0.120–0.279 at crystallite sizes of 15–17 nm, suggesting weak or no confinement effects in this size regime. Hence, efforts were focused on the synthesis of significantly smaller NCs without the presence of larger crystallites to investigate both the effects of quantum confinement and Sn alloying. Nevertheless, the successful synthesis of larger NCs suggests that the synthetic strategy reported herein produces homogeneous $Ge_{1-x}Sn_x$ nanoalloys without the presence of undesired metallic impurities.
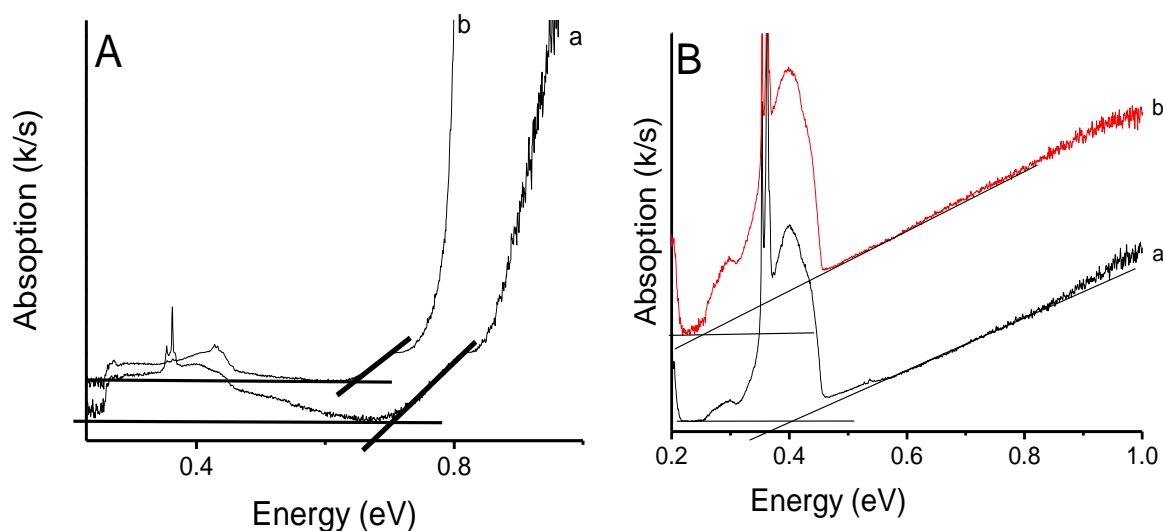
Figure 3.6. (A) Diffuse reflectance FTIR spectra (converted to absorption using Kubelka-Munk remission function) for (a) Ge nanocrystals (~23 nm, bandgap ≈0.70 eV) and the (b) bulk Ge powder (purchased from Sigma Aldrich, bandgap ≈0.64eV) along with (B) 15-17 nm $Ge_{1-x}Sn_x$ alloy nanocrystals displaying (a) x=0.120 (bandgap ≈0.41 eV) (b) $Ge_{1-x}Sn_x$ x=0.279 (bandgap ≈0.26 eV). Pronounced peaks observed in the 0.2-0.5 eV are attributed to amine and alkene groups of the surfactant ligands (oleylamine and octadecene) used in the synthesis.

To provide further evidence that $Ge_{1-x}Sn_x$ NCs are free from Sn segregation, scanning TEM- energy dispersive spectroscopy (STEM-EDS) elemental line scans were recorded to confirm the compositional uniformity of nanoalloys. The dark and bright field STEM images and the corresponding elemental line scan recorded from a single $Ge_{0.890}Sn_{0.110}$ NC are shown in Figure 3. Additional lines scans are presented in Figure 3.7. No spikes in Sn composition were detected in any of the NCs examined indicating that Sn is evenly distributed throughout the nanocrystalline $Ge_{1-x}Sn_x$ lattice (Figure 3.8C). Similar results were obtained from alloy NCs with other compositions supporting the view that $Ge_{1-x}Sn_x$ nanoalloys obtained from this route are homogeneous solid solutions. In addition, the HRTEM image of the corresponding $Ge_{0.890}Sn_{0.110}$ alloy NC indicates a (111) lattice spacing of 3.4 Å, which is slightly larger than that of pure Ge (3.3 Å)[64] further confirming the expansion of cubic Ge lattice (Figure 3.8A).
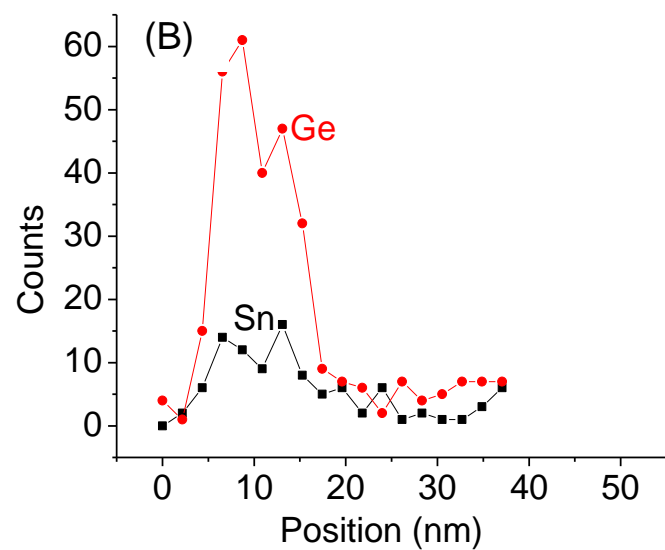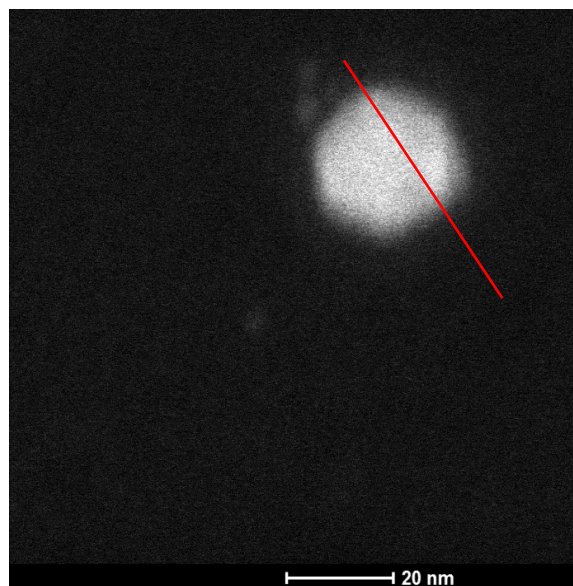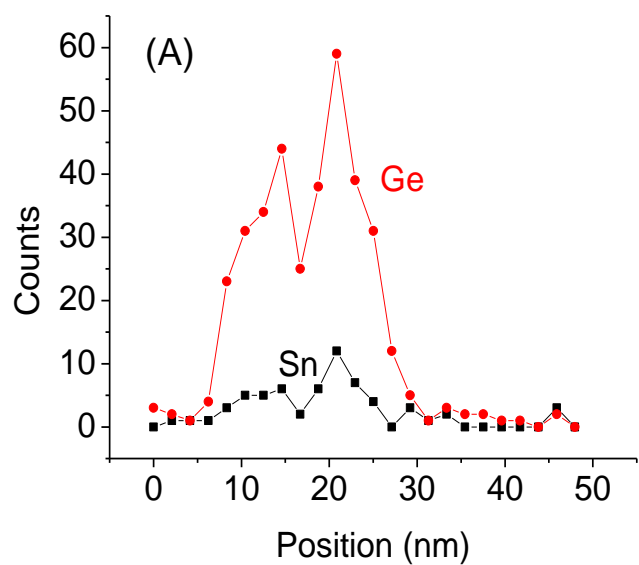
Figure 3.7. The STEM-EDS line scans of (A) $Ge_{0.890}Sn_{0.110}$ and (B) $Ge_{0.803}Sn_{0.197}$ alloy NCs indicating no inconsistences between Ge and Sn distributions throughout the nanocrystalline Ge lattice. The corresponding dark field STEM image is shown to the right.
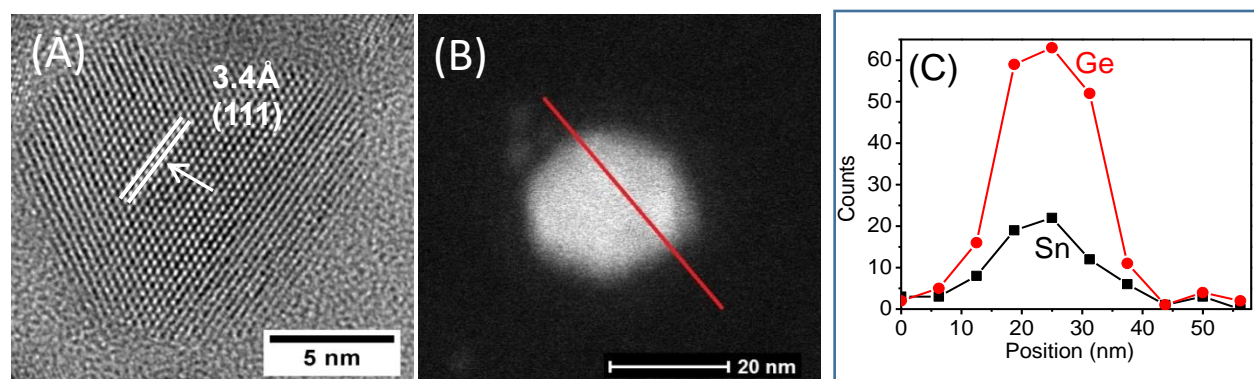
Figure 3.8. (A) The bright and (B) dark field high resolution TEM images of $Ge_{0.890}Sn_{0.110}$ alloy NCs. (C) STEM-EDS line scan showing the compositional ratio of Ge and Sn is consistent across the entire particle.

X-ray photoelectron spectroscopy (XPS) was used to examine the surface species of $Ge_{1-x}Sn_x$ nanoalloys. A typical XPS spectrum of $Ge_{1-x}Sn_x$ NCs is shown in Figure 4A depicting the Ge 3d region. The peak at 28.6 eV corresponding to Ge^0 ($3d_{5/2}$ and $3d_{3/2}$) is shifted from the expected value of 29.4 eV[103] likely due to surface charging effects commonly observed in semiconductor NCs.[104] Higher energy peak at 30.8 eV (Ge 3d) is likely to arise from surface Ge atoms coordinated to passivating organic ligands. The peak at 34.0 eV (Ge 3d) is attributed to minor amount of GeO_2 produced via surface oxidation.[23] The broad nature of the 30.8 eV peak (full width at the half maximum = 2.44 eV) suggests multiple oxidation states, Ge^{1+} (30.3 eV), Ge^{2+} (31.4 eV) Ge^{3+} (32.4 eV), resulting from multimodal binding of ligands to surface species, with the possible presence of Ge-C, Ge-N, Ge=C and Ge=N bonds.[103, 105] Similar behavior has been observed in the Sn 3d region (Figure 3.8B). Sn^0 is present as indicated by the peaks at 484.2 eV and 492.7 eV that corresponds to Sn $3d_{5/2}$ and Sn $3d_{3/2}$ binding energies, respectively.[106] Peaks at 486.5 eV and 494.9 eV corresponding to Sn $3d_{5/2}$ and $3d_{3/2}$ indicate the presence of Sn^{2+} and

72

Sn^{4+} on the NC surface suggesting that surface Sn atoms are also passivated with stabilizing ligands. While minor GeO$_2$ impurities have been detected through PXRD analyses (Figure 3.2A), no SnO$_x$ species has been detected in the Raman spectra of corresponding samples (Figure 3.4). Despite the use of rigorous air free synthetic procedures, it is suspected that the formation of GeO$_2$ occurs during ambient isolation and purification of NCs as weakly bound surfactant ligands can be lost via excessive washing and centrifugation.[65]
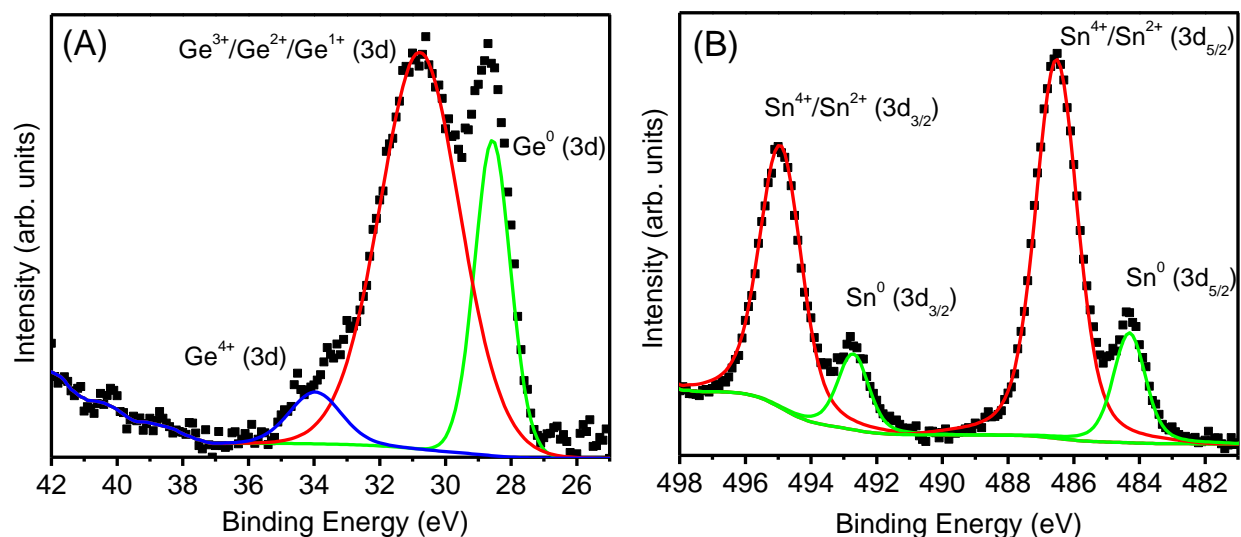
Figure 3.9 (A) Ge 3d and (B) Sn 3d XPS spectra of Ge$_{0.721}$Sn$_{0.279}$ alloy NCs. Dotted lines represent the spectral data. The green lines are fitted peaks for Ge^0/Sn^0 species and the red lines are fitted peaks to different oxidation states of surface speciation and the blue line is fitted to suspected surface oxidation.

To investigate the nature of the ligand coverage on the NC surface, thermogravimetric analysis (TGA) was employed. Samples were loaded onto platinum pans under ambient conditions and heated at 10 °C min^{-1} up to 600 °C under N$_2$ flow. Three major weight

losses were observed at 100-150 ºC, 200-300 °C, and 340-410 ºC (Figure 3.10). The weight loss up to 150 °C is attributed to trapped moisture whereas from 200-300 °C is attributed to butyl groups bound to the NC surface. The largest desorption event takes place from 340–410 °C consistent with OLA acting as the major capping ligand.[107] Surprisingly, the PXRD analysis of the annealed samples revealed that NCs heated to 600°C were free of Sn segregation (Figure 3.11A). However, significant growth of GeO_2 had occurred, which likely provided a barrier against Sn segregation. Despite TGA being carried out under a flow of inert gas, it is suspected that the oxide formation is a direct result of moisture trapped in the NC powder from being exposed to ambient conditions.

To further study the thermal stability of $Ge_{1-x}Sn_x$ NCs without any capping oxide formation, a systematic annealing study under rigorous inert conditions was implemented. Dried NC powders were thoroughly degassed in a vacuum chamber and stored in a N_2 atmosphere for 1 week prior to being inserted into a tube furnace under high purity argon. The samples were introduced 200 °C below the final temperature and ramped to a desired holding temperature for 30 min. prior to being cooled to room temperature. PXRD patterns of the annealed samples (Figure 3.11B) indicate that $Ge_{1-x}Sn_x$ NCs undergo minimal crystal growth and no Sn segregation up to 400-500 °C. However, the segregation of Sn is clearly observed at 600 °C and 700 °C *via* the evolution of diffractions from the (200) and (101) planes of β-Sn (PDF# 00-004-0673, Figure 3.11B). It is significant to note that the NCs heated at 400 °C for 30 min. exhibit minimal sintering, 13.3 nm as-prepared to 15.4 nm post annealed, as determined by Scherrer equation. The only significant change to the NC structure at 400 °C is the relaxation of tensile strain of the Ge lattice and the development of compressively strained $Ge_{1-x}Sn_x$,[86] indicated by the shift in diffraction

peaks to higher Bragg angles (Figure 3.11B). Based on TGA data performed under similar experimental conditions (Figure 3.10), the NC surface should be free of ligands above 400 °C allowing for direct contact between particles without the loss of the desired properties.
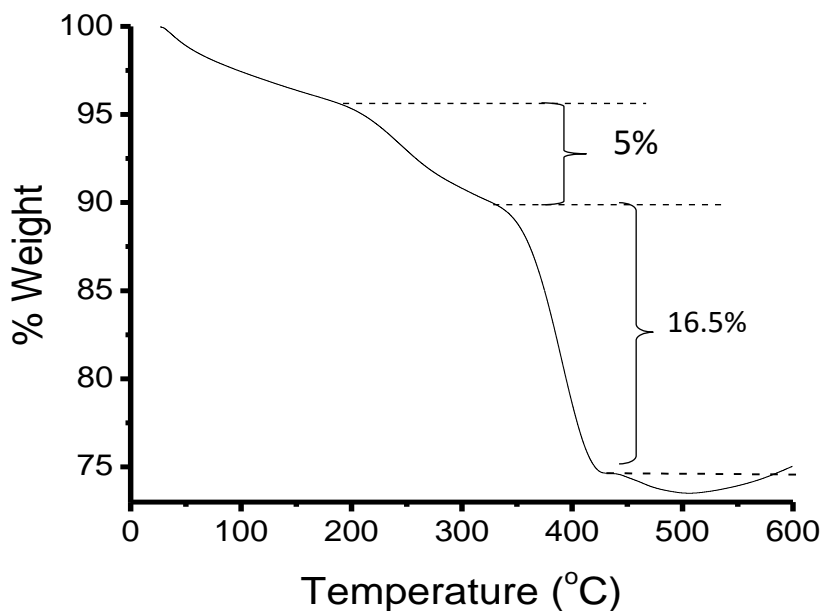
Figure 3.10 A representative thermogravimetric plot of $Ge_{0.908}Sn_{0.092}$ alloy NCs. Weight loss up to 150 °C is attributed to trapped moisture, from 200-300 °C is attributed to butyl groups bound to the NC surface and from 350-450 °C is attributed to oleylamine and octadecene passivating ligands.
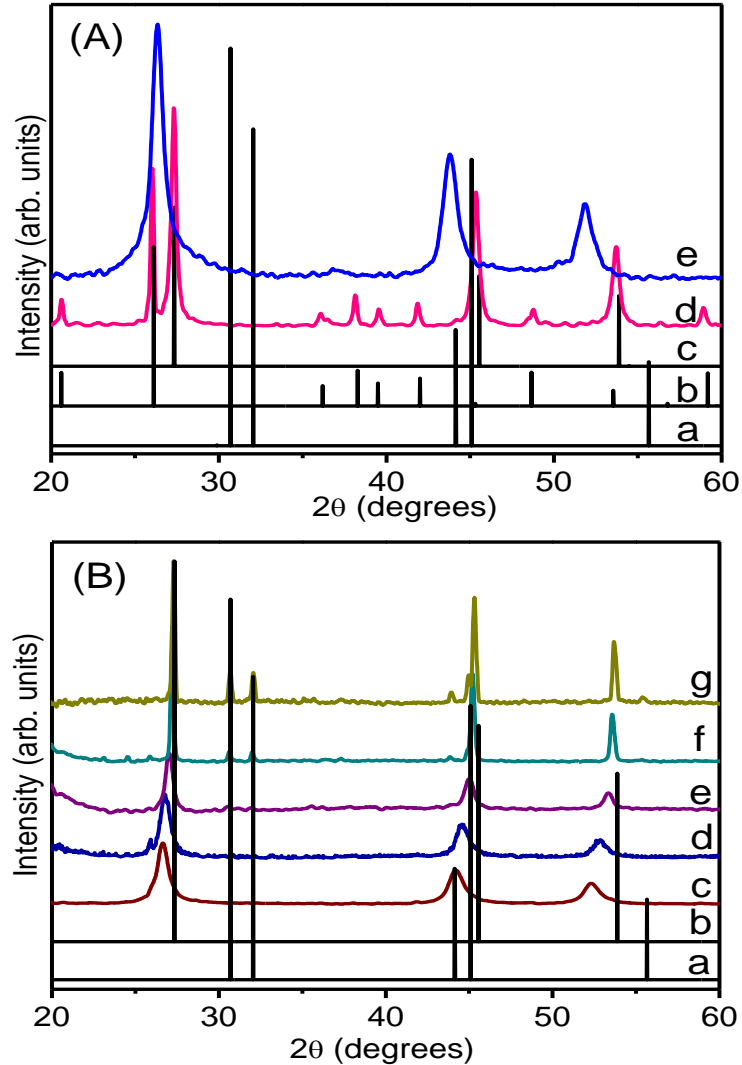
Figure 3.11 (A) $Ge_{0.860}Sn_{0.140}$ NCs (size=15.9 nm) heated during TGA undergo significant sintering and oxidation but no Sn segregation. (a) β-Sn PDF# 00-004-0673, (b) GeO_2 PDF# 00-036-1463, (c) Ge PDF# 01-089-5011 along with PXRD patterns of $Ge_{0.860}Sn_{0.140}$ NCs (d) post and (e) pre-TGA annealing. (B) A systematic rigorous air free annealing study on $Ge_{0.860}Sn_{0.140}$ NCs (starting crystallite size=13.3 nm) monitored by PXRD showing the thermo-stability of samples up to 400 °C. (a) (β-Sn PDF# 00-004-0673), (b) (Ge PDF# 01-089-5011), (c) as-prepared NCs, along with NC annealed at (d) 400, (e) 500, (f) 600, and (g) 700 °C.

In addition, elemental analysis of the annealed samples indicates no loss of Sn after the heating profiles. It should be noted that the ability to remove ligands with minimal changes to properties is highly advantageous for the fabrication of self-assembled NC thin films for future device applications.

3.3.3 Confinement Effects and Compositional Dependent Optical properties.

To systematically study the effects of quantum confinement across different concentrations of Sn, a set of significantly smaller $Ge_{1-x}Sn_x$ nanocrystallites were produced with average size in the range of 3.4–4.6 nm. The successful elimination of the larger NCs from the system was accomplished through lowering the concentration of the metal precursor by increasing the solvent (OLA) volume, which further reduces the probability of Sn atoms forming homogeneous nuclei and subsequent growth into β-Sn particles. Additionally, it is noted that as more Sn is incorporated into the reaction mixture the catalytic effects of Sn increases resulting in wider size dispersity than desired. Currently studies are being performed to improve the synthesis for specific Sn concentrations so that better size and dispersity control may be achieved. Nevertheless, this section investigates the evolution of the nature and energy of the bandgaps of as-prepared $Ge_{1-x}Sn_x$ NCs as a function of Sn composition. For the ease of comparison, the smaller $Ge_{1-x}Sn_x$ nanoalloys are abbreviated numerically as (1) x=0.000, (2) x=0.033, (3) x=0.056, (4) x=0.077, (5) x=0.088, (6) x=0.092, (7) x=0.116 as shown in Table 3.3. The phase purity of smaller $Ge_{1-x}Sn_x$ NCs is confirmed by PXRD, which shows only the Bragg reflections corresponding to diamond-like cubic structure and no detectable diffraction corresponding to GeO_2, β-Sn, or any other impurities (Figure 3.12). Significant line

broadening is evident as a result of Scherrer scattering consistent with the smaller NCs produced. Diffractions corresponding to the (220) and (331) planes of cubic Ge exhibit minor overlap owing to the combined scattering from each plane. The broad nature of the Bragg reflections makes it difficult to observe a systematic shift in the diffraction angles expected from the incorporation of Sn. However, the examination of 15–23 nm $Ge_{1-x}Sn_x$ NCs produced by employing a similar synthesis suggests that smaller $Ge_{1-x}Sn_x$ nanocrystallites are likely to exhibit a similar shift in Bragg reflections as a function of Sn composition (Figure 3.2). To further investigate the size, shape, and composition of smaller $Ge_{1-x}Sn_x$ nanoalloys TEM was employed.

The primary particle sizes of the smaller $Ge_{1-x}Sn_x$ nanoalloys were obtained from TEM analysis providing evidence that the formation of larger NCs has been successfully eliminated or reduced for all samples (Figure 3.13). In general, as-synthesized NCs are spherical in morphology and are narrowly dispersed with size in the range of 3.4–4.6 nm. The size histograms of $Ge_{1-x}Sn_x$ NCs without any post synthetic size selection are shown in Figure 3.14. The effects of increasing Sn concentration on nucleation and growth of nanoalloys can be clearly observed through changes in size dispersity and increase in average particle size. Pure Ge NCs 3.4 ± 0.4 nm, sample (1), are narrowly dispersed and primarily consist of spherical crystallites (Figure 3.13A). Introduction of even low concentrations of Sn, results in significant changes to size dispersity, and this effect worsens as higher levels of Sn are incorporated. Figure 3.13B and 3.13C correspond to

Table 3.3 Comparison of the elemental composition, crystallite and primary particle sizes, and optical band gaps from $(h\nu\alpha)^2$, $(h\nu\alpha)^{1/2}$, corresponding to direct and indirect electronic transitions, along with band energies obtained from Kubelka-Munk (KM) function for 3.4-4.6 nm $Ge_{1-x}Sn_x$ NCs.

Sample	Sn composition ICP-OES (x)[a]	Atomic % Sn SEM/EDS[b]	Particle Size (nm)[c]	Crystallite size (PXRD)[d]	$(h\nu\alpha)^2$ E_g (eV)[e]	$(h\nu\alpha)^{1/2}$ E_g (eV)[e]	(KM) E_g (eV)[e]
1	0.000	0.000	3.4 ± 0.4	2.3 ± 0.2	1.47	1.31	1.29
2	0.033 ± 0.007	0.030	4.1 ± 0.8	2.9 ± 0.2	1.53	1.23	1.15
3	0.056 ± 0.002	0.044	4.0 ± 0.8	2.9 ± 0.2	1.43	1.20	1.08
4	0.077 ± 0.008	0.064	4.3 ± 1.2	3.2 ± 0.2	1.51	1.59	0.99
5	0.088 ± 0.012	0.073	4.1± 1.0	3.4 ± 0.2	1.39	1.39	0.88
6	0.092 ± 0.014	0.089	4.3 ± 1.4	3.7 ± 0.3	1.15	1.15	0.75
7	0.116 ± 0.017	0.110	4.6 ± 1.2	2.6 ± 0.2	0.95[f]	0.75[f]	n/a[f]

[a] Elemental compositions were obtained as mol % Sn from ICP-OES averaging 3 individual measurements per sample.

[b] Atomic compositions were obtained from SEM/EDS, atomic percentage averaged from 5 spots per sample.

[c] Average particle size was calculated from counting 125-150 individual NCs from TEM images.

[d] Calculated using the Scherer equation[93] after applying appropriate correction for instrumental broadening using a Si standard.

[e] Optical bandgaps were estimated from extrapolating the first major absorption onset to the intersection point of the baseline using linear fits.[71, 72, 108]

[f] Onset cut off by detector limitation.
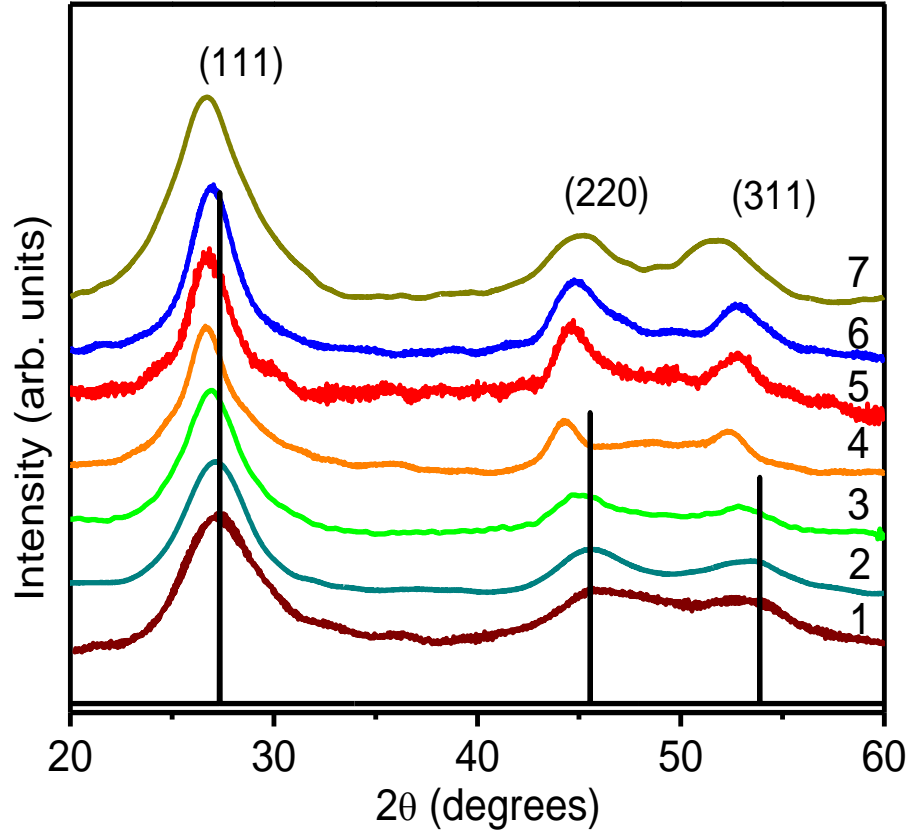
Figure 3.12 Power X-ray diffraction patterns of 3.4–4.6 nm $Ge_{1-x}Sn_x$ NCs with Sn compositions ranging from (1) x=0.000, (2) x=0.033, (3) x=0.056, (4) x=0.077, (5) x=0.088, (6) x=0.092, (7) x=0.116. The cubic Ge reference pattern (PDF# 01-089-5011) is shown as vertical black lines.

samples (2) and (3) respectively, particles are spherical but size dispersity has slightly increased relative to sample (1). Furthermore, at higher Sn concentrations it is apparent that the dispersity further increases, as seen in Figure 3.13D, 3.13E, and 3.13F. Nonetheless, the HRTEM studies suggest that $Ge_{0.884}Sn_{0.116}$ NCs are single crystalline with a lattice spacing of 3.4 Å (Figure 3.13H), which is consistent with an expanded (111) plane of cubic Ge (3.3 Å).
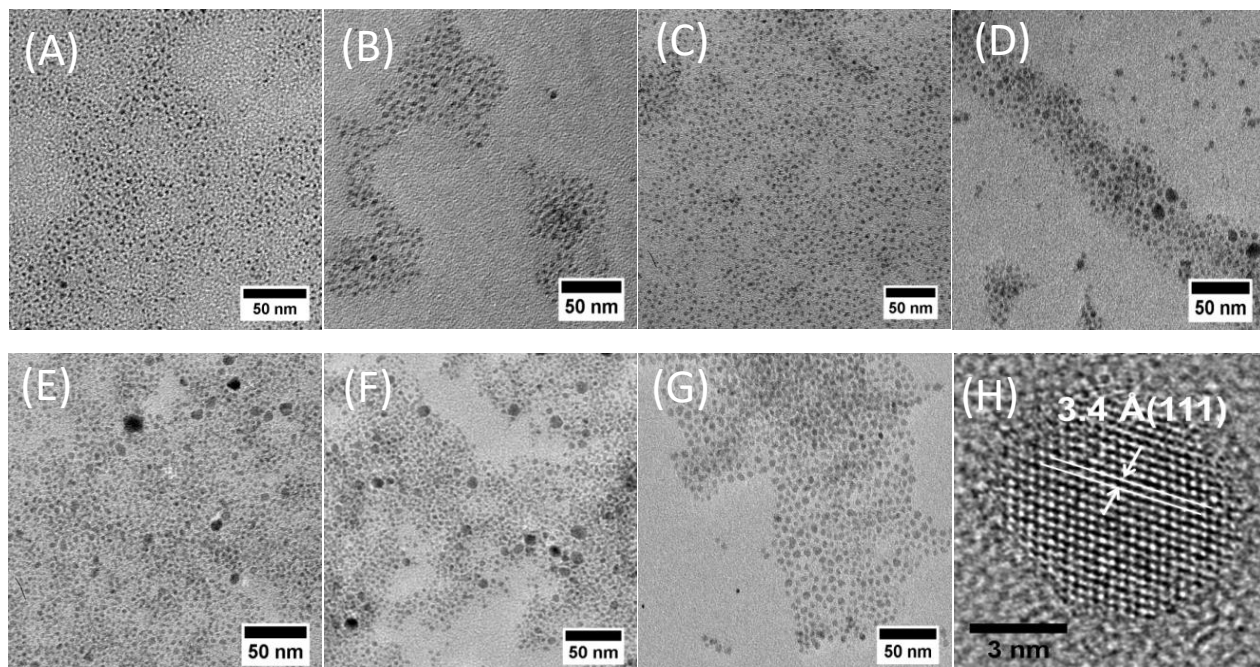
Figure 3.13. TEM Images of $Ge_{1-x}Sn_x$ NCs with Sn composition ranging from (A) x=0.000, (B) x=0.033, (C) x=0.056, (D) x=0.077, (E) x=0.088, (F) x=0.092, (G) x=0.116. (H) HRTEM of a single $Ge_{0.884}Sn_{0.116}$ NC showing the lattice fringe corresponds to (111) plane of cubic Ge.
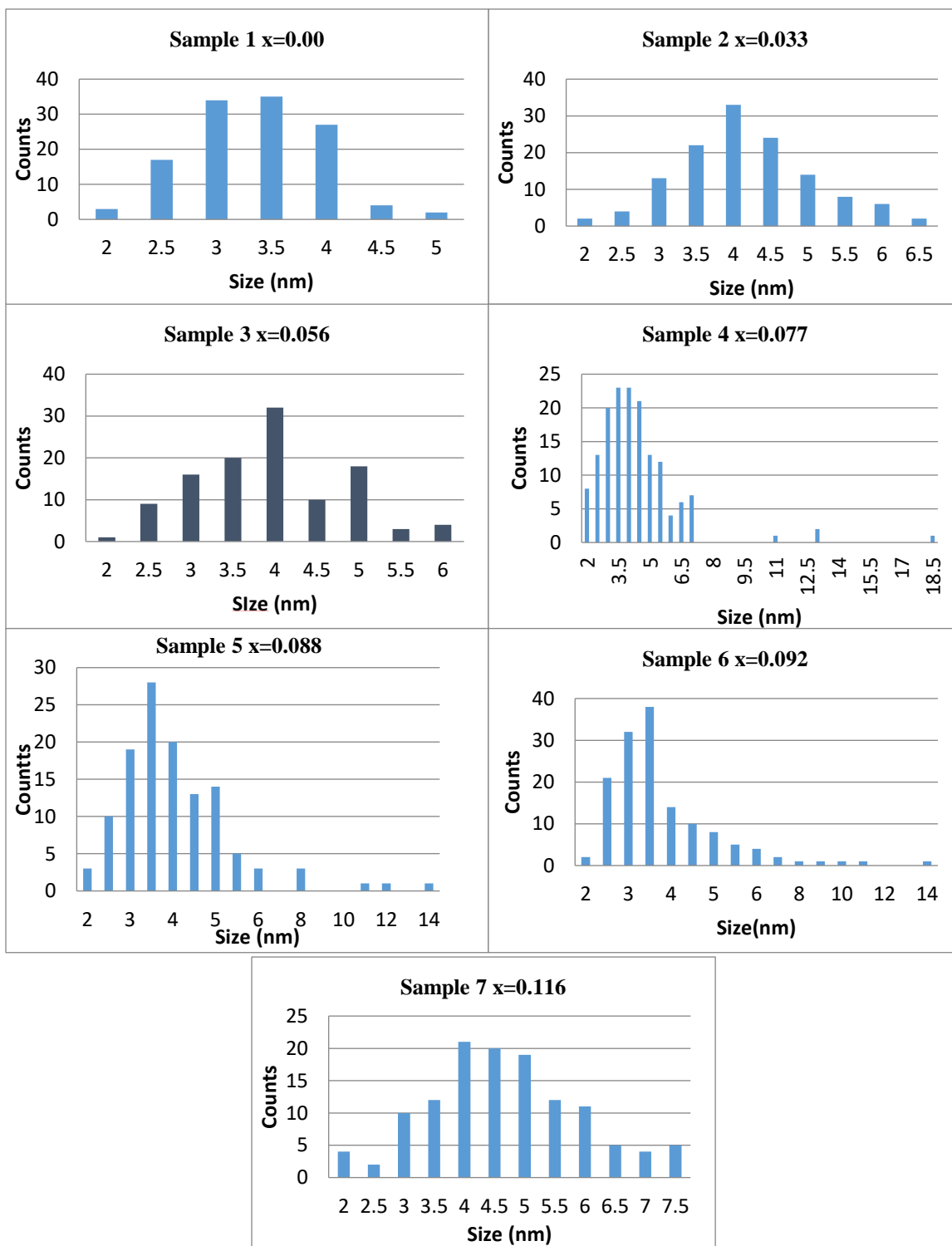
Figure 3.14. Size histograms of Ge$_{1-x}$Sn$_x$ alloy NCs with average size in the range of 3.4-4.3 nm obtained from analysis of 125-150 individual nanocrystals from multiple TEM images.

Solution based UV-Visible-near-IR (NIR) spectra indicate absorption onsets from 850-1100 nm with sharp increases in the visible range similar to single element Si and Ge NCs (Figure 3.15).[65, 109] To probe the effects of size and composition on optical bandgaps, solid state diffuse reflectance NIR spectroscopy was employed. The Kubelka-Munk (KM) remission function, which converts the reflectance to pseudo-absorption, is widely applied method for determining the bandgaps from reflectance data.[71, 72] For analysis of $Ge_{1-x}Sn_x$ nanoalloys, the reflectance data were converted to absorption using KM function[71, 72] and the bandgap measurements were made by extrapolating a least squares linear regression of the first major onset of the absorption profile to the intersection point of the baseline. Details about the extrapolation are provided more in-depth in Table 3.4. The energy gaps obtained from KM analysis indicate strong quantum size effects in $Ge_{1-x}Sn_x$ NC samples 1–7 (Figure 3.16) and a clear red shift with increasing Sn composition (Table 3.3). Since the alloy NCs produced by this route have nearly the same morphology and average particle size (4.1-4.6 nm), the systematic red shifts in their band energies can be correlated to the effect of Sn (bandgap = 0.09 eV)[42] concentration (x). It is significant to note that the bandgap values obtained from KM analysis (0.75-1.29 eV for x = 0.092-0.00) are significantly larger than those reported for $Ge_{1-x}Sn_x$ thin film alloys (0.35-0.80 eV for x= 0.15-0.00),[15] consistent with the size confinement effects. However, the KM analysis does not account for the type of transition occurring, which can lead to underestimated measurements.
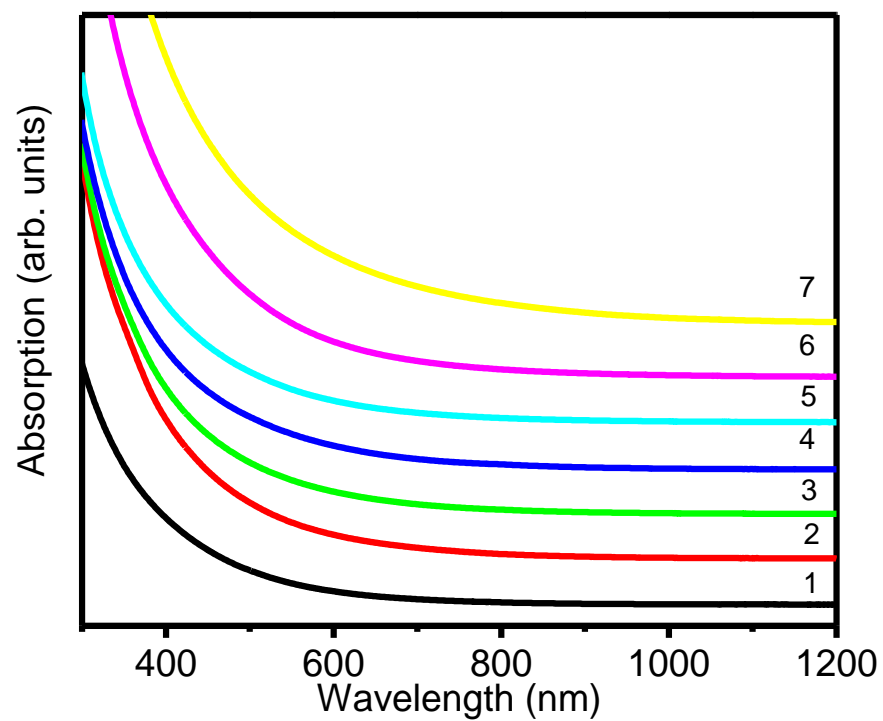
Figure 3.15. UV-visible-NIR spectra of 3.6-4.3 nm $Ge_{1-x}Sn_x$ alloy NCs examined in this study along with the Sn composition (1) x=0.000, (2) x=0.033, (3) x=0.056, (4) x=0.077, (5) x=0.088, (6) x=0.092, (7) x=0.116.

Table 3.4. Comparison of the elemental composition, primary particle sizes, and optical band gaps from $(h\nu\alpha)^2$, $(h\nu\alpha)^{1/2}$, corresponding to direct and indirect gap energies, respectively and R squared values for the linear regressions used to determine bandgap energies for 3.4-4.6 nm $Ge_{1-x}Sn_x$ NCs.

Sample	Sn composition ICP-OES (x)[a]	Particle Size (nm)[b]	$(h\nu\alpha)^2$ E_g (eV)[c]	R^2	$(h\nu\alpha)^{1/2}$ E_g (eV)[c]	R^2
1	0.000	3.4 ± 0.4	1.47	0.9969	1.31	0.9954
2	0.033 ± 0.007	4.1 ± 0.8	1.53	0.9877	1.23	0.9983
3	0.056 ± 0.002	4.0 ± 0.8	1.43	0.9985	1.20	0.9981
4	0.077 ± 0.008	4.3 ± 1.2	1.51	0.9901	1.59	0.9671
5	0.088 ± 0.012	4.1± 1.0	1.39	0.9921	1.39	0.9921
6	0.092 ± 0.014	4.3 ± 1.4	1.15	0.9975	1.15	0.9983
7	0.116 ± 0.017	4.6 ± 1.2	0.95[d]	0.9899	0.75[d]	0.9955

[a] Elemental compositions were obtained as mol % Sn from ICP-OES averaging 3 individual measurements per sample.

[b] Average particle size was calculated from counting 125-150 individual NCs from TEM images.

[c] Optical bandgaps were estimated by extrapolating the first major absorption event of the experimental data to the intersection point of the baseline. To reduce inconsistencies in the extrapolation least squares linear fits were employed on the experimental data. The points selected for fitting with the linear regression was typically covered a range of 0.4 electron volts. To obtain the best linear fits the experimental data range selected was allowed to vary from 0.3 electron volts to 0.6 electron volts. It is important to note multiple permutations of data ranges were analyzed for each sample. Only insignificant variations of bandgap values were observed regardless of the fitting range selected therefore only the fits with the best R^2 values were used to estimate the bandgap of the $Ge_{1-x}Sn_x$ NCs.

[d] Onset cut off by detector limitation.
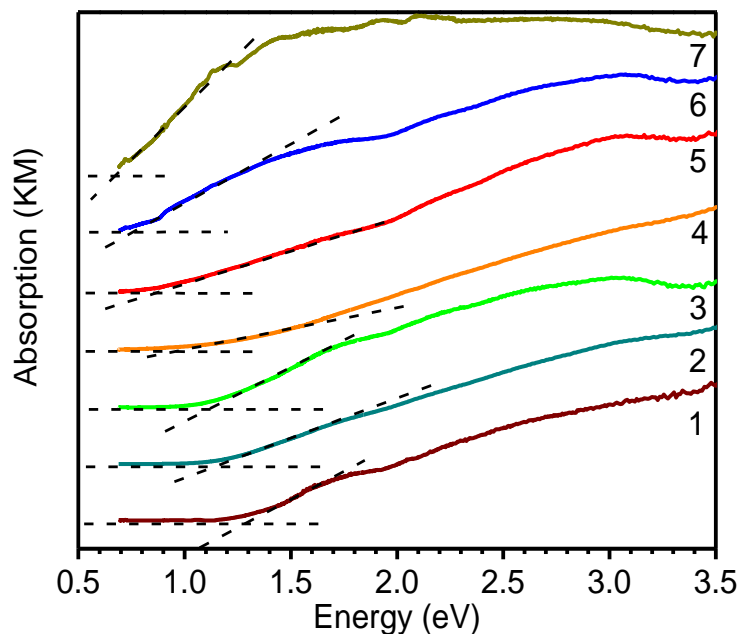
Figure 3.16. Diffuse reflectance spectra (converted to absorbance using Kubelka-Munk remission function) of 3.6-4.3 nm $Ge_{1-x}Sn_x$ alloy NCs as a function of Sn composition. (1) x=0.000, (2) x=0.033, (3) x=0.056, (4) x=0.077, (5) x=0.088, (6) x=0.092, and (7) x=0.116.

It is important to note that bulk Ge exhibits a fundamental indirect gap of 0.67 eV and a higher energy direct gap of 0.80 eV.[28] The addition of Sn into Ge has been shown to greatly reduce both energy gaps,[14, 15, 23, 24, 27, 28, 87] however currently there are no studies that show the effects of quantum confinement on indirect and direct band energies. Hence, to account for different electronic transitions, the Tauc equations for both indirect and direct bandgaps were utilized for comparision.[64, 72, 73, 108, 110-113] Tauc equation states that the absorption coefficient (α) of a semiconductor is proportional to the density of states for a given transition $(hv - E_g)^{1/n}$ where n = 2, 2/3, ½, 1/3 corresponds to the inter-band transitions of an allowed direct gap, forbidden direct gap, allowed indirect gap, and forbidden indirect gap, respectively.[72] Consistent with literature studies, we have utilized

the assumption that the product of KM conversion $\propto \alpha$[71, 72] allowing for the reflectance data to be employed in the Tauc analysis (Equation 1),[73] where α is the absorption coefficient, hv is the photon energy, E_g is the bandgap and A is the proportionality constant.

$$\alpha(hv)^n = A(hv - E_g) \tag{1}$$

The direct and indirect bandgaps of $Ge_{1-x}Sn_x$ alloy NCs were obtained by plotting $(\alpha hv)^n$ verses hv obtained from corresponding Tauc equations.[9, 72, 73, 108, 110-112] Bandgap energies were determined by extrapolating from least squares linear regressions of the first major absorption onset of $(\alpha hv)^n$ to the intersection point of the baseline (Figure 3.17, Table 3.4 and Table 3.3) as reported in the literature. Details about the regression fits are provided more in-depth in Table 3.4. Tauc analysis suggests indirect bandgaps in the range of 1.31-0.75 eV and direct bandgaps in the range 1.47-0.95 eV for as-prepared nanoalloys with x = 0.000-0.116 (Table 3.3). Slight differences are seen between the three methods of bandgap determination. While all three are consistent in demonstrating an overall decrease energy with increasing Sn composition is observed (Figure 3.18 & 3.19 Table 3.5). However, both indirect and direct gap methods indicate slight various possibly due to changes in the band structure or quantum confinement. As previously discussed, it has been predicted that $Ge_{1-x}Sn_x$ thin film alloys exhibit an indirect to direct transition from 6.3-11% Sn[17, 23-26, 30, 31, 36] which has been experimentally observed for x = 7.1-8.6%.[23-25] It is likely that $Ge_{1-x}Sn_x$ NCs follow a similar trend, nonetheless further experimental and theoretical studies including steady state and ultrafast absorption and emission spectroscopy analyses, which are beyond the score of current work are needed

to conclusively confirm this transition. Specific studies to probe the evolution of band structure as a function of Sn composition are currently underway.
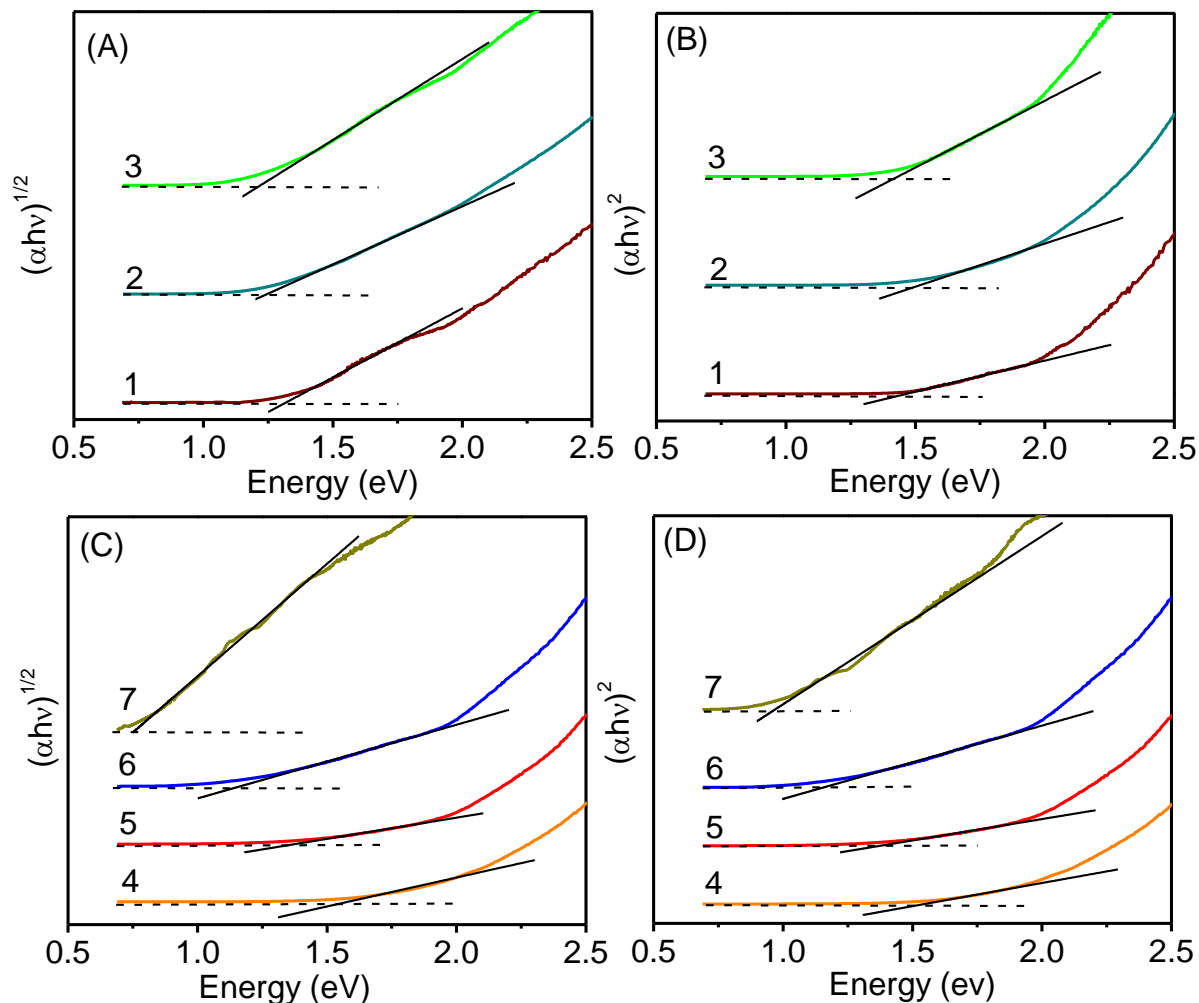
Figure 3.17 Tauc plots of Ge$_{1-x}$Sn$_x$ alloy NCs. (A) sample 1-3 plotted with indirect-gap Tauc function, (B) sample 1-3 plotted with direct-gap Tauc function, (C) sample 4-7 plotted with indirect-gap Tauc function and (D) sample 4-7 plotted with direct-gap Tauc function. Solid line represents linear regressions; dashed lines are baselines. The average Sn compositions obtained from ICP-OES analysis are (1) x=0.000, (2) x=0.033, (3) x=0.056, (4) x=0.077, (5) x=0.088, (6) x=0.092, and (7) x=0.116.
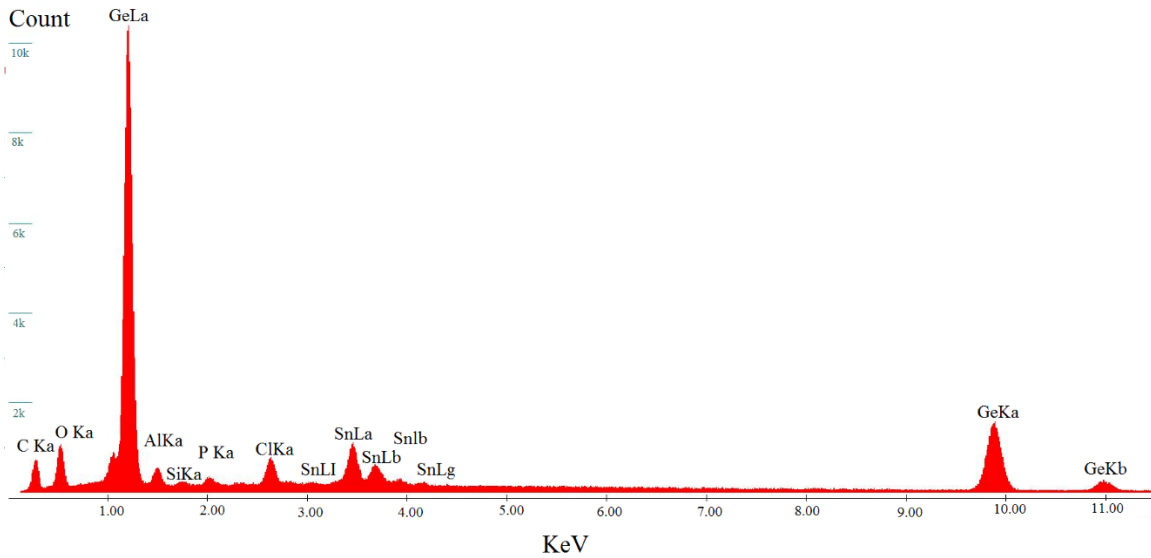
Figure 3.18. Representative EDS spectrum of Ge$_{1-x}$Sn$_x$ NCs. C, O, and Al signals are originating from the carbon tape and aluminum sample holder. Si and P suspected impurities due to the use of molecular sieves for solvent drying.
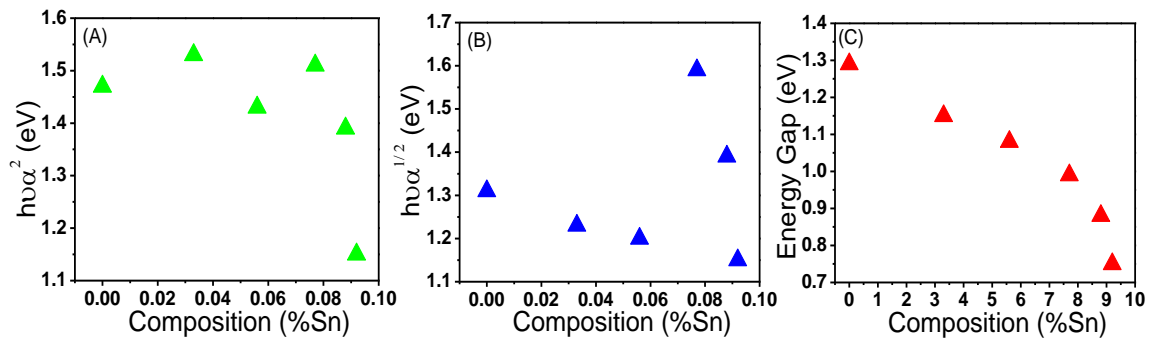
Figure 3.19 Bandgap values obtained from three different functions A) Direct gaps from (hvα)^2 B) Indirect gaps from (hvα)$^{\frac{1}{2}}$ C) Energy gaps obtained from the Kubelka-Munk function.

Table 3.5 Atomic %Sn values obtained from 5 points per sample in SEM/EDS for 3.6-4.3 nm $Ge_{1-x}Sn_x$ alloy NCs.

Sample	Sn atomic %					Average %
2	2.91	2.98	3.21	2.67	3.13	2.98
3	4.61	4.30	4.02	4.52	4.37	4.36
4	6.62	6.83	5.87	6.53	6.38	6.44
5	6.56	6.72	8.10	6.91	7.97	7.25
6	8.96	8.93	8.96	9.24	8.63	8.94
7	10.86	10.79	10.92	10.89	11.2	10.93

3.4   Conclusions

We have successfully produced two different size sets of homogeneous $Ge_{1-x}Sn_x$ alloy NCs displaying Sn composition in the range of x = 0.000–0.279 using a low temperature colloidal synthesis. The larger set of NCs (15–23 nm) provides an accurate measure of the structural characteristics as a function of Sn composition and suggests a high solubility of Sn in nanocrystalline cubic Ge for OLA passivated particles. The successful incorporation of Sn into Ge has been confirmed with PXRD, STEM-EDS, and Raman spectroscopic studies and the increase in the inter-planar distance was further confirmed through HRTEM studies. Thermal stability has been examined in samples exposed to air as well as kept in rigorous inert conditions. $Ge_{1-x}Sn_x$ NCs demonstrate moderate resistance against phase segregation even at elevated temperatures (400–500 °C) without any surface capping layer. While many studies have been done on the contraction

of the band energies in $Ge_{1-x}Sn_x$ alloy films,[14, 15, 27, 28] to our knowledge this study communicates the first report on the dependence of bandgaps of colloidal $Ge_{1-x}Sn_x$ NCs as a function of size and Sn composition. The larger $Ge_{1-x}Sn_x$ crystallites (15–23 nm) exhibit band energies far below that of bulk Ge indicating lack of significant size confinement. In contrast, strong quantum size effects were observed for smaller $Ge_{1-x}Sn_x$ nanoalloys (3.4–4.6 nm) resulting in a wide range of direct and indirect band energies throughout much of the NIR spectrum. Despite the red shift induced via incorporation of Sn the fundamental energy gaps of $Ge_{1-x}Sn_x$ nanoalloys were well above than those of the non-confined bulk counterparts (0.35 - 0.80 eV),[13] consistent with the quantum size effects.

Further optimization in size and dispersity control over variable Sn concentrations are being performed. The effort in the future will be focused on elucidating the luminescent properties of $Ge_{1-x}Sn_x$ NCs and achieving a better insight into the growth kinetics of nanoalloys as a function of Sn composition. As more and more efforts are put into the study of new semiconducting systems in order to produce high quality materials that are both stable and have low to no toxicity, $Ge_{1-x}Sn_x$ alloys have great potential as both a narrow direct gap thin film material and now as quantum dots with composition tunable bandgaps. We have demonstrated the successful synthesis of $Ge_{1-x}Sn_x$ NCs free of segregated Sn at concentrations far exceeding the previous two reports,[51, 61] with strong optical absorption and high thermal stability. The colloidal synthesis developed here allows for the low-cost solution based processing for thin film fabrication, which is more cost effective than previously reported molecular beam epitaxy and chemical vapor deposition methods.

CHAPTER 4

Ultra-small Ge$_{1-x}$Sn$_x$ Quantum Dots with Visible

Photoluminescence

4.1   Introduction

Development of direct bandgap materials from low-to-nontoxic, earth-abundant Group IV elements, has been a long-term goal in semiconductor research. Ge$_{1-x}$Sn$_x$ alloys have been demonstrated as prime candidates to fill this position. Alloying with Sn allows energy gap tuning and improves light-matter interactions, which otherwise are weak in the case of indirect bandgap Si and Ge. When the Sn composition in Ge$_{1-x}$Sn$_x$ thin films exceeds x = 0.06-0.20 (depending on strain), the material is expected to be a direct bandgap semiconductor.[14, 15, 22-24] However, the amount of Sn required for the indirect to direct bandgap transition, also reduces the gap energies deep into the infrared region (0.35-0.80 eV for x = 0.15-0.00).[14, 15, 28] To extend the spectral range into visible and near infrared spectrum and improve the efficiency of the optical transitions, there has been increased interest in producing Ge$_{1-x}$Sn$_x$ nanostructures to exploit quantum confinement effects.[65] High-quality Ge$_{1-x}$Sn$_x$ nanowires have been previously reported,[58, 60] however the larger nanowires did not exhibit size confinement effects due to smaller excitonic Bohr radius of Ge (11.5 nm).[114] In contrast, there have been two reports on the synthesis of Ge$_{1-x}$Sn$_x$ NCs, reporting energy gaps from weakly confined (1.04-0.41 eV)[63] and somewhat strongly confined (1.29-0.75 eV)[59] regimes. In both reports, the incorporation of Sn has been shown to significantly redshift the energy gaps when the particle size is held   constant,   consistent   with   alloying   effects.   However,   comprehensive

photoluminescence (PL) studies on $Ge_{1-x}Sn_x$ quantum dots (QDs) are still lacking, in part due to the low success of synthesizing phase pure, luminescent QDs combined with the fairly low quantum yields achieved.[40]

In this study, we have explicitly focused on $Ge_{1-x}Sn_x$ QDs that are smaller than 3.0 nm to elucidate the full potential of quantum confinement effects. The resultant ultra-small QDs exhibit energy gaps in the visible spectrum with composition dependent photophysical properties. The structure and morphology of the QDs were examined with powder X-ray diffraction (PXRD) and transmission electron microscopy (TEM). The structural analysis indicates a diamond cubic structure as expected for $Ge_{1-x}Sn_x$ NCs and thin film alloys.[58] Solid-state absorption and emission studies indicate strong confinement effects with absorption onsets ranging from 1.55-2.16 eV and PL peak maxima from 1.72-2.05 eV (620-720 nm) for x = 0.018-0.236. *Ab initio* hybrid functional calculations revealed energy gaps in close agreement with the experimental results, confirming measured QD sizes and compositions.

4.2   Experimental Section

4.2.1 Materials.

Germanium diiodide (99.99+ %) and tin dichloride (>99.9985 % Ultra-Dry), were purchased from Strem Chemicals and Alfa Aesar, respectively and stored in a N_2 glove box. N-butyllithium (BuLi) 1.6 M in hexane was purchased from Sigma Aldrich. Organic solvents such as, 1-octadecene (ODE, 90%), oleylamine (OLA, 80-90%), and Rhodamine 101 inner salt (99%) were purchased from Fisher Scientific. ACS grade solvents such as chloroform, toluene, carbon tetrachloride, and methanol were

purchased from Acros. OLA and ODE were dried by heating at 120 °C under vacuum for one hour prior to storage in a N_2 glovebox. Methanol was dried over molecular sieves and toluene was dried over Na and both were distilled prior to use. Carbon tetrachloride was degassed by bubbling N_2 through it and was stored under inert conditions. *(Caution: n-butyllithium is highly pyrophoric and must be handled in air free conditions by properly trained personal. Carbon tetrachloride is highly toxic and its use should be minimized to limit exposure.)*

4.2.2 Synthesis of Ultra-Small (1-3 nm) $Ge_{1-x}Sn_x$ Quantum Dots (QDs)

A wet-colloidal strategy was used to produce $Ge_{1-x}Sn_x$ QDs with a diameter of 1.5-2.2 nm and Sn compositions of x = 0.018, 0.046, 0.066, and 0.236. Details of the synthesis procedures have been discussed elsewhere,[59] with the major change in procedure being the varied concentration of the reducing agent. Briefly, the appropriate molar ratios of GeI_2 and $SnCl_2$ (0.6 mmol total) and 20 mL of oleylamine were loaded into a three neck round bottom flask under air-free conditions. This mixture was stirred and degassed for ~8 min while heating to 115 °C then heated to 230 °C (~10 °C/min) prior to injection of the reducing agent. The reducing agent used was n-butyllithium (BuLi) diluted in 3 mL of 1-octadecene and the amount of BuLi used varied from 0.5-0.9 equivalents of the precursor halide concentration. After injection, the temperature was ramped to 300 °C at a rate of ~6 °C/ min, before being cooled by compressed air (~5 min). Resultant QDs were isolated by a mixture of toluene ~5−10 mL followed by methanol ~60−90 mL, and purified by dispersing in toluene and precipitating with methanol twice.

94

4.2.3 Synthesis of Larger, Polydisperse (5-20 nm) $Ge_{1-x}Sn_x$ QDs

A set of larger, polydisperse $Ge_{1-x}Sn_x$ QDs (5-20 nm) were produced for STEM/EDS analysis, using a synthetic procedure reported in the literature.[59] Briefly, 0.6 mmol of metal halides, GeI_2 /$SnCl_2$, were heated in OLA at 115 °C to produce a homogeneous orange color solution. This mixture was heated to 230 °C and BuLi (1.1 molar eq. of halides) in ODE (3.0 mL) was swiftly injected. Then the reaction was heated to 300 °C and the growth stage was extended to 10 min at 300 °C to produce larger polydisperse (5-20 nm) alloy NCs. This ensures a similar nucleation process for both ultra –small and larger, polydisperse $Ge_{1-x}Sn_x$ NCs.

4.2.4 Isolation and Purification of QDs

After the desired growth time, the temperature was dropped below 100 °C and the crude reaction mixture was mixed with 10 mL of freshly distilled toluene. Then, 60-90 mL of freshly distilled methanol was added, the resultant mixture was centrifuged for 5 min to obtain an orange color powder. The supernatant was discarded and the precipitate was twice purified by dispersing in toluene and subsequent precipitation with methanol.

4.2.5 Characterization of QDs

Powder X-ray diffraction (PXRD) measurements were performed with a PANanalytical X'Pert PRO X-Ray diffractometer calibrated with Si standard and equipped with a Cu Kα anode (κα= 1.54 Å). Purified QDs were deposited on to a low background sample holder and diffraction patterns were collected at 45 kV and 40 mA operating conditions. A Cary 6000i spectrophotometer (Agilent Technologies) was used for solution absorption

measurements and solid state diffuse reflectance (DRA) with an internal DRA 2500 attachment. Solid sample measurements were performed by mixing the dry QDs in a $BaSO_4$ matrix prior to analysis. Elemental compositions were recorded by energy dispersive spectroscopy (EDS). EDS data were obtained in a Hitachi FE-SEM Su-70 scanning electron microscope (SEM) operating at 20 KeV with an in-situ EDAX detector. Dried QDs were adhered to an aluminum stub with double sided carbon tape prior to analysis. The elemental compositions were determined by averaging the atomic percentages of Ge and Sn acquired from 5 individual spots per sample. X-ray photoelectron spectroscopy (XPS) analyses were performed with a Thermofisher ESCALAB 250 equipped with Al κα source. Samples were prepared by pressing them into indium foil (Sigma Aldrich) which was adhered to an aluminum stub with conductive carbon tape. Low resolution transmission electron micrographs (TEM) were recorded using a Zeiss Libra 120 microscope operating at an accelerating voltage of 120 kV. High resolution TEM (HRTEM) analyses were performed on a JEOL 2000FX scanning transmission electron microscope with LaB_6 source operating at 200 kV. Scanning transmission electron microscopy (STEM) and HRTEM images were recorded on a FEI Titan 8300 microscope equipped with a Gatan 794 multiscan camera operating at 200 kV. TEM samples were prepared by drop casting ~5 μL of NCs, dispersed in CCl_4, onto a carbon coated copper grids and evaporating the solvent. Photoluminescence (PL) studies were performed using a frequency doubled Ti:sapphire laser (385 nm wavelength, 150 fs pulse width, 160 kHz to 80 MHz repetition rate) as the excitation source. The detector was a liquid N_2 cooled charge coupled device (CCD) camera connected to a spectrometer. Samples were drop cast onto a clean Si substrate and dried and stored

96

under nitrogen. Quantum yield measurements were performed on a Cary Eclipse fluorescence spectrophotometer (Agilent Technologies). Rhodamine 101 and $Ge_{x-1}Sn_x$ QDs were dissolved in $CHCl_3$ and the concentrations were adjusted so that the optical densities were matched at the respective excitation energies. Annealing studies were performed in a quartz tube under high purity argon flow, in a Thermo-Scientific Lindenburg Blue M furnace. Raman spectra were acquired using a Horiba LABram HR Evolution Confocal Raman Spectrometer equipped with a 532 nm laser with powder samples deposited on an aluminum substrate.

4.2.6 Theoretical Electronic Structure Calculations of QDs

Calculations were performed for $Ge_{1-x}Sn_x$ QDs with diameters of 2.1 nm and 2.7 nm, with dangling bonds passivated by hydrogen. Since hybrid functional structure relaxations are computationally demanding (and likely in this case unnecessary), lattice relaxations were performed using the generalized gradient approximation (GGA)[115] to the density functional theory, with forces minimized to 0.05 eV/Å or less. The electronic structure was calculated using tuned Heyd-Scuseria-Ernzerhof (HSE) hybrid functional calculations and the projector-augmented wave (PAW)[116] formalism, as implemented in VASP,[117] a plane-wave density functional code. In HSE hybrid functional, the semi-local Purdue-Burke-Ernzerhof exchange correlation part of the density functional is mixed with a Fock-type exchange in varying proportions at short range. In our calculations, the fraction of exact exchange was kept at a standard 25%, while the exchange range separation parameter was increased to 0.29 Å^{-1}, corresponding to the exchange screening length of 6.9 Å. The plane-wave basis sets with an energy cut-off of 250 eV were used. These parameters were found to reproduce bulk band structure of Ge in

excellent agreement with experiment and as such, are expected to be consistent for $Ge_{1-x}Sn_x$ alloy QDs. Test calculations performed for pure Ge QDs compared with previously published results obtained using empirical pseudopotential calculations show that the bandgaps of QDs are accurately reproduced. Excitonic effects were calculated using time-dependent hybrid functional (TD-HSE) calculations.

4.3 Results and Discussion

4.3.1 Physical Charaterization of Ultra-small GeSn Quantum Dots

The growth of $Ge_{1-x}Sn_x$ alloys is very challenging due to the lack of a stable bulk phase.[51, 59, 61, 63] In addition, with variation in Sn composition, the nucleation and growth kinetics have been shown to drastically change. These changes are a result of differences in the reaction chemistry and crystallization temperature of the alloy that is being produced.[59, 63] Optimizing the synthesis for any specific composition of QDs requires a multivariate approach, taking into consideration the precursor concentrations, solvent volume, amount of reducing agent, nucleation and growth temperature and growth time. The synthesis of ultra-small $Ge_{1-x}Sn_x$ QDs was carried out at 300 °C similar to a literature method with changes in the reduction event,[13] as detailed above. Moreover, a larger polydispsere set of $Ge_{1-x}Sn_x$ QDs (5-20 nm) were also produced when the growth time is extended to 10 min. at 300 °C. The ultra-small QDs with visible PL can be clearly distinguish by a reaction product of light orange to deep red color.

Powder X-ray diffraction patterns suggest that as-prepared QDs consist of ultra-small diamond cubic crystals with no detectable Sn impurities (Fig. 4.1A). As the concentration of Sn increases, a systematic shift of diffraction peaks to lower 2θ angles

98

is expected, relative to the diamond cubic phase of Ge.[51, 58, 59, 63] However, as the

crystallite size decreases, scattering signal increases and peak broadening dominates
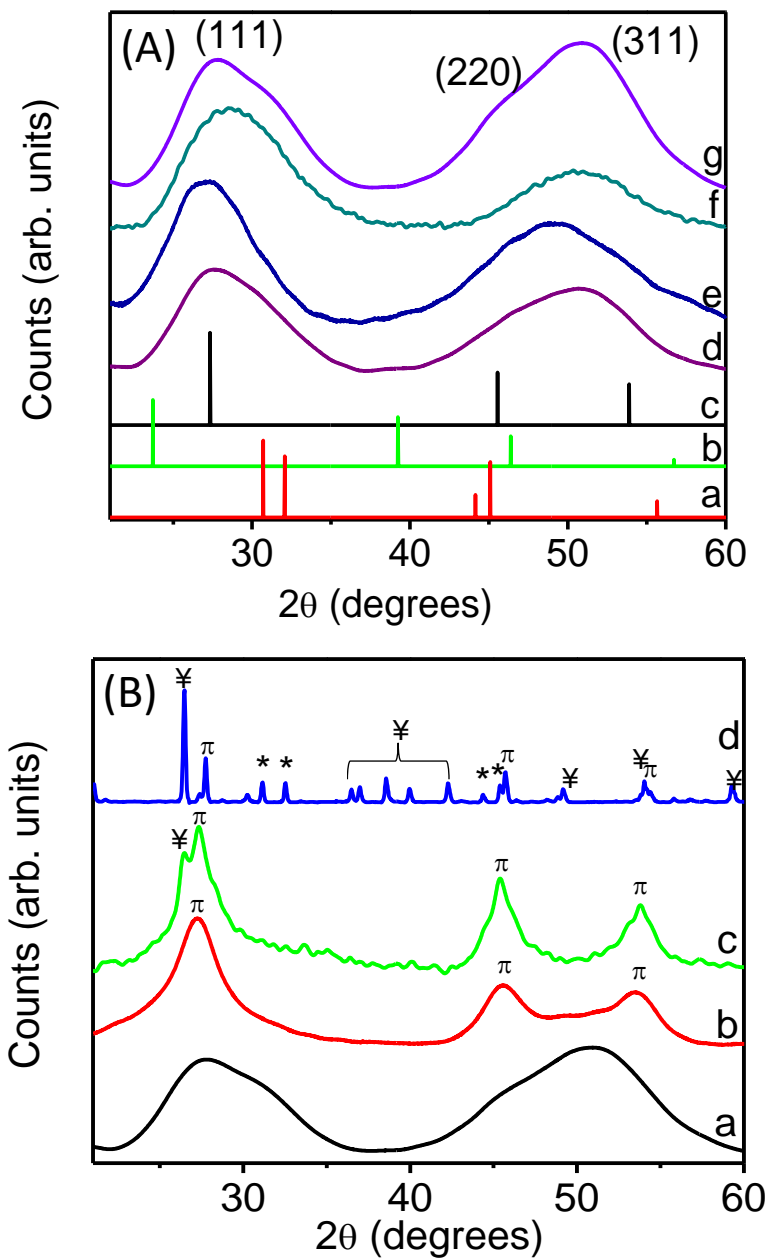
Figure 4.1. (A) PXRD patterns of $Ge_{1-x}Sn_x$ QDs a) *=β-Sn, JCPDS # 00-004-0673(b) α-

Sn, JCPDS # 01-086-2266 (c) π=Ge, JCPDS # 01-089-5011 x = (d) 0.018, (e) 0.046, (f)

0.066, and (g) 0.236. (B) Annealing study performed on $Ge_{0.764}Sn_{0.0236}$. a) as-prepared QDs b) 400 C° c) 500 C° d) 600 C° for 11 hours. ¥ =GeO_2, JCPDS # 00-036-1463

much of the diffraction pattern. The broad peaks obscure the expected shift from cubic Ge Bragg reflections making it difficult to quantify the effects of Sn on lattice expansion. Such extreme line broadening also causes the peaks corresponding to (220) and (311) to merge. This is because the combined scattering from each plane is more intense than the diffraction from the individual Bragg angles. In addition, the incorporation of Sn can lead to alloy disordering and strain in the lattice, contributing even more to broadening of Bragg reflections.[118]

To further elucidate the structure and thermal stability, samples were annealed in a tube furnace for 11 h at 400, 500 and 600 °C (Figure 4.1B). After sintering, the diamond cubic structure became evident with progressive crystal growth at higher temperatures. Between each annealing step, samples were exposed to ambient conditions for PXRD, resulting in the formation of GeO_2 at 500 °C. Further heating to 600 °C resulted in complete sintering, oxidation and segregation of the $Ge_{1-x}Sn_x$ QDs into GeO_2, tetragonal Sn, and cubic Ge phases. The lack of segregation below 500 °C suggests significant thermal stability of $Ge_{1-x}Sn_x$ QDs consistent with prior reports.[59, 63] Prior to annealing, X-ray photoelectron spectroscopy (Figure 4.2 and Table 4.1) was employed to study the oxidation states of Ge and Sn, which suggests that Sn is incorporated before annealing and not after.
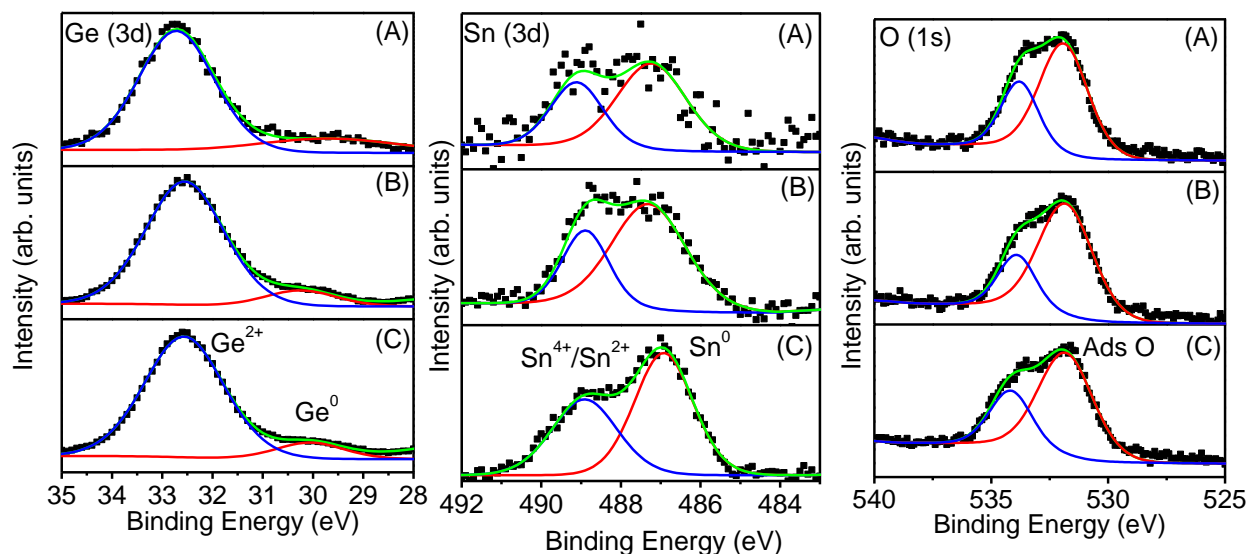
Figure 4.2. Representative X-ray photoelectron spectra of ultra-small $Ge_{1-x}Sn_x$ QDs: (A) x = 0. 018, (B) x = 0.046, (C) x = 0.066. Dotted lines represent spectral data and solid blue and red lines are fitted deconvolutions and green line is the sum of the fitted peaks.

The XPS spectra of ultra-small $Ge_{1-x}Sn_x$ QDs are consistent with previous reports.[59, 63] The peaks observed in the Ge (3d) spectra at 30.0 eV and 32.5 eV can be assigned to Ge^0 and Ge^{2+}, respectively (Figure 4.2). There is a noted absence of Ge^{4+} which would indicate GeO_2.[59, 63, 119] The relative intensity of the two peaks suggests a large contribution from the surface of the QDs as is expected for ultra-small QDs with a large surface to volume ratio. Examination of the Sn (3d) region indicates a similar story, with both core Sn^0 (486.9 eV) and surface $Sn^{4+/2+}$ (488.8) present in the sample (Figure 4.2).[59,63, 119] The Sn peaks are shifted to higher energies due to surface charging effect commonly observed in XPS analysis of nanoparticles.[59, 104] In combination with XRD, Raman, and STEM/ EDS maps, the presence of Sn^0 confirms that $SnCl_2$ was successfully reduced and incorporated into the as-prepared $Ge_{1-x}Sn_x$ QDs with no surface segregation. Both

the $Sn^{4+/2+}$ and Ge^{2+} peaks are attributed to surface atoms bound to stabilizing ligands, similar to a previous report.[59] The potential presence of SnO_2 is ruled out by a lack of a O (1s) peak at 530.6 eV.[119] The O (1s) peaks observed at 531.9 and 534.1 eV are attributed to adsorbed H_2O and CO_2 from the atmosphere.

Table 4.2. Elemental composition of ultra-small $Ge_{1-x}Sn_x$ QDs acquired from energy dispersive spectroscopy (EDS) and X-ray photoelectron spectroscopy (XPS) analyses.

Sample	Sn composition from EDS[a]	Sn composition XPS[b]
$Ge_{1-x}Sn_x$	0.018 ± 0.07	0.0184
$Ge_{1-x}Sn_x$	0.046 ± 1.2	0.0479
$Ge_{1-x}Sn_x$	0.066 ± 0.5	0.075
$Ge_{1-x}Sn_x$	0.236 ± 1.4	N/A

[a]Sn compositions were obtained in terms of atomic % from SEM/EDS, and averaging five individual measurements per each sample. [b]Sn compositions were obtained from the ratio of Ge(3d) and Sn(3d) in XPS calculated with atomic sensitivity factors of 0.38 and 4.30, respectively.[119]

In addition, Raman spectroscopy was employed to study the vibrational energies of ultra-small QDs. The Raman shift for Ge-Ge bonds arises at 300 cm^{-1} and as the Sn concentration is increased a systematic redshift is expected.[23, 59] This is a result of the longer Ge-Sn bonds and the heavier Sn atoms. However, the bond vibrations in Ge also redshift with decreasing particle size in QDs due to phonon confinement.[100] As such, it is not possible for Raman to distinguish the amount of Sn in $Ge_{1-x}Sn_x$ QDs.

Nonetheless, Ge-Sn phonon modes are observed at ~276 cm^{-1} (Figure 4.3), consistent with previous reports on confined Ge and Ge$_{1-x}$Sn$_x$ nanostructures.[59, 120]
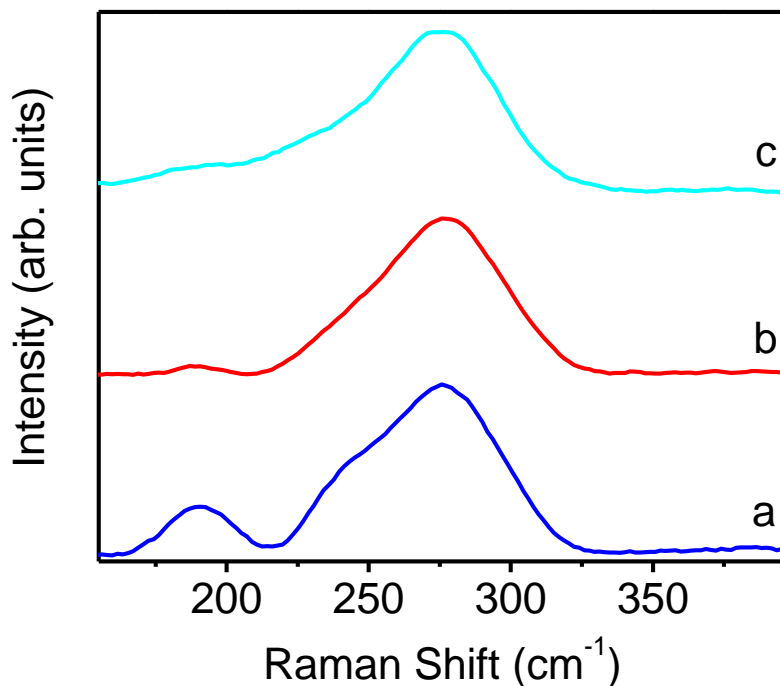
Figure 4.3. Raman spectra of ultra-small Ge$_{1-x}$Sn$_x$ QDs (1.85 ± 0.47 - 2.28 ± 0.48 nm) with varying Sn composition: x = (a) 0.018, (b) 0.066, and (c) 0.236.

To further investigate the crystal structure and size of the QDs, TEM was employed (Figure 4.4 and Figure 4.5). The bright field TEM images show particles with sizes ranging from 1.85 ± 0.47 - 2.28 ± 0.48 nm for x = 0.018 to x = 0.236. All four compositions of Ge$_{1-x}$Sn$_x$ QDs exhibit spherical morphology and fairly narrow dispersity given the significantly small size. Increasing Sn content has been shown to drastically change the nucleation and growth dynamics of Ge$_{1-x}$Sn$_x$ QDs, which makes the synthetic control challenging.[59, 63] Nonetheless, particle size histograms of as-

synthesized QDs (Figure 4.5) indicate there are narrow size discrepancies within samples and between QDs with varying Sn concentrations. A few larger QDs (3.0-4.5 nm) are present in the x = 0.046 and x = 0.236 samples, however, their effect on the optical properties would be minimal due to the low population count.
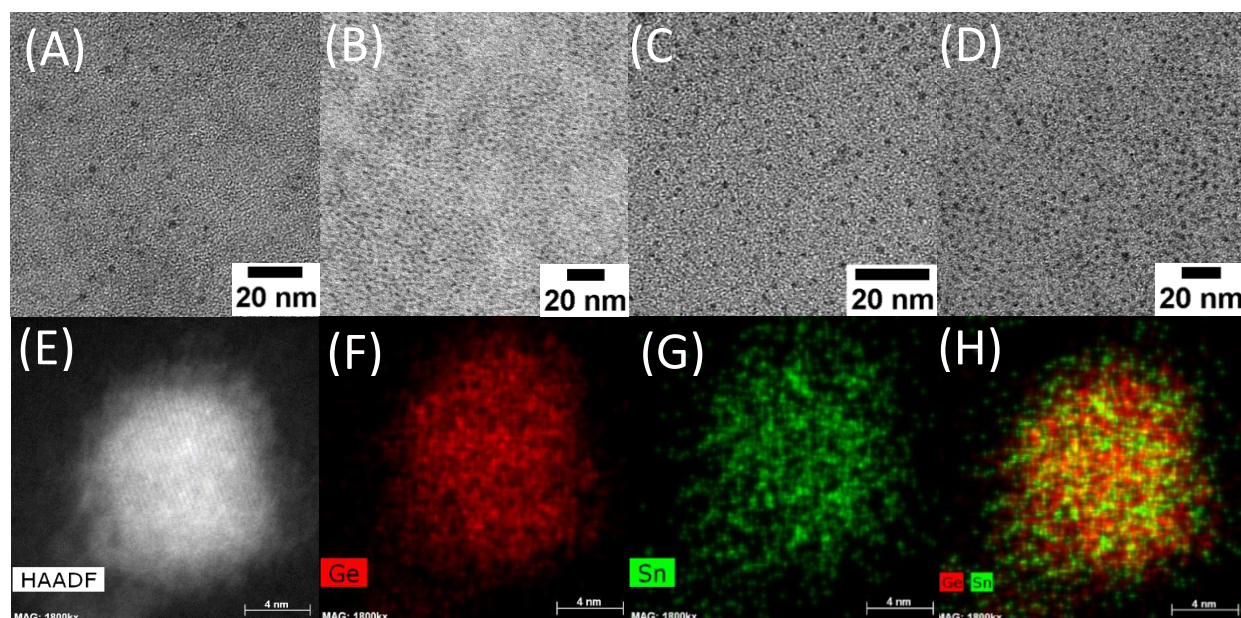
Figure 4.4. Low resolution TEM images of $Ge_{1-x}Sn_x$ QDs with varying Sn composition and almost consistent sizes: (A) x = 0.018, 2.28 ± 0.48 nm (B) x = 0.046, 1.76 ± 0.63 nm (C) x = 0.066, 1.85 ± 0.47 nm (D) x = 0.236, 2.01 ± 0.57 nm. (E) High resolution TEM image of a larger $Ge_{0.87}Sn_{0.13}$ QD along with STEM/EDS elemental maps of (F) Ge, (G) Sn, and (H) an overlay of Ge and Sn indicating the homogeneous distribution of elemental components throughout the QD.
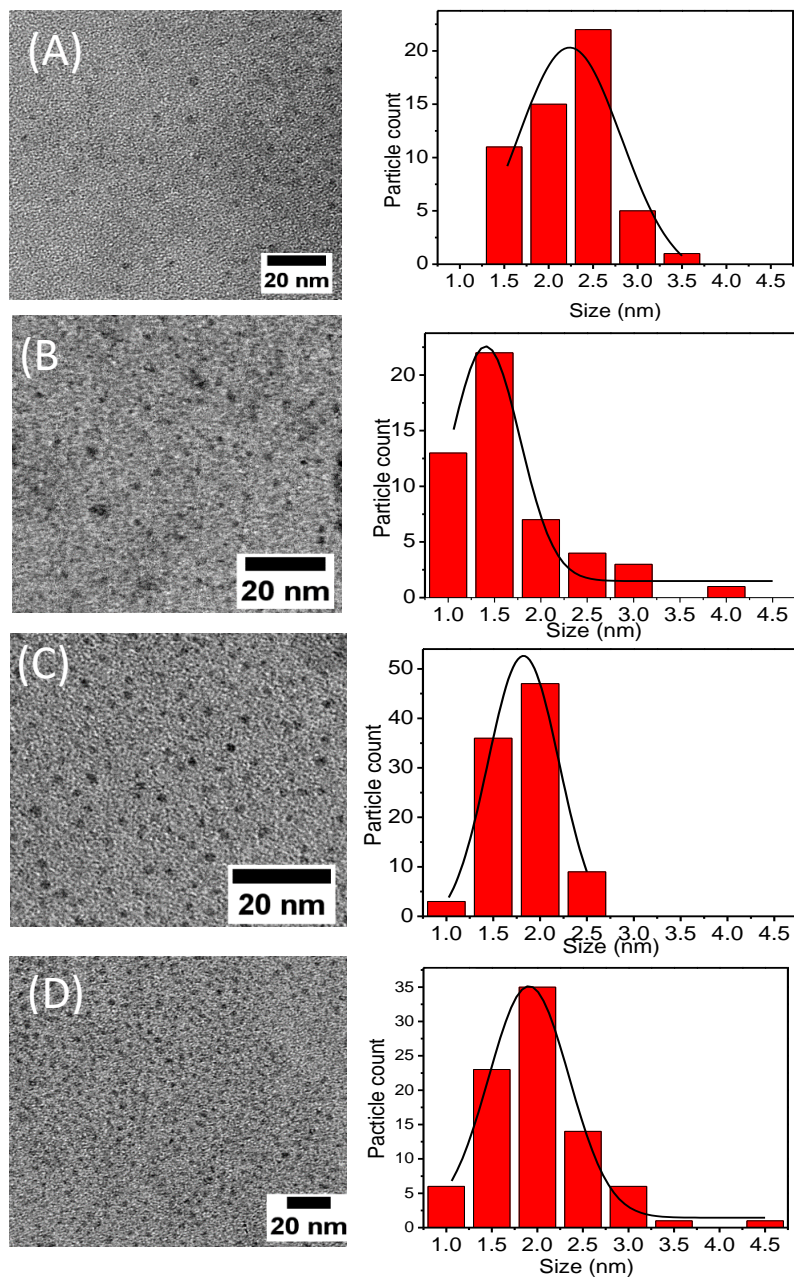
Figure 4.5 Bright field TEM images of ultra-small $Ge_{1-x}Sn_x$ QDs with varying Sn composition: (A) x = 0. 018, (B) x = 0.046, (C) x = 0.066, and (D) x = 0.236. The corresponding size histograms of $Ge_{1-x}Sn_x$ QDs without any post-synthetic size selection are also shown.

In conjunction with the PXRD and Raman spectroscopy, high-resolution TEM has been employed to elucidate the structure of $Ge_{1-x}Sn_x$ QDs. Figure 4.6 and 4.7 hows discrete QDs oriented with visible lattice spacings of 3.4, 2.1, 1.8 Å, considerably expanded from those of the (111), (220), (311) planes of diamond cubic Ge: 3.3, 2.0, 1.7 Å, respectively. The systematic lattice expansion of $Ge_{1-x}Sn_x$ with increasing Sn content is well documented and has previously been utilized to quantify the alloy composition in both thin films and QDs.[51, 63, 121] Scanning transmission electron microscopy (STEM) was utilized to acquire elemental maps of $Ge_{1-x}Sn_x$ QDs. For this analysis, a larger set of particles were produced (~5-20 nm), by a similar synthetic strategy,[13] due to difficulties in mapping ultra-small QDs. Elemental maps of Ge and Sn indicate even distributions of both components throughout the alloy lattice (Figure 4.4 and Figures 4.8-4.9). Therefore, combined with the HRTEM, these results suggest that the as-prepared $Ge_{1-x}Sn_x$ QDs are homogeneous solid solutions and devoid of segregated Sn species.
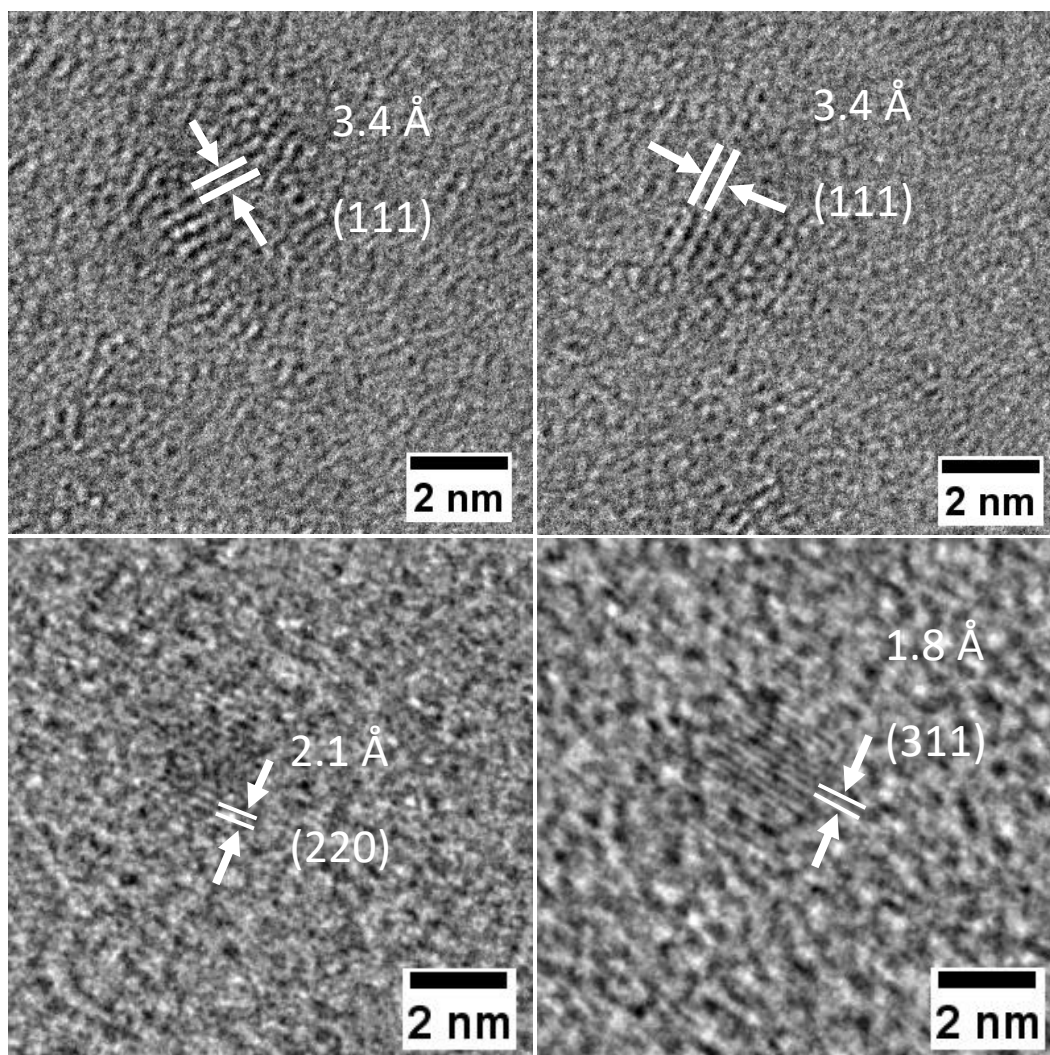
Figure 4.6. High resolution TEM images of 2.0 ± 0.57 nm $Ge_{0.764}Sn_{0.236}$ QDs. Visible lattice fringes are measured at 3.4, 2.1, and 1.8 Å corresponds to expanded (111), (220), and (311) planes of diamond cubic $Ge_{1-x}Sn_x$.
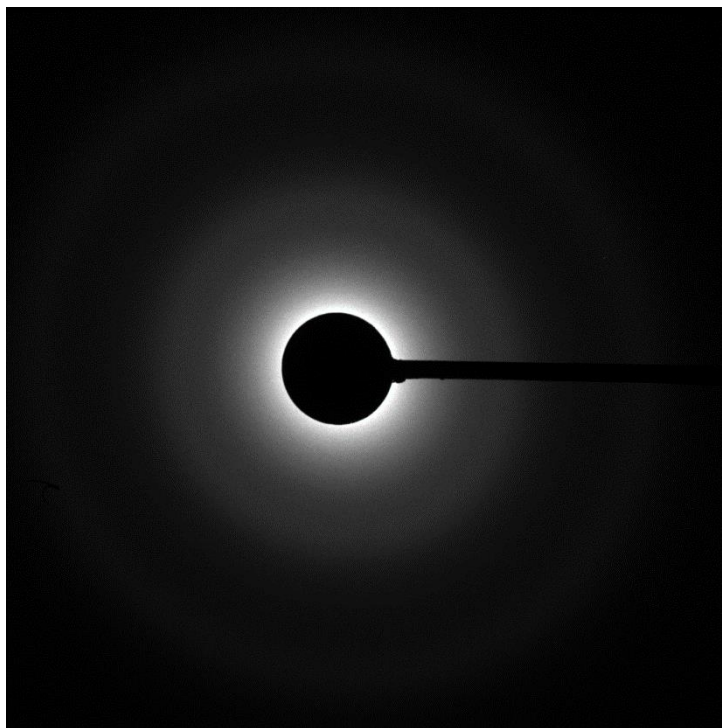
Figure 4.7. Representative electron diffraction pattern of ultra-small $Ge_{0.934}Sn_{0.066}$ QDs.
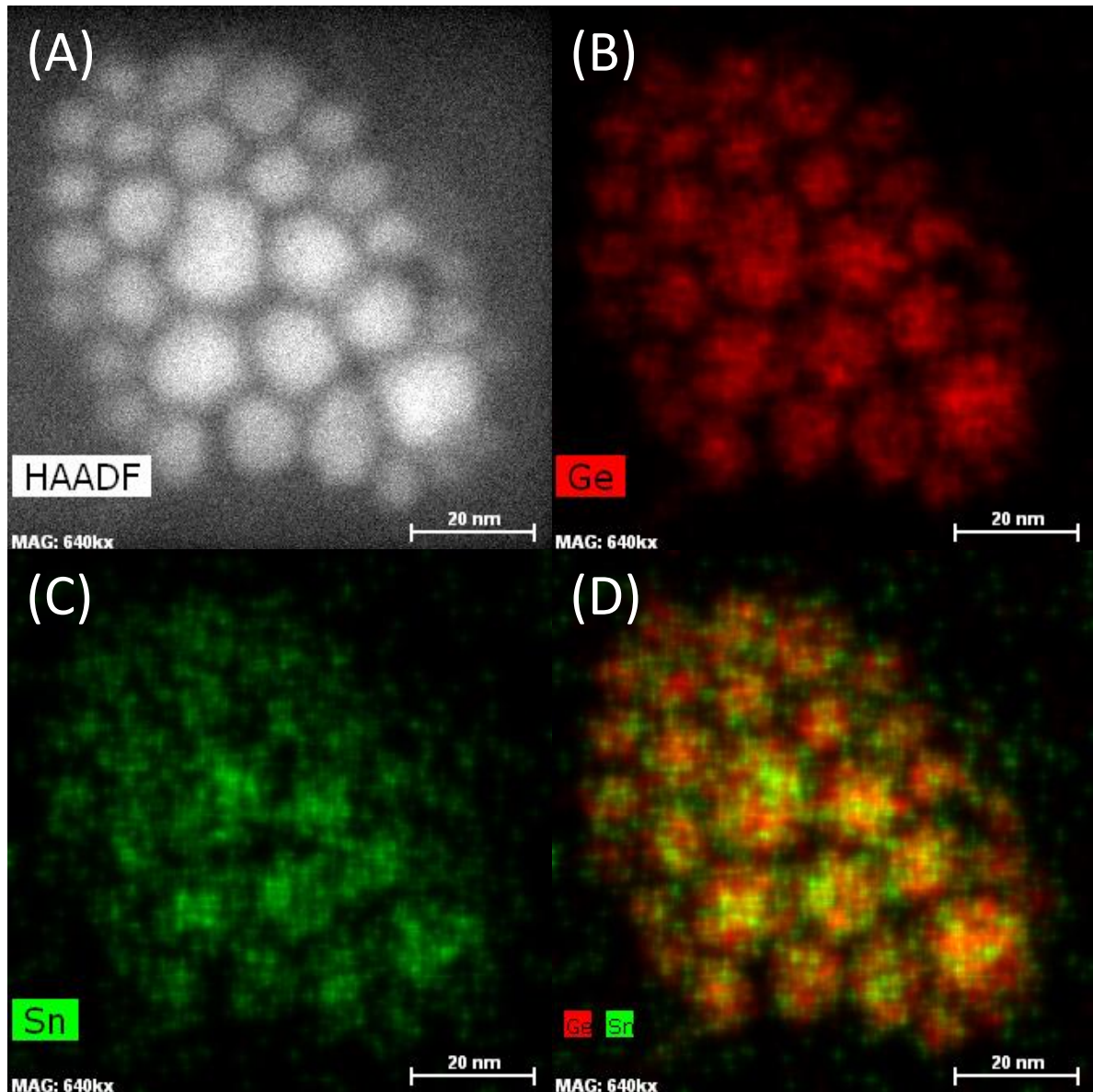
Figure 4.8. (A) Dark field TEM image of a polydisperse mixture of larger $Ge_{0.87}Sn_{0.23}$ NCs (5-20 nm) along with STEM/EDS elemental maps of (B)) Ge, (C) Sn, and (D) an overlay of Ge and Sn indicating the homogeneous distribution of elemental components throughout the lattice.
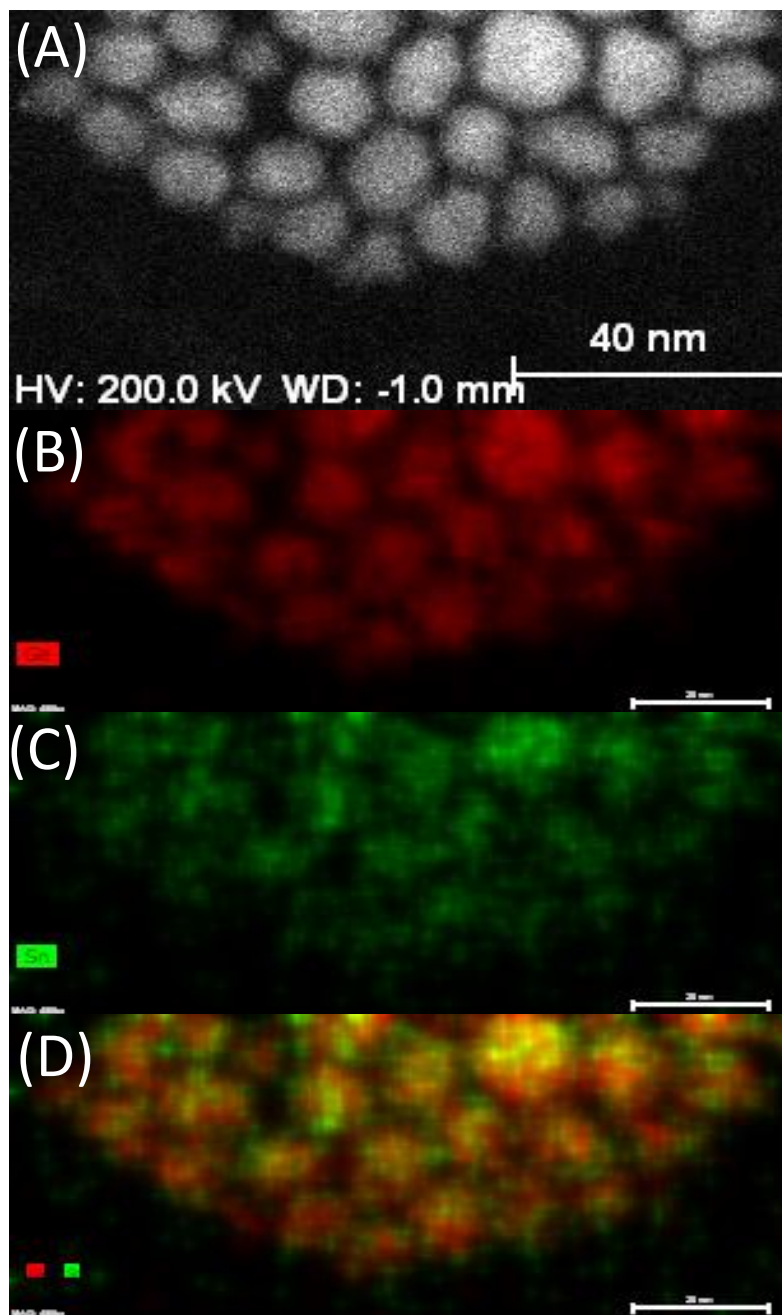
Figure 4.9. (A) Dark filed TEM image of a polydisperse mixture of larger $Ge_{0.87}Sn_{0.23}$ NCs (5-20 nm) along with STEM/EDS elemental maps of (B) Ge, (C) Sn, and (D) an overlay of Ge and Sn indicating the homogeneous distribution of elemental components in this size regime.

The small particle sizes achieved for alloy QDs have resulted in strong confinement effects and exhibit composition tunable absorption and emission in the visible spectrum. PL spectra indicate that even with strong confinement effects, increasing the Sn content still produces a pronounced redshift in emission energy (Figure 4.10.). For $Ge_{1-x}Sn_x$ QDs with x = 0.046 and x = 0.067, there is negligible change in the PL spectral position. This can be attributed to a few different factors. First, a crystal with ~2 nm diameter consists of only a few hundred atoms. This means that for a 2% difference in composition only ~5-10 atoms are substituted in the entire nanocrystal. Combined with variation in the distribution of Sn atoms within the crystal, only a small change in energy gap may result for ultra-small QDs. This is also confirmed by theoretical calculations, which show that the alloying effect becomes less pronounced for smaller QDs (Table 4.2). Nonetheless, there is a clear redshift for $Ge_{1-x}Sn_x$ QDs of x = 0.018 to x = 0.236 with PL maximum shifting from 2.00 to 1.72 eV (620-720 nm) consistent with expected Sn alloying effects. PL quantum yield (QY) were measured with respect to Rhodamine 101 and indicate values form ~0.8-1.1 %.
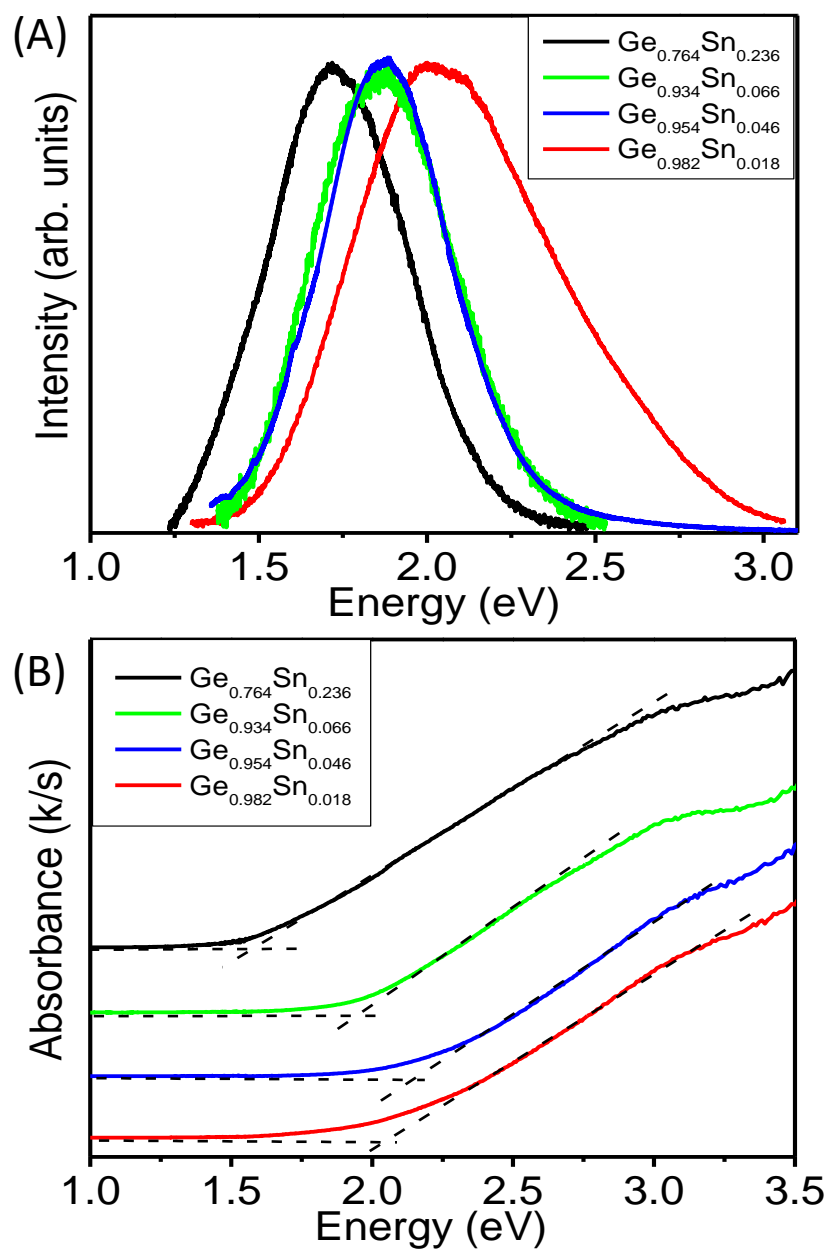
Figure 4.10. Solid-state (A) photoluminescence and (B) absorption spectra of $Ge_{1-x}Sn_x$ QDs with varying Sn composition. Absorption onsets were obtained from intersects of the dashed lines.

Table 4.2. Theoretical energy gaps calculated for different sizes and compositions of $Ge_{1-x}Sn_x$ QDs along with experimental composition analysis, absorption onsets, and PL peak maxima.

Theory		
Sn content (x)	2.1 nm QDs energy gap (eV)[a]	2.7 nm QDs energy gap (eV)[a]
0.00	2.52	2.01
0.05	2.50	1.96
0.10	2.48	1.86
0.20	2.36	1.79
Experimental		
Sn content (x)[b]	Absorption onset (eV)[c]	PL peak (eV)
0.018 ± 0.07	2.05	2.00
0.046 ± 1.2	2.16	1.80
0.066 ± 0.5	1.96	1.86
0.236 ± 1.4	1.56	1.72

[a]Theoretical energy gaps were obtained using tuned HSE hybrid functional. [b]SEM/EDS was employed to determine the elemental compositions. [c]Absorption onsets were determined from intersection of baseline with the first major increase in absorption.

For comparison, diffuse reflectance spectroscopy was employed to measure the absorption onsets of alloy QDs. The reflectance data were converted to pseudo-absorption using the Kubelka-Munk remission function.[72] The absorption onsets (Figure 4.9B) are greatly blue shifted from those of larger $Ge_{1-x}Sn_x$ QDs (1.29-0.40 eV) that have been previously reported with similar compositions (x = 0.0-0.42).[59, 63] A clear

redshift is notable in the x = 0.236 sample while the other compositions all have similar onsets. Further, the absorption onsets are in close agreement with the PL peak maxima, suggesting that the emission results from fundamental energy gap transitions. It is important to note that this is the first report demonstrating $Ge_{1-x}Sn_x$ QDs with visible spectral range absorption and PL properties. Hence, to further confirm the results, theoretical calculations of electronic and optical properties were performed. In this study, diamond cubic $Ge_{1-x}Sn_x$ QDs with diameters of 2.1 and 2.7 nm, passivated with hydrogen atoms, were considered. In calculated $Ge_{1-x}Sn_x$ QD alloys, Ge atoms were randomly replaced with Sn, and equilibrium geometries were obtained by relaxing the structures within local density approximation[122] to the density functional theory. Subsequent electronic structure calculations were performed using Heyd-Scuseria-Ernzerhof (HSE) hybrid functional,[123] with exact exchange separation parameter tuned to accurately reproduce bulk Ge band structure. HSE calculations show a systematic decrease of the energy gap with increasing Sn concentration. However, the theoretical energy gaps for 2.1 nm QDs are ~0.5 eV higher than those observed experimentally, although the general trends of gap evolution with Sn concentration are in agreement (Table 4.2). Furthermore, the experimental absorption/PL energies are in close agreement with the HSE calculations for 2.7 nm $Ge_{1-x}Sn_x$ QDs (Table 4.2 and Figure 4.11). This can be a result of sample polydispersity, where recombination in smaller QDs is mainly governed by the non-radiative surface states and therefore the larger QDs dominate the emission. There is also a possibility that experimental and theoretical approaches in determining the QD size have some disparity. Nonetheless, all results point to the $Ge_{1-x}Sn_x$ QDs having quantum confinement induced visible orange-red PL.

114
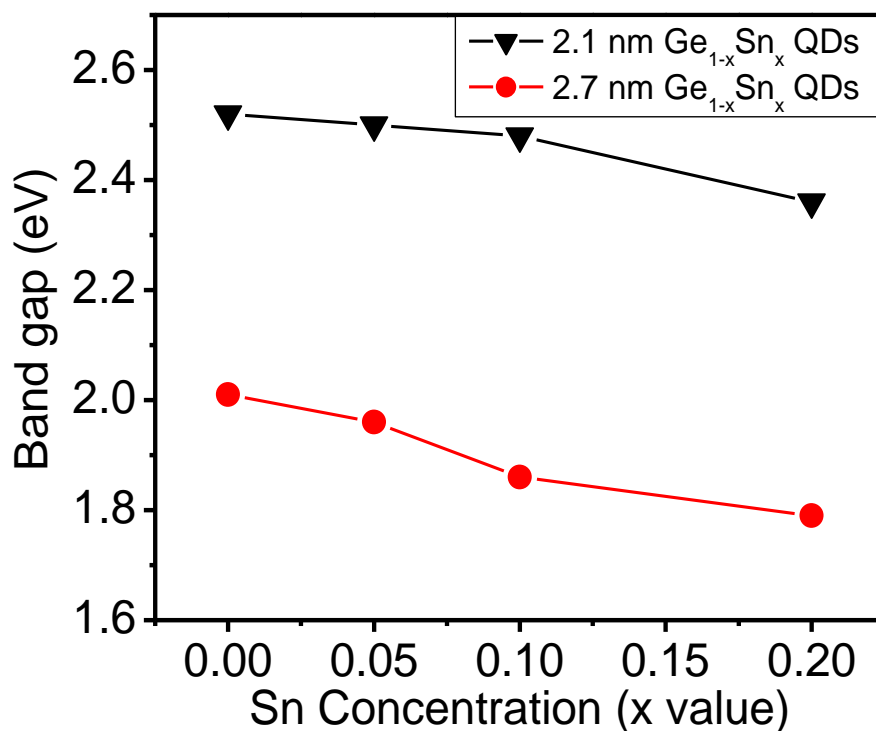
Figure 4.11. Theoretical energy gaps of 2.1 nm and 2.7 nm $Ge_{1-x}Sn_x$ QDs with varying Sn composition calculated using tuned Heyd-Scuseria-Ernzerhof hybrid functional calculations.

4.4   Conclusions

In summary, we have produced ultra-small $Ge_{1-x}Sn_x$ QDs as homogeneous solid solutions with Sn content up to x=0.236. The resultant QDs display composition tunable visible, orange-red emission. The structure of the QDs has been confirmed as diamond cubic $Ge_{1-x}Sn_x$ by PXRD and post-synthetic annealing studies whereas the Raman spectroscopy, HRTEM, and STEM data support the homogeneous solid solution behavior. Composition dependent photoluminescence (1.72-2.05 eV) and absorption (1.55-2.16 eV) energies are in agreement with theoretical energy gap calculations

performed with HSE hybrid functional. In this study, we have successfully expanded the optical window of $Ge_{1-x}Sn_x$ alloys into the visible spectrum allowing for applications in bio imaging, chemical sensing and LEDs. Further as a Group IV QD system $Ge_{1-x}Sn_x$ QDs have an advantage over other non-toxic QDs due to being more suitable for monolithic integration into existing Si-based technologies.

CHAPTER 5

Energy Gap Tuning and Carrier Dynamics in Colloidal Ge$_{1-x}$Sn$_x$ Quantum Dots

5.1   Introduction

Germanium is widely used as an infra-red (IR) optical material in photodetectors, thermal imaging cameras, phosphors, and light emitting diodes.[124-126] However, the major limitation for efficient use of Ge in optical/optoelectronic applications is its indirect bandgap, which requires phonons for optical transitions. It has been shown that the band structure of Ge can be modified by alloying with Sn to reduce the energy difference of first direct and indirect transitions, and beyond a certain Sn concentration (6 − 20%, depending on the strain) an indirect-to-direct bandgap crossover is expected.[127-130] Ge$_{1-x}$Sn$_x$ alloy has therefore attracted significant interest for the next generation of Si-compatible electronic and photonic devices. However, incorporation of Sn (bandgap, E$_g$ = 0.08 eV) dramatically reduces the fundamental energy gap of Ge$_{1-x}$Sn$_x$ alloy deep into the mid infrared (0.35 – 0.80 eV for x = 0.15 – 0.00), limiting its potential in visible to near infrared (NIR) optoelectronics. To extend the potential spectral range, quantum confinement effects have been utilized to produce Ge$_{1-x}$Sn$_x$ alloy nanostructures. Quantum dots (QDs)[59, 63] and nanowires (NWs)[58, 60] have been demonstrated both at weakly confined and somewhat strongly confined regimes that promote wider energy gaps, in addition to enhancing the optical efficiency.[61]

Thin films of $Ge_{1-x}Sn_x$ alloy produced via chemical vapor deposition and molecular beam epitaxy are well-studied and exhibit composition-tunable energy gaps in the mid-IR region.[14, 23, 37] However, growth of homogeneous $Ge_{1-x}Sn_x$ thin films is challenging due to the emergence of phase segregation in high temperature syntheses, inherent poor crystallinity, and high density of defects created with low temperature synthesis.[33, 131] In contrast, colloidal synthesis is a low-cost alternative approach to attain high quality, solution-processable $Ge_{1-x}Sn_x$ QDs without phase segregation of Sn while tuning the energy gaps through variation of size and/or composition.[59, 63] The synthesis of phase-pure $Ge_{1-x}Sn_x$ nanocrystals (NCs) with sizes in the range of 15 − 23 nm and 3.4 − 4.6 nm with up to x = 0.279 and gap energies of 1.29 − 0.75 eV have been recently demonstrated.[59] Moreover, larger $Ge_{1-x}Sn_x$ NCs (9 − 12 nm) with tunable energy gaps in the near-to-mid IR region (1.04 − 0.41 eV) have also been reported.[63] However, no study has so far produced small enough $Ge_{1-x}Sn_x$ QDs with visible photoluminescence (PL). In this work, we report the first systematic study of optical transition energies and carrier dynamics at room and cryogenic temperatures in colloidally synthesized ultra-small $Ge_{1-x}Sn_x$ QDs (~2.0 ± 0.8 nm) as a function of Sn concentration (x = 0.055 − 0.236) by employing steady-state and time-resolved PL spectroscopy and *ab initio* calculations.

5.2   Experimental Methods

5.2.1 Materials:

Tin dichloride (>99.9985 % Ultra-Dry) and Germanium diiodide (99.99+ %) were purchased from Alfa Aesar and Strem Chemicals, respectively and stored in a N_2 glove box. Oleylamine (OLA, 80-90%) and 1-octadecene (ODE, 90%), were purchased from

Fisher Scientific. N-butyllithium (BuLi) 1.6 M in hexane was purchased from Sigma Aldrich. ACS grade solvents such as methanol, carbon tetrachloride, and toluene were purchased from Acros. ODE and OLA were dried by heating at 120 °C under vacuum for one hour prior to storage in a N_2 glovebox. Methanol and toluene were distilled prior to use after drying with molecular sieves and Na, respectively. Carbon tetrachloride was degassed by bubbling N_2 through it and was stored under inert conditions.

5.2.2 Synthesis of Ultra-small $Ge_{1-x}Sn_x$ QDs:

A wet-colloidal strategy was used to produce $Ge_{1-x}Sn_x$ QDs with a diameter of 1.5-2.2 nm and Sn compositions of x = 0.055, 0.071, 0.125, and 0.236. Details of the synthesis procedures have been discussed elsewhere,[59] with the major change in procedure being the varied concentration of the reducing agent. Briefly, the appropriate molar ratios of GeI_2 and $SnCl_2$ (0.6 mmol total) and 20 mL of oleylamine were loaded into a three neck round bottom flask under air-free conditions. This mixture was stirred and degassed for ~8 min while heating to 115 °C then heated to 230 °C (~10 °C/min) prior to injection of the reducing agent. The reducing agent used was n-butyllithium (BuLi) diluted in 3 mL of 1-octadecene and the amount of BuLi used varied from 0.5-0.9 equivalents of the precursor halide concentration. After injection, the temperature was ramped to 300 °C at a rate of ~6 °C/ min, before being cooled by compressed air (~5 min). Resultant QDs were isolated by a mixture of toluene ~5−10 mL followed by methanol ~60−90 mL, and purified by dispersing in toluene and precipitating with methanol twice.

5.2.3 Synthesis of larger $Ge_{1-x}Sn_x$ particles:

For STEM/EDS analysis, a set of larger, polydisperse $Ge_{1-x}Sn_x$ QDs (5-20 nm) were produced using a similar synthetic procedure. To ensure a good comparison can be made between larger and the ultra-small QDs all parameters were kept constant except the growth time at 300 ºC. After all initial heating, nucleation and growth stages, the resultant $Ge_{1-x}Sn_x$ nuclei were grown at 300 °C for 10 min to produce $Ge_{1-x}Sn_x$ QDs with sizes ranging from 5-20 nm.

5.2.4 Characterization:

For optical measurements, QD samples dispersed in carbon tetrachloride were spin-coated on sapphire or silicon substrates and mounted on a closed cycle He cryostat. Steady-state PL and TRPL measurements were performed using a frequency doubled Ti:sapphire laser (385 nm wavelength, 150 fs pulse width, 8 kHz to 80 MHz repetition rate) as the excitation source. A liquid N_2 cooled charge coupled device (CCD) camera connected to a spectrometer was employed to collect the steady-state PL spectra, and a Hamamatsu streak camera with 25 ps temporal resolution was used to analyze the PL transients. Hitachi FE-SEM Su-70 model scanning electron microscope operating at 20 keV, coupled with an *in situ* EDAX energy dispersive x-ray spectroscopy detector unit was employed for the elemental analysis. TEM images were collected on a Zeiss Libra 120 model microscope operating at 120 kV. STEM images were recorded on a FEI Titan 8300 microscope equipped with a Gatan 794 multiscan camera operating at 300 kV. Samples for TEM analysis were prepared by drop casting the QDs in CCl_4 onto carbon coated copper grids, followed by evaporation of the solvent. Powder X-ray diffraction measurements were performed with a PANalytical X'Pert PRO X-Ray diffractometer

calibrated with Si standard and equipped with a Cu Kα anode (κα= 1.54 Å). Purified QDs were deposited on to a low background sample holder and diffraction patterns were collected at 45 kV and 40 mA operating conditions.

5.2.4 Computational calculations:

Calculations of the energy gaps and optical properties were performed using several levels of theory. Alloy QD supercells were created using ideal bulk Ge bond lengths. QD diameters were varied from 1.4 nm to 2.7 nm, with dangling bonds passivated by hydrogen. The lattice relaxation method was used within local/semilocal approximation of the density functional theory (DFT), since lattice properties are usually reproduced by either local density approximation (LDA) or generalized gradient approximation (GGA) reasonably well. It has been shown in the literature, and confirmed by our calculations, that GGA relaxation of bulk Ge using some parameterizations of GGA (for example, a widely-used Purdue-Burke-Ernzerhof)[115] yields overestimated lattice constants of both Ge and Sn. This leads to the lattice structure of Ge with a PBE computed direct band gap at the Γ-point, instead of experimentally observed indirect bandgap with conduction band minimum at L-point. On the other hand, LDA[122] underestimates the lattice constants very slightly, and yields the structure corresponding to the correct indirect band gap. Therefore, lattice relaxations were performed using LDA approximation to the DFT, with forces minimized to 0.05 eV/Å or less. In order to correctly reproduce the electronic levels of alloy QDs, we used tuned Heyd-Scuseria-Ernzerhof (HSE) hybrid functional calculations.[123] In HSE hybrid functional, the PBE exchange correlation part of the density functional is mixed with a Fock-type exchange in varying proportions at short range. In our calculations, the fraction of exact exchange was kept at a standard 25%, while the

exchange range separation parameter was increased to 0.29 Å^{-1}, corresponding to the exchange screening length of 6.9 Å. These parameters were found to reproduce bulk band structure of Ge in excellent agreement with experiment. Using time-dependent hybrid functional calculations (TD-HSE), following Ref. 132, based on the tuned hybrid HSE functional, the optical and excitonic properties were calculated for smallest alloy QDs (1.4 nm). The trends in these properties are not expected to depend on size within the range of sizes explored here. The PL lifetimes were determined by thermal averaging of the radiative transition rates obtained from the oscillator strengths computed from TD-HSE. All calculations were performed using Vienna *ab initio* simulation package (VASP)[117] with projector augmented plane-wave (PAW)[116] method to describe core electrons.

5.3   Results and Discussion.

Four $Ge_{1-x}Sn_x$ QD samples with varying Sn content (x = 0.055, 0.071, 0.125, and 0.236) were produced by high temperature co-reduction of halides in high boiling alkyl amine/alkene solvents. Transmission electron microscopy (TEM) images of QDs (Figure 5.1) without post-synthetic size selection indicate nearly spherical morphology and narrow size dispersity with average sizes of 1.9 ± 0.4 nm, 1.5 ± 0.3 nm, 2.2 ± 0.6 nm, and 2.0 ± 0.6 nm in $Ge_{1-x}Sn_x$ QDs with x = 0.055, 0.071, 0.125, and 0.236, respectively. The x-ray diffraction patterns of QDs are consistent with the presence of diamond cubic phase typically reported for $Ge_{1-x}Sn_x$ alloy thin films and NCs (Figure 5.2). Significant broadening of Bragg reflections is consistent with the growth of ultra-small QDs. Scanning transmission electron microscopy (STEM) data support the growth of homogeneous $Ge_{1-x}Sn_x$ alloys with Ge and Sn randomly distributed in the alloy lattice (Figure 5.3-5.4). For STEM analysis, slightly larger (~5 − 20 nm) set of QDs were produced using a similar

strategy, because of the difficulty of mapping ultra-small $Ge_{1-x}Sn_x$ QDs. It should be noted that the formation of homogeneous $Ge_{1-x}Sn_x$ alloys observed for larger particles (~5 − 20 nm) is presumed to be true for smaller particles. This conclusion is based on the similar synthesis strategy used for production of larger and smaller QDs (longer growth time for larger particles) and the high tendency of Sn to continuously segregate and form heterostructures (cubic Ge and tetragonal β-Sn) at longer growth times. It is expected that if at any point during growth Sn segregation occurs, the formation of a homogenous final product would be extremely unlikely. Moreover, structural analysis of ultra-small $Ge_{1-x}Sn_x$ QDs (Figure 5.2) provides no evidence of heterogeneous nucleation or Sn segregation further supporting the growth of homogeneous alloys.
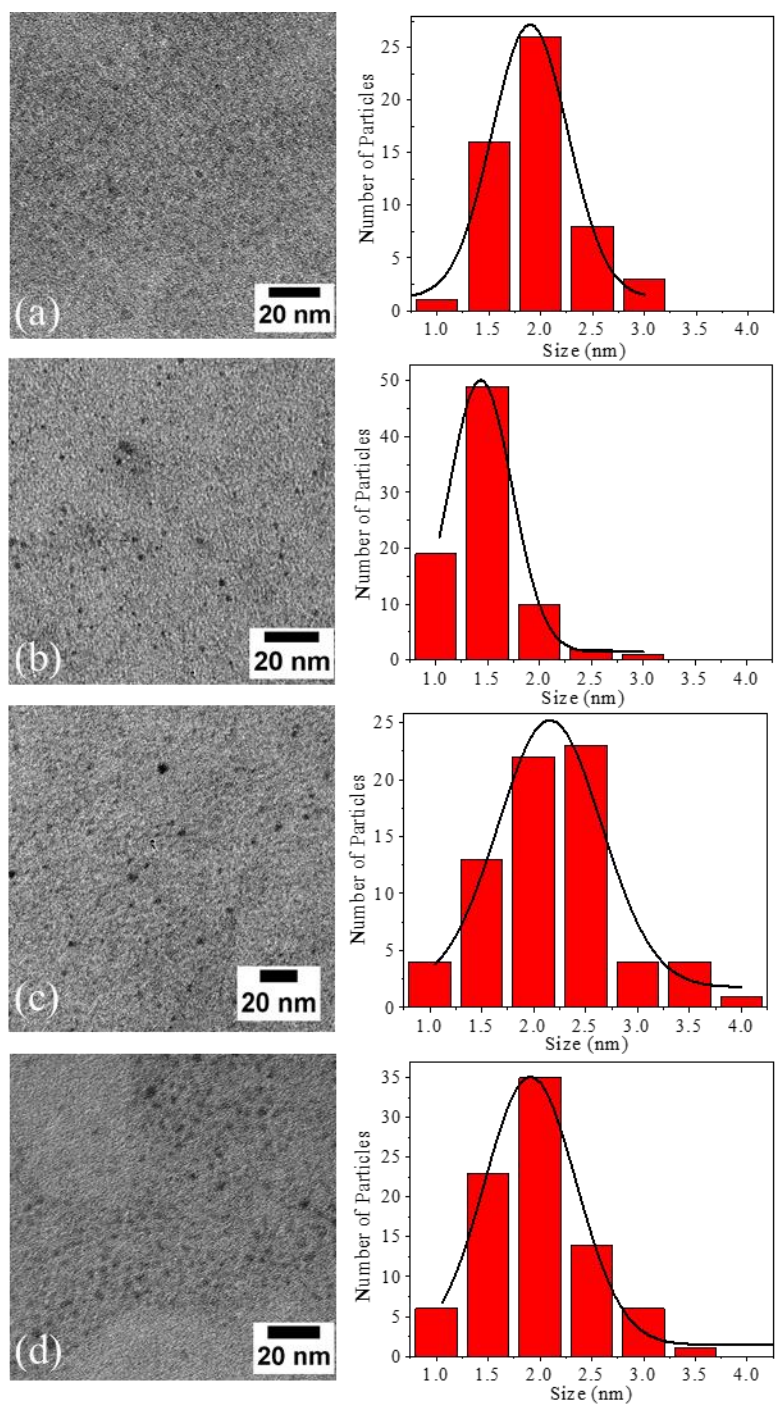
Figure 5.1. Bright field TEM images of Ge$_{1-x}$Sn$_x$ QDs with (a) x = 0. 055, (b) x = 0.071, (c) x = 0.125, and (d) x = 0.236. The corresponding size histograms of Ge$_{1-x}$Sn$_x$ QDs without any post-synthetic size selection are also shown.
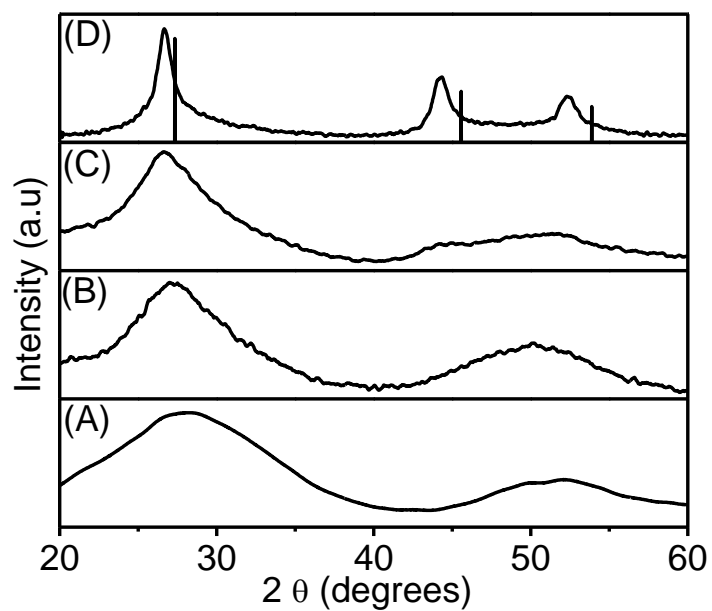
Figure 5.2. Representative Powder X-ray diffraction patterns of ultra-small (A)

$Ge_{0.945}Sn_{0.055}$ QDs (B) $Ge_{0.929}Sn_{0.071}$ QDs, (C) $Ge_{0.875}Sn_{0.125}$ and (D) larger (4-20 nm)

polydispersity $Ge_{0.87}Sn_{0.13}$ particles produced using a similar synthetic strategy, with Ge,

JCPDS File No. 01-089-5011.
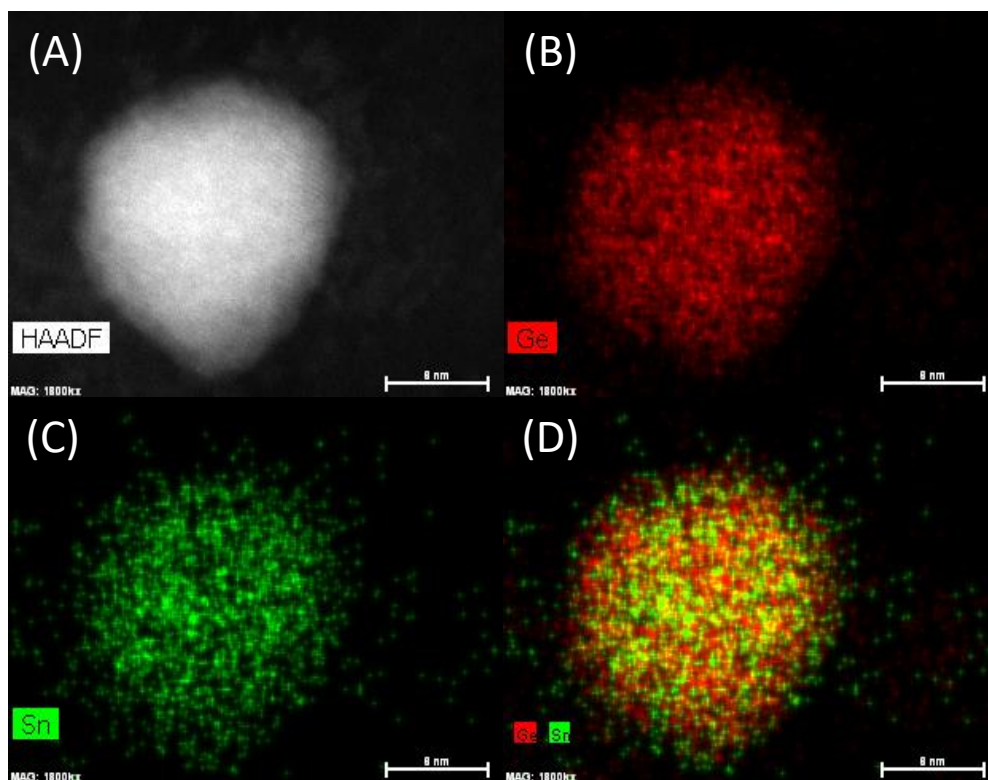
Figure 5.3. (A) High resolution TEM image of a $Ge_{0.87}Sn_{0.13}$ QD (~20 nm) along with STEM/EDS elemental maps of (B) Ge, (C) Sn, and (D) an overlay of Ge and Sn indicating the homogeneous distribution of elemental components throughout the lattice.
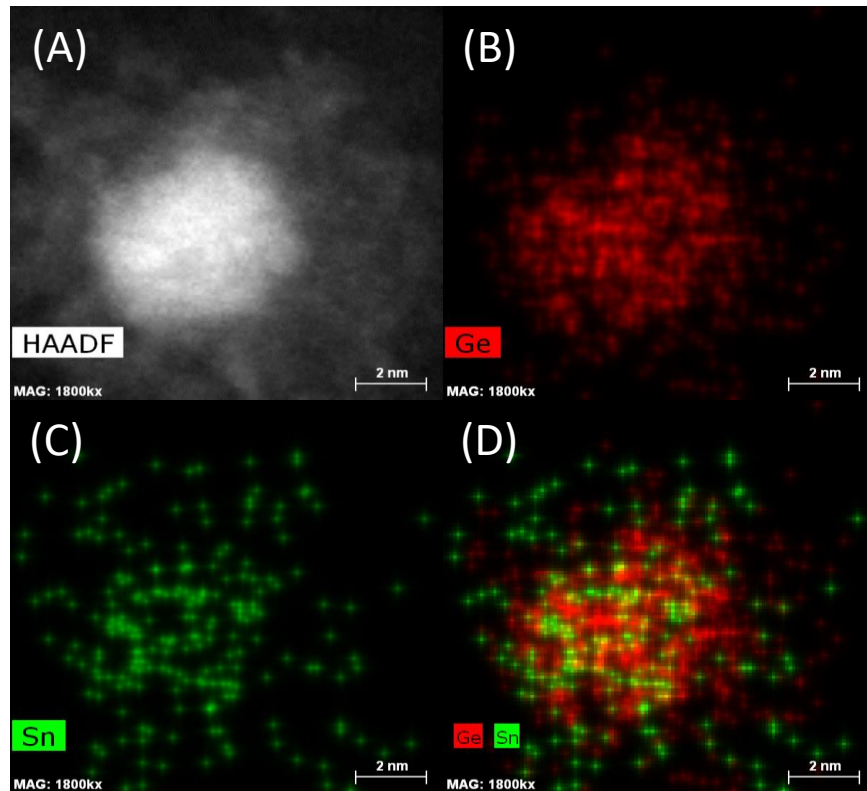
Figure 5.4. (A) High resolution TEM image of a $Ge_{0.87}Sn_{0.13}$ QD (~5 nm) along with STEM/EDS elemental maps of (B) Ge, (C) Sn, and (D) an overlay of Ge and Sn indicating the homogeneous distribution of elemental components throughout the lattice.

Figure 5.5(a) shows the steady-state PL spectra of ultra-small $Ge_{1-x}Sn_x$ QDs measured at 15 K. The PL peaks exhibit a red-shift from 1.88 eV for x = 0.055 to 1.61 eV for x = 0.236. As these alloy QDs have the same shape (nearly spherical) and average particle size (Figure 5.1), the systematic red-shift in PL can be attributed to the decrease in energy gaps due to increasing Sn content, consistent with alloying effects. Moreover, strong quantum confinement effects are evident in this ultra-small size regime as the gap energies are well above those of their thin film counterparts (~0.35 – 0.80 eV for x = 0.15 – 0.00).[15]
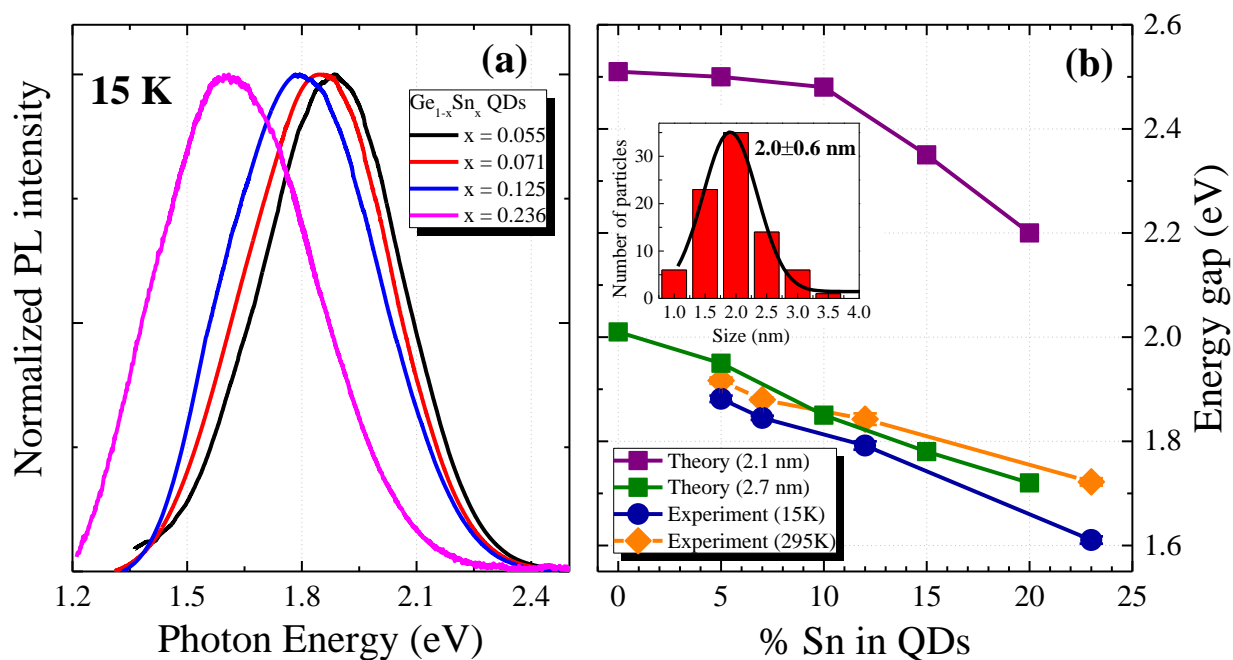
Figure 5.5. (a) PL spectra of Ge$_{1-x}$Sn$_x$ QDs with varying Sn content at 15 K, (b) experimental (PL peak) and theoretical energy gaps as a function of Sn concentration in 2.1 nm and 2.7 nm QDs. Inset shows the size histogram of Ge$_{0.77}$Sn$_{0.23}$ QD sample, representative of QDs with different Sn compositions, obtained from TEM analysis with no post-synthetic size selection.

The PL peak position, both at 15 K and 295 K, as a function of Sn content is plotted in Figure 4.5(b) along with the theoretical energy gaps calculated using tuned HSE hybrid functional for 2.1 and 2.7 nm Ge$_{1-x}$Sn$_x$ QDs. It is evident that the experimentally obtained energy gaps are consistent with theoretically calculated values for 2.7 nm QDs even though the TEM data revealed an average size of 2.0 ± 0.8 nm. This deviation can be attributed to size variation within an experimental sample, where the PL is dominated by emission from the larger QDs because of their better surface passivation by ligands

resulting in reduced non-radiative decay pathways. For smaller QDs, the long carbon chain and the bent structure of the surfactant (oleylamine, OLA) would become more detrimental to ligand packing, leading to reduced surface passivation due to steric hindrance of neighboring surfactant ligands. This discrepancy can also be attributed to differences of theoretical and experimental size estimations, which is previously observed in Group IV QDs.[133] With increasing excitation density from 40 mWcm^{-2} to 40 Wcm^{-2}, PL peaks at 15 K were observed to blue shift by 14 − 19 meV. In contrast, Wen *et al.*[134] reported blue shifts of 20 and 120 meV in Si QDs of sizes 2.5 and 3.8 nm, respectively when the excitation density was increased by three orders of magnitude at room temperature. They explained their observation using the Y-band theory which is compared with our proposed model below. The larger shift in 3.8 nm QDs was ascribed to quantum confinement effects and the saturation of lower energy core states. However, the smaller shift in 2.5 nm QDs, where quantum confinement should be even stronger, was attributed to the dominance of luminescence from surface states, which could not be fully saturated. As discussed in detail below, our experimental and theoretical data suggest that the small blue shifts observed for Ge$_{1-x}$Sn$_x$ QDs with increasing excitation density at 15 K are most likely due to emission from higher energy surface states, the depth of which increases with Sn content, as well as the higher energy excitons in the QD core.

As shown in Figure 5.5(b), for all the samples PL peaks at room temperature are blue shifted compared to those at 15 K. One of the reasons for this temperature dependence can be the exchange splitting between dark and bright exciton states. An exciton in which the electron and the hole spins are parallel (s = 1) forms an optically inactive triplet state, referred to as the dark exciton. Since in this case the optical transition is spin-forbidden,

it is characterized by a long decay time.[135] In contrast, a singlet s = 0 exciton state, referred to as the bright exciton, is formed if spins of the electron and the hole are antiparallel. This state is optically active and has a short life time. Calculations show that at low temperatures and in the absence of surface traps, excitons in the QDs occupy the lower-energy dark states and PL emission originates from these states. As the temperature increases, thermal activation of higher energy bright excitons takes place and consequently PL emission blue-shifts. Due to the electron-hole exchange interaction, these dark and bright exciton states are separated by an energy Δ_{db}, which can be several meV to several tens of meV depending on the material system as well as on the size of QDs.[136] In case of 2.7 nm diameter QDs, Δ_{db} has been reported to be 15, 20, 25, and 40 meV in CdSe, Si, CdTe, and GaAs QDs respectively.[137-140] Our calculations for the GeSn alloy QDs predict that in 2.7 nm dots this splitting is roughly 20 − 30 meV. Furthermore, calculations also suggest that this dark-bright exciton splitting should decrease from ~30 to ~20 meV with Sn concentration increasing from zero to 20%. However, the experimentally observed shift between the room temperature and low temperature PL peaks increases from 35 meV in $Ge_{1-x}Sn_x$ QDs with x = 0.055 to 110 meV in $Ge_{1-x}Sn_x$ QDs for x = 0.236 Sn. These values are significantly larger than those suggested by calculations as well as those reported in the literature. Moreover, the trend of increasing difference in PL peaks at 15 K and 295 K with increasing Sn content is inconsistent with the theoretical predictions. The temperature shifts of PL peaks can therefore be explained by the surface traps, which are likely to be present due to incomplete passivation by the ligands. This would suggest that low temperature PL includes contributions from the surface traps as well as the slowly decaying dark excitons. Unpassivated sites and

surface defects create localized states at the surface, with energy levels within the gap. As a result of thermalization of the photoexcited carriers, the electron (or the hole, or both) can be trapped at such a surface state, with subsequent radiative recombination with a hole in the HOMO (or electron in the LUMO). Such a spatially separated electron hole pair, at low temperature, could recombine radiatively with a long lifetime and PL energy below the gap. With increasing temperature, the electron (or hole) trapped at the surface can be thermally ejected into the LUMO (or HOMO), with subsequent HOMO-LUMO radiative recombination. Therefore, the blue shift with temperature, particularly for the $Ge_{1-x}Sn_x$ QDs with x = 0.236 (~110 meV) where the increased alloy disorder can potentially create high density of deeper traps, might mainly be due to detrapping from surface states. From the temperature dependent shifts in PL peaks [Figure 5.5(b)], it is evident that the surface trap depth increases with increasing Sn content. It should also be noted that the observed 14 − 19 meV blue shift with increasing excitation density (by three orders of magnitude) at 15 K can be attributed to the saturation of deeper surface traps, which results in emission from shallower surface states.

In order to reveal the dynamics involving different recombination processes of non-equilibrium carriers, time-resolved PL spectroscopy was employed. PL transients measured at 15 K are shown in Figure 5.6. All samples exhibit biexponential PL decays, where the fast decays are most likely associated with surface recombination (radiative component) and slow decays are due to radiative recombination of dark excitons in the QD cores. In QDs containing surface defects, carrier trapping is usually significantly faster than radiative recombination in the core which leads to this two-component PL decay.[133] The surface state radiative recombination lifetimes derived from our calculations are on

the order of 1 μs in ~2 nm $Ge_{1-x}Sn_x$ alloy QDs, consistent with the fast decays in Figure 5.6, and are practically independent of temperature.

A biexponential decay function $A_{fast}e^{-t/\tau_{fast}} + A_{slow}e^{-t/\tau_{slow}}$ was used to fit the PL transients, where time constants τ_{fast} and τ_{slow} represent the fast and the slow decay components, respectively. As shown in Figure 5.7(a) and Table 5.1, τ_{slow} (~ 24 μs) and τ_{fast} (~ 4 μs) at 15 K are practically independent of the Sn content for up to x = 0.125, but decrease significantly to 3 μs and 0.5 μs, respectively, for x = 0.236, consistent with the expected higher density and deeper surface traps due to increased alloy disorder.
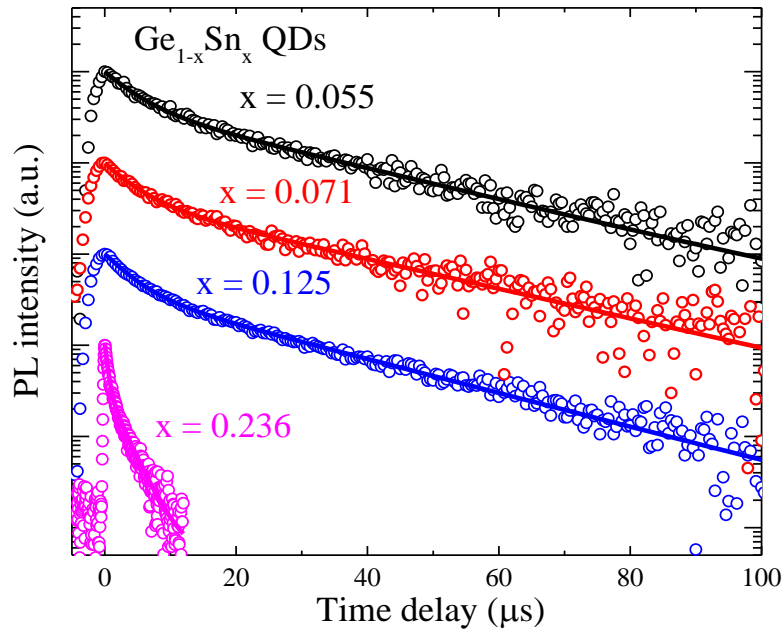
Figure 5.6. PL transients of the $Ge_{1-x}Sn_x$ QD samples of different Sn composition at 15 K.
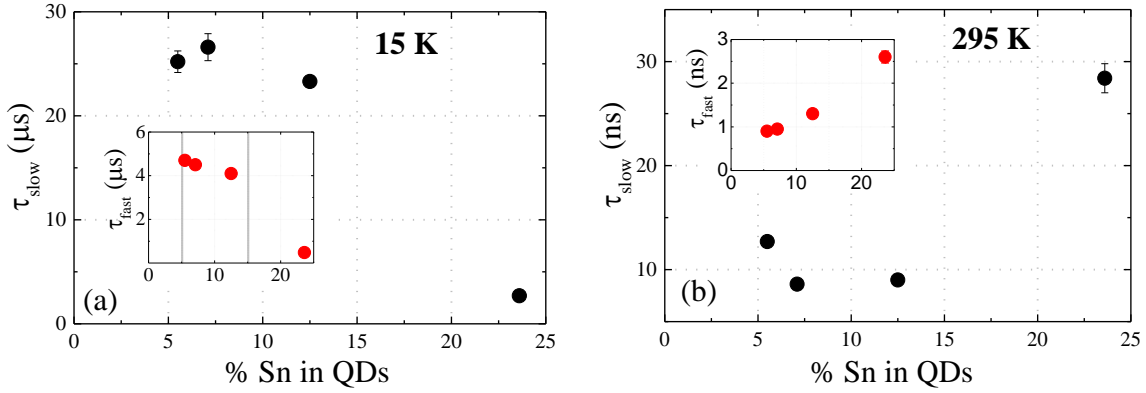
Figure 5.7. PL decay times measured at (a) 15 K and (b) 295 K as a function of %Sn in Ge$_{1-x}$Sn$_x$ QDs. Fast decay components are shown in the insets of (a) and (b).

Table 5.1 Decay times and amplitude ratios obtained from biexponential fits to PL transients at 15 K and 295 K.

Sn content (x)[a]	15 K			295 K		
	T$_{fast}$ (µs)	T$_{slow}$ (µs)	A$_{fast}$ / A$_{slow}$	T$_{fast}$ (ns)	T$_{slow}$ (ns)	A$_{fast}$ / A$_{slow}$
0.055	4.7±0.2	25.2±1.0	1.3	0.9±0.03	12.7±0.4	5.4
0.071	4.5±0.2	26.6±1.3	1.5	0.9±0.2	8.6±0.3	3.1
0.125	4.1±0.1	23.2±0.5	1.6	1.3±0.02	9.0±0.3	2.8
0.236	0.5±0.02	2.7±0.13	2.0	2.6±0.1	28.4±1.4	1.8

[a] Sn content determined from energy dispersive spectroscopy, averaging 5 individually measured points.

Our calculations suggest that in colloidal Ge$_{1-x}$Sn$_x$ QDs, possible interplay between surface state localized carriers and dark-bright exciton splitting is responsible for the observed optical response. Time-dependent HSE calculations indicate that dark excitons should have a lifetime of ~1 − 10 µs at x = 0, *i.e.* for phase pure Ge QDs, followed by roughly an order of magnitude drop for x = 0.05 and nearly no change for higher Sn concentrations. However, as discussed above, the PL peak shifts with temperature suggest a significant contribution from surface traps. Therefore, at low temperatures, long biexponential decays suggest that carriers could be localized at the surface, with small overlap between the wavefunctions.[141, 142] The slow surface recombination of localized carriers could explain the fact that until concentrations of Sn reach x = 0.236, there is almost no change in PL lifetime. Calculations also suggest that alloying with Sn smears the separation between dark and bright excitons in Ge$_{1-x}$Sn$_x$ alloy QDs, introducing excitons with increasing optical oscillator strength with increasing Sn content. This combination of surface trap emission and exciton recombination in the core of QD would lead to averaged decrease in PL lifetimes of excitonic transitions, revealed at high Sn concentrations.

PL decay times were found to be much faster at room temperature. As shown in Figure 5.7b), τ_{slow} is around 10 ns for QDs with x up to 0.125 and 28 ns for x = 0.236. This dramatic decrease of three orders of magnitude in decay times with increasing temperature is most likely a result of thermal activation of singlet bright exciton transitions, while the PL decay at 15 K is dominated by slow recombination of spin-forbidden triplet dark excitons and recombination of carriers localized at surface traps. From our calculations, the recombination of carriers localized on deep surface traps is found to be

independent of temperature when lattice vibrations are neglected. In experiment, this recombination is likely somewhat dependent on temperature, since at higher temperatures overlap between the surface state and the core carrier wavefunctions significantly increases due to the increased thermal vibrations. However, this dependence is not as dramatic as the lifetime difference between dark and bright exciton recombination. Therefore, room temperature PL is likely dominated by the bright exciton recombination in the core of the QD. This dark-bright exciton splitting induced change in PL decay times with increasing temperature is consistent with the steady-state PL results discussed above and has also been observed in colloidal QDs of PbSe, CdSe, and Ge.[76, 133, 143] According to our calculations, room temperature lifetimes for radiative transitions, which are dominated by bright excitons, have almost no dependence on Sn concentration (only very weakly decreasing with Sn), and are around 10 − 20 ns.

To explore the origin of the fast decaying component (τ_{fast}) at room temperature, we investigated the temporal dependence of PL spectra (Figure 5.8), which revealed the existence of a very short lived (<1 ns) emission (at 2.2 − 2.3 eV during the first 1 ns time window) possibly originating from higher energy bright excitonic states. This emission cannot be observed in the spectra recorded at times longer than 2 ns, therefore, leading to the fast component in PL transients. It is also not observed in the steady-state PL spectra because its integrated intensity is much weaker than the longer-lived emission from the lowest energy bright exciton states. Furthermore, no such short-lived PL peak was observed in low temperature PL spectra collected at different time delays.

PL decays at room temperature are also strongly affected by non-radiative surface recombination as evidenced by the much weaker intensities compared to those at 15 K.

The ratios of time and spectrally integrated PL intensity at 295 K to that at 15 K for all the QDs samples were found to be <10%, providing an upper limit for the quantum yield. At 15 K, surface traps are at least in part radiative as suggested by the lower energy emission compared to room temperature. However, nonradiative channels most likely become accessible at room temperature as the trapped carriers can overcome the associated energy barrier via thermal excitation. The fast recombination component at 295 K, might therefore, have contributions from the nonradiative decay through surface traps. In summary, carrier relaxation pathways at 15 K include primarily non-radiative and radiative recombination at the surface traps. At 295 K, carrier de-trapping from the surface and activation of bright exciton recombination take place, with non-radiative surface recombination being dominant.
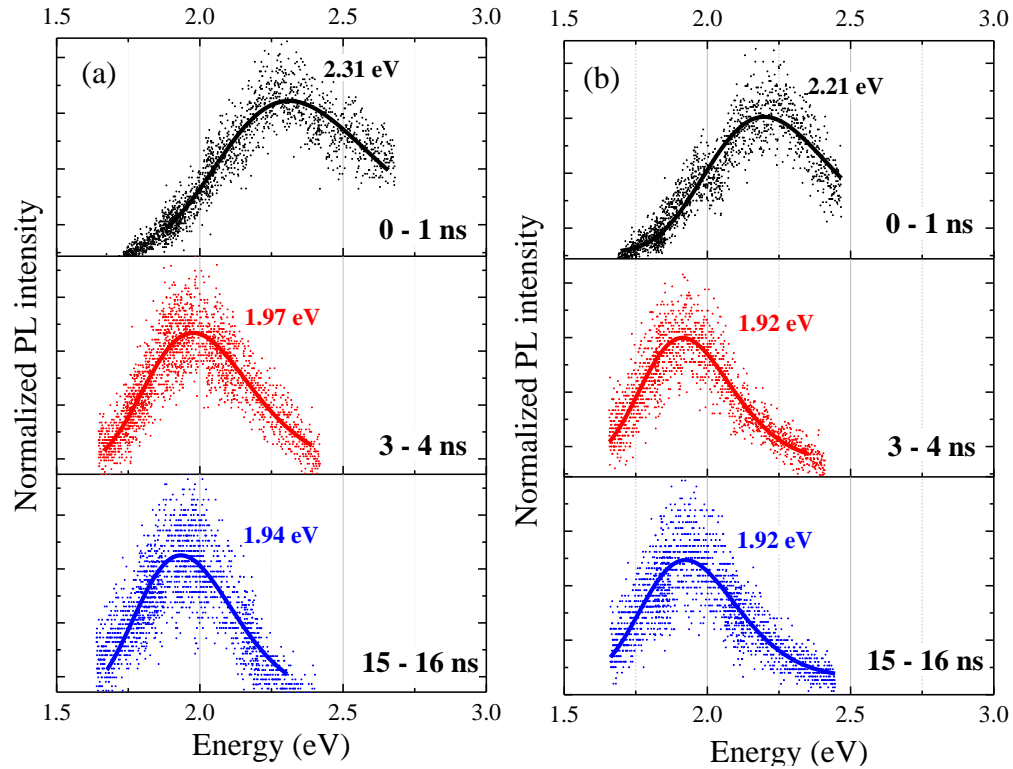
Figure 5.8. Temporal dependence of room temperature PL spectra (along with their corresponding Gaussian fitting) for $Ge_{1-x}Sn_x$ QD samples with (a) x = 0.055 and (b) 0.071. Other QD samples exhibit similar behavior.

Figure 5.9 summarizes the PL mechanisms identified in ultra-small $Ge_{1-x}Sn_x$ alloy QDs. The discrete excitonic states in the core of the QD (on the left) are adjacent to the surface states, i.e. shallow electron traps and hole traps with densities of states N(E) below the excitonic transitions. The theoretically estimated dark-bright exciton splitting is 20 meV. Experimentally measured blue shift of the PL peak with temperature suggests that the shallow electron traps are at 35-110 meV below the band edge. At low temperature, following the above the gap excitation, the lowest energy excitonic state for the electron-hole pair is the neutral dark exciton X_D^0. In addition, the electron and hole can be trapped at the localized spatially separated electron and hole traps. In both

137

cases the radiative recombination has low probability, resulting in the long low

temperature lifetimes. At room temperature, bright exciton recombination leads to

significantly shorter lifetimes. Surface state radiative recombination also occurs faster;

however, this effect is less pronounced compared to switching on the bright excitons

and due to detrapping. With the admixing of Sn to $Ge_{1-x}Sn_x$ quantum dots, the radiative

lifetime is expected to decrease, due to the introduction of dark-bright exciton mixing

and effective reduction of electron-hole exchange splitting.
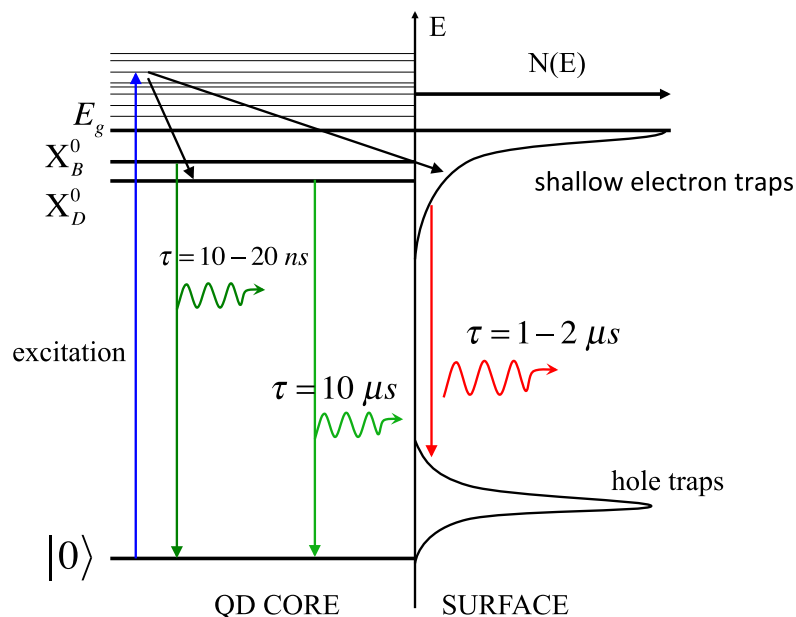
Figure 5.9. Schematic diagram of the radiative recombination pathways in $Ge_{1-x}Sn_x$ alloy

QDs.

According to the Y-band theory, it is not possible to tune the emission energy in Si

QDs beyond 2.1 eV, which corresponds to the energy of the yellow emission band, by

decreasing the size of the QDs.[134] We have not observed any evidence for the emission

energy tunability limit due to presence of high energy surface states (so-called Y-band in

the case of Si QDs) with reduction of the size of QDs. Instead, the surface states we have reported are at energies lower than those corresponding to the bright exciton states in the QD cores, and both energies can be tuned by changing the Sn content. However, we do not rule out any similarities between the two models, and further studies with different sizes of QDs are required for a better comparison.

5.4   Conclusions

In conclusion, we reported, for the first time, on the tunability of energy gap and carrier dynamics in colloidally synthesized 2.0 ± 0.8 nm $Ge_{1-x}Sn_x$ QDs (x = 0.055 − 0.236) having visible luminescence and developed a model for their radiative recombination pathways. Energy gaps at 15 K, as deduced from steady-state PL measurements, were confirmed to reach the visible spectral range, varying from 1.88 eV to 1.61 eV by changing Sn content from x = 0.055 to x = 0.236, respectively. Taking the size and compositional variation of these QDs into account, experimental energy gap values were fairly consistent with theoretically calculated ones. PL decay times were found to be 3 − 27 μs at 15 K due to the slow recombination of spin-forbidden dark excitons and recombination of carriers trapped at surface states. They dramatically decreased to 9 − 28 ns at room temperature owing to the thermal activation of spin-allowed bright excitons and carrier de-trapping from surface states.

CHAPTER 6

CONCLUSIONS AND PROSPECTUS

The content of this dissertation has successfully laid the appropriate groundwork for the motivation behind pursing the development of $Ge_{1-x}Sn_x$ nanocrystals, set defined goals for the development of a synthetic method (Goal 1), exploration of size dependent optical properties (Goal 1 and Goal 2), and advanced spectroscopic studies to guide future device development (Goal 3). Each of these three goals has been achieved thoroughly and explored in detail.

The development of a colloidal synthesis for $Ge_{1-x}Sn_x$ nanocrystals was previously unexplored, despite the high potential of $Ge_{1-x}Sn_x$ alloys in optoelectronic applications. The method reported herein is the first to successfully gain control over a wide range of sizes and compositions without any undesired side products. This was accomplished by co-reduction of metal-salts (GeI_2 and $SnCl_2$) through a hot injection of a strong reducing agent (n-butyllithium) in a strongly coordinating solvent (oleylamine). While hot-injection methods are well known for the production of high quality semiconducting nanocrystals, the inherent instability of $Ge_{1-x}Sn_x$ as a bulk system and preferential growth of β-Sn over α-Sn at high temperature introduces many complicating factors. As such, fine control over the nucleation stage was found to be of the utmost importance in preventing the separate growth of Ge and Sn nuclei. Heterostructure nucleation was eliminated by limiting the ability of Sn to self-nucleate with a two-fold strategy. First a relatively large volume of solvent was utilized (10-20 mL), minimizing

the chance of Sn-Sn collisions. The second was by determining a nucleation temperature (210-230 °C) that would destabilize any Sn nuclei that might still form while still allowing $Ge_{1-x}Sn_x$ alloy nuclei to coalesce. Growth of size, shape, and composition controlled $Ge_{1-x}Sn_x$ alloy nanocrystals permitted in-depth studies into structure-property relationships.

Three different size sets of homogeneous $Ge_{1-x}Sn_x$ nanocrystals were studied. The largest set, 15-23 nm, played a crucial role in understanding the nucleation and growth stages of the synthesis. At this size range composition control was realized up to 28% Sn content, demonstrating systematic lattice expansion key to altering the energy gap. XPS analysis indicates proportional amounts of Ge and Sn both on the surface and in the core of the nanocrystals. Deconvolution of the Ge (3d) and Sn (3d) suggests multiple bonding modes of surface atoms related to metal-amine and metal-akyl bonds. Elemental line scans and maps acquired through STEM-EDS confirmed a homogeneous distribution of Ge and Sn throughout the nanocrystals supporting the XRD and XPS results. Diffuse reflectance measurements confirmed the reduction in energy gap in $Ge_{1-x}Sn_x$ nanocrystals (0.26 eV @ 28% Sn) with respect to pure Ge (0.67 eV) suggesting minimal to no quantum confinement in 15-23 nm size regime.

To induce significant confinement effects, it was necessary to study even smaller $Ge_{1-x}Sn_x$ nanocrystals. $Ge_{1-x}Sn_x$ nanocrystals in the range of 3.4 - 4.6 nm were prepared with compositions ranging from 0-12% Sn. Cubic alloy structure was confirmed with XRD and narrow size distribution determined through TEM. Both solution and solid state absorption spectra show a significant increase in energy gap with respect to that of pure bulk Ge. Full analysis of the energy-gaps revealed that even in

141

the confinement size regime, the effect of Sn alloying still caused pronounced red shifting of absorption onset. Gap energies of the 3.4 - 4.6 nm nanocrystals (0.75-1.29 eV for 0- 9 %Sn) were determined by Kubelka-Munk converted diffuse reflectance. Further analysis was performed by applying the Tauc equations for both direct and indirect bandgaps resulting in energy gaps of 0.95-1.4eV and 0.75-1.31eV, respectively. Tauc analysis is not truly appropriate for determining between indirect and direct bandgaps, especially in the case of quantized energy levels in quantum confined nanocrystals. However, an interesting cross over is noted from the indirect equation predicting lower energy gaps from 0-5.6 %Sn to the direct gap equation predicting lower gaps when the composition exceeded 7.7 %Sn. The significance of this trend change is that, even if just coincidental, it occurs in at the same composition range that theoretical and experimental studies on $Ge_{1-x}Sn_x$ alloy thin films undergo a transition from indirect to direct bandgap. Unfortunately, little success was made in determining the luminescent properties of the 3.4-4.6 nm $Ge_{1-x}Sn_x$ nanocrystals. This can be attributed to a combination of low success rates of luminescence and fairly low quantum yields.

To further explore the effects of quantum confinement an even smaller set of $Ge_{1-x}Sn_x$ nanocrystals was produced. Narrowly dispersed ultra-small $Ge_{1-x}Sn_x$ nanocrystals (1.5-2.2 nm) with compositions in the range of 1.8-23 %Sn, exhibiting absorption and emission in the visible region for the first-time. Kubelka-Munk analysis predicted energy gaps of 2.16-1.5 eV (x = 0.018-0.23), however Sn induced red-shifting was only seen in the nanocrystals with 23 %Sn by this method. Photoluminescence is a far more reliable method to determine energy-gaps and indicate that there is still systematic red-shifting even in such a strong confinement region. The PL

measurements indicate gaps of 1.72-2.05 eV for x = 0.018-0.23 at room temperature with incremental red-shifting as Sn concentration increases. These measurements were in close agreement with energy-gaps calculated through theoretical calculations. To better understand the fine structure of the energy-gaps and probe the carrier dynamic further spectroscopic studies were conducted. In addition to the room temperature measurements, steady state PL was conducted at 15 K. At low temperatures, the PL range was 1.61-1.88 eV with decay lifetimes of 3-27 µs. The decay times at 15 K are 3 orders of magnitude slower than those at room temperature (9-28 ns). The temperature dependence on PL lifetimes is likely due to spin forbidden dark states which are overcome by thermal activation of bright excitons at room temperature.

While significant progress has been made in the field of $Ge_{1-x}Sn_x$ nanostructure research since the onset of this project, these studies are still in their infancy. The synthetic methodology should be improved with a focus on reducing size dispersity at all size ranges. Narrower size dispersity will enable more precise analysis of both size and composition relationships for better understanding of energy-gaps and carrier dynamics. Developing strategies for enhanced surface functionality are already underway. Better surface passivation will help improve emission efficiency and elucidate PL properties for not only the ultra-small nanocrystals but also the larger nanocrystals. One of the most prolific ways of improving surface passivation is through core-shelling with a compatible material to eliminate dangling bonds. However, selecting a shell material for $Ge_{1-x}Sn_x$ alloy nanocrystals is not trivial. Many common shell materials include Group VI anions, which are highly reactive with both Ge and Sn and will likely etch the particles instead of

depositing on the surface. Oxide based shells such as SiO_2 can be applied for fundamental studies but their insulating properties will not prevent use in devices.

Since the ultimate goal of studying $Ge_{1-x}Sn_x$ nanocrystal is for application in semiconducting devices, all current methods for film assembly should be considered and explored. All inorganic ligand systems are one of the more recent developments in semiconductor nanocrystal research. They have been shown to improve carrier transport in thin film devices by providing a conductive cross linking between particles. By adapting this technique early in the development of $Ge_{1-x}Sn_x$ nanocrystals it will greatly expedite our understanding of the system and application into devices.

To further explore the effects of quantum confinement an even smaller set of $Ge_{1-x}Sn_x$ nanocrystals was produced. Narrowly dispersed ultra-small $Ge_{1-x}Sn_x$ nanocrystals (1.5-2.2 nm) with compositions in the range of 1.8-23 %Sn exhibited for the first-time absorption and emission in the visible region. Kubelka-Munk analysis predicted energy gaps of 2.16-1.5 eV, however Sn induced red-shifting was only seen in the nanocrystals with 23 %Sn by this method. Photoluminescence is a far more reliable method to determine energy-gaps and indicate that there is still systematic red-shifting even in such a strong confinement region. The PL measurements indicate gaps of 1.72-2.05 eV at room temperature with incremental red-shifting as Sn concentration increases. These measurements were in close agreement with energy-gaps calculated through theoretical calculations. To better understand the fine structure of the energy-gaps and probe the carrier dynamic further spectroscopic studies were conducted. In addition to the room temperature measurements, steady state PL was conducted at 15K. At low temperatures, the PL range was 1.61-1.88 eV with decay lifetimes of 3-27

144

µs. The decay times at 15 K are 3 orders of magnitude slower than those at room temperature (9-28 ns). The temperature dependence on PL lifetimes is likely due to spin forbidden dark states which are overcome by thermal activation at room temperature.

While significant progress has been made in the field of $Ge_{1-x}Sn_x$ nanostructure research since the onset of this project, these studies are still in their infancy. The synthetic methodology should be improved with a focus on reducing size dispersity at all size ranges. Narrower size dispersity will enable more precise analysis of both size and composition relationships for a better understanding energy-gaps and carrier dynamics. Developing strategies for enhanced surface functionality are already underway. Better surface passivation will help improve emission efficiency and help elucidate PL properties for not only the ultra-small nanocrystals but also the larger nanocrystals. One of the most prolific ways of improving surface passivation is through core-shelling with a compatible material to eliminate dangling bonds. However, selecting a shell material for $Ge_{1-x}Sn_x$ alloy nanocrystals is not trivial.[40, 144] Many common shell materials include Group VI anions, which are highly reactive with both Ge and Sn and will likely etch the particles instead of depositing on the surface. Oxide based shells such as SiO_2 can be applied for fundamental studies but their insulating properties will not prevent use in devices.

Since the ultimate goal of studying $Ge_{1-x}Sn_x$ nanocrystal is for application in semiconducting devices, all current methods for film assembly should be considered and explored. All inorganic ligand systems are one of the more recent developments in semiconductor nanocrystal research.[145] They have been shown to improve carrier transport in thin film devices by providing a conductive cross linking between particles.

By adapting this technique early in the development of $Ge_{1-x}Sn_x$ nanocrystals it will greatly expedite our understanding of the system and application into devices.

References

1.   Claeys, C.; Simoen, E., *Germanium-Based Technologies From Materials to Devices*. Elsevier: Oxford, UK, 2007; p 449.

2.   Sze, S. M., *Physics of Semiconductor Devices*. 2nd ed.; John Wiley & Sons: New York, NY, 1981.

3.   Sze, S. M., *Semiconductor Devices: Physics and Technology*. John Wiley & Sons: New York, NY, 1985; p 523.

4.   Moore, G. E., Cramming More Components onto Integrated Circuits. *Proc. IEEE* **1965,** *86*, 82-85.

5.   Kamata, Y., High-k/Ge MOSFETs for Future Nanoelectronics. *Mater. Today* **2008,** *11*, 30-38.

6.   Franklin, A. D., Nanomaterials in Transistors: From High-performance to Thin-film Applications. *Science* **2015,** *349*, 10.

7.   Liddle, J. A.; Gallatin, G. M., Nanomanufacturing: A Perspective. *ACS Nano* **2016,** *10*, 2995-3014.

8.   Trindade, T.; O'Brien, P.; Pickett, N. L., Nanocrystalline Semiconductors: Synthesis, Properties, and Perspectives. *Chem. Mater.* **2001,** *13*, 3843-3858.

9.   Pankove, J. I., *Optical Processes in Semiconductors*. Dover Publications: New York, 1971; p 422.

10.   Smith, A. M.; Nie, S. M., Semiconductor Nanocrystals: Structure, Properties, and Band Gap Engineering. *Acc. Chem. Res.* **2010,** *43*, 190-200.

11.   Dietert, R. R.; Lee, J. E.; Hussain, I.; Piepenbrink, M., Developmental Immunotoxicology of Lead. *Toxicol. Appl. Pharmacol.* **2004,** *198*, 86-94.

12.   Fan, J.; Chu, P. K., Group IV Nanoparticles: Synthesis, Properties, and Biological Applications. *Small* **2010,** *6*, 2080-2098.

13.   Walling, M. A.; Novak, J. A.; Shepard, J. R. E., Quantum Dots for Live Cell and In Vivo Imaging. *Int. J. Mol. Sci.* **2009,** *10*, 441-491.

14.   He, G.; Atwater, H. A., Interband Transitions in Sn_xGe-x Alloys. *Phys. Rev. Lett.* **1997,** *79*, 1937-1940.

15.   Ragan, R.; Min, K. S.; Atwater, H. A., Direct Energy Gap Group IV Semiconductor Alloys and Quantum Dot Arrays in Sn_xGe_{1-x}/Ge and Sn_xSi_{1-x}/Si Alloy Systems. *Mater. Sci. Eng., B* **2001,** *87*, 204-213.

16.   Wirths, S.; Tiedemann, A. T.; Ikonic, Z.; Harrison, P.; Hollaender, B.; Stoica, T.; Mussler, G.; Myronov, M.; Hartmann, J. M.; Gruetzmacher, D.; Buca, D.; Mantl, S., Band Engineering and Growth of Tensile Strained Ge/(Si)GeSn Heterostructures for Tunnel Field Effect Transistors. *Appl. Phys. Lett.* **2013,** *102*, 192103/1- 192103/4.

17.   Sun, X.; Liu, J.; Kimerling, L. C.; Michel, J., Direct Gap Photoluminescence of n-type Tensile-Strained Ge-on-Si. *Appl. Phys. Lett.* **2009,** *95*, 011911/1-011911/3.

18.   Liu, J.; Sun, X.; Pan, D.; Wang, X.; Kimerling, L. C.; Koch, T. L.; Michel, J., Tensile-Strained, n-type Ge as a Gain Medium for Monolithic Laser Integration on Si. *Opt. Express* **2007,** *15*, 11272-11277.

19.   Denton, A. R.; Ashcroft, N. W., Vegard Law. *Phys. Rev. A* **1991,** *43*, 3161-3164.

20.   Jenkins, D. W.; Dow, J. D., Electronic-Properties of Metastable Ge_xSn_{1-x} Alloys. *Phys. Rev. B* **1987,** *36*, 7994-8000.

21.   Mader, K. A.; Baldereschi, A.; Vonkanel, H., Band-structure and Instability of $Ge_{1-x}Sn_x$ Alloys Alloys. *Solid State Commun.* **1989,** *69*, 1123-1126.

22.   Eckhardt, C.; Hummer, K.; Kresse, G., Indirect-to-direct Gap Transition in Strained and Unstrained Sn_xGe_{1-x} Alloys. *Phys. Rev. B* **2014,** *89*, 165201/1-165201/9.

23.   Gupta, S.; Chen, R.; Huang, Y.; Kim, Y.; Sanchez, E.; Harris, J. S.; Saraswat, K. C., Highly Selective Dry Etching of Germanium over Germanium-Tin ($Ge_{1-x}Sn_x$): A Novel Route for $Ge_{1-x}Sn_x$ Nanostructure Fabrication. *Nano Lett.* **2013,** *13*, 3783-3790.

24.   Gupta, S.; Magyari-Koepe, B.; Nishi, Y.; Saraswat, K. C., Achieving Direct Band Gap in Germanium Through Integration of Sn Alloying and External Strain. *J. Appl. Phys.* **2013,** *113*, 073707/1-073707/7.

25.   Chen, R.; Lin, H.; Huo, Y.; Hitzman, C.; Kamins, T. I.; Harris, J. S., Increased Photoluminescence of Strain-reduced, High-Sn Composition $Ge_{1-x}Sn_x$ Alloys Grown by Molecular Beam Epitaxy. *Appl. Phys. Lett.* **2011,** *99*, 181125/1-181125/3.

26.   Yin, W.; Gong, X.; Wei, S., Origin of the Unusually Large Band-gap Bowing and the Breakdown of the Band-edge Distribution Rule in the $Sn_{(x)}Ge_{(1-x)}$ Alloys. *Phys. Rev. B* **2008,** *78*, 161203/1-161203/4.

27.   de Guevara, H. P. L.; Rodriguez, A. G.; Navarro-Contreras, H.; Vidal, M. A., Nonlinear Behavior of the Energy Gap in $Ge_{1-x}Sn_x$ alloys at 4 K. *Appl. Phys. Lett.* **2007,** *91*, 161909/1-161909/3.

28.   D'Costa, V. R.; Cook, C. S.; Birdwell, A. G.; Littler, C. L.; Canonico, M.; Zollner, S.; Kouvetakis, J.; Menendez, J., Optical Critical Points of Thin-film $Ge_{1-y}Sn_y$ Alloys: A Comparative $Ge_{1-y}Sn_y/Ge_{1-x}Si_x$ Study. *Phys. Rev. B* **2006,** *73*, 125207/1-125207/16.

29.   Tolle, J.; Chizmeshya, A. V. G.; Fang, Y. Y.; Kouvetakis, J.; D'Costa, V. R.; Hu, C. W.; Menendez, J.; Tsong, I. S. T., Low Temperature Chemical Vapor Deposition of

Si-based Compounds via $SiH_3SiH_2SiH_3$: Metastable SiSn/GeSn/Si(100) Heteroepitaxial Structures. *Appl. Phys. Lett.* **2006,** *89*, 231924/1-231924/3.

30.   Lee, M.; Liu, P.; Hong, Y.; Chou, Y.; Hong, J.; Siao, Y., Electronic Band Structures of $Ge_{1-x}Sn_x$ Semiconductors: A First-principles Density Functional Theory Study. *J. Appl. Phys.* **2013,** *113*, 063517/1-063517/5.

31.   Yahyaoui, N.; Sfina, N.; Lazzari, J. L.; Bournel, A.; Said, M., Wave-function Engineering and Absorption Spectra in $Si_{0.16}Ge_{0.84}/Ge_{0.94}Sn_{0.06}/Si_{0.16}Ge_{0.84}$ Strained on Relaxed $Si_{0.10}Ge_{0.90}$ Type I Quantum Well. *J. Appl. Phys.* **2014,** *115*, 033109/1-033109/9.

32.   Min, K. S.; Atwater, H. A., Ultrathin Pseudomorphic Sn/Si and Sn_xSi_{1-x}/Si Heterostructures. *Appl. Phys. Lett.* **1998,** *72*, 1884-1886.

33.   He, G.; Atwater, H. A., Synthesis of Epitaxial Sn_xGe_{1-x} Alloy Films by Ion-assisted Molecular Beam Epitaxy. *Appl. Phys. Lett.* **1996,** *68*, 664-666.

34.   Chen, R.; Gupta, S.; Huang, Y. C.; Huo, Y. J.; Rudy, C. W.; Sanchez, E.; Kim, Y.; Kamins, T. I.; Saraswat, K. C.; Harris, J. S., Demonstration of a Ge/GeSn/Ge Quantum-Well Microdisk Resonator on Silicon: Enabling High-Quality Ge(Sn) Materials for Micro- and Nanophotonics. *Nano Lett.* **2014,** *14*, 37-43.

35.   Virgilio, M.; Manganelli, C. L.; Grosso, G.; Schroeder, T.; Capellini, G., Photoluminescence, Recombination Rate, and Gain Spectra in Optically Excited n-type and Tensile Strained Germanium Layers. *J. Appl. Phys.* **2013,** *114*.

36.   Lin, H.; Chen, R.; Lu, W.; Huo, Y.; Kamins, T. I.; Harris, J. S., Investigation of the Direct Band Gaps in $Ge_{1-x}Sn_x$ Alloys with Strain Control by Photoreflectance Spectroscopy. *Appl. Phys. Lett.* **2012,** *100*, 102109/1-102109/4.

37.   Gencarelli, F.; Vincent, B.; Demeulemeester, J.; Vantomme, A.; Moussa, A.; Franquet, A.; Kumar, A.; Bender, H.; Meersschaut, J.; Vandervorst, W.; Loo, R.; Caymax, M.; Temst, K.; Heyns, M., Crystalline Properties and Strain Relaxation Mechanism of CVD Grown GeSn. *ECS J. Solid State Sci. Technol.* **2013,** *2*, 134-137.

38.   Cheng, T. H.; Ko, C. Y.; Chen, C. Y.; Peng, K. L.; Luo, G. L.; Liu, C. W.; Tseng, H. H., Competitiveness Between Direct and Indirect Radiative Transitions of Ge. *Appl. Phys. Lett.* **2010,** *96*.

39.   Cheng, T. H.; Peng, K. L.; Ko, C. Y.; Chen, C. Y.; Lan, H. S.; Wu, Y. R.; Liu, C. W.; Tseng, H. H., Strain-enhanced Photoluminescence From Ge Direct Transition. *Appl. Phys. Lett.* **2010,** *96*.

40.   Guo, Y. J.; Rowland, C. E.; Schaller, R. D.; Vela, J., Near-Infrared Photoluminescence Enhancement in Ge/CdS and Ge/ZnS Core/Shell Nanocrystals: Utilizing IV/II-VI Semiconductor Epitaxy. *ACS Nano* **2014,** *8*, 8334-8343.

41.   Wang, B.; Ouyang, G.; Yang, Y. H.; Yang, G. W., Anomalous Thermal Stability of Cubic Tin Confined in a Nanotube. *Appl. Phys. Lett.* **2007,** *90*, 121908/1-121905/3.

42.   Lavine, C. F.; Ewald, A. W., 2-Band Galvanomagnetic Effects In Gray Tin. *J. Phys. and Chem. Solids* **1971,** *32*, 1121-1140.

43.   Lee, M.; Liu, P.; Hong, Y.; Chou, Y.; Hong, J.; Siao, Y., Electronic Band Structures of $Ge_{1-x}Sn_x$ Semiconductors: A First-principles Density Functional Theory Study. *J. Appl. Phys.* **2013,** *113*, 063517/1-063517/5.

44.   Eckhardt, C.; Hummer, K.; Kresse, G., Indirect-to-direct Gap Transition in Strained and Unstrained Sn_xGe_{1-x} Alloys. *Phys. Rev. B* **2014,** *89*, 165201/1-165201/9.

45.   Liu, J. J.; Yang, W. T.; Li, Y. C.; Fan, L. Z.; Li, Y. F., Electrochemical Studies of the Effects of the Size, Ligand and Composition on the Band Structures of CdSe, CdTe and their Alloy Nanocrystals. *Phys. Chem. Chem. Phys.* **2014,** *16*, 4778-4788.

46.   Nguyen, T. T. N.; He, J. L., Preparation of Titanium Monoxide Nanopowder by Low-energy Wet Ball-milling. *Adv. Powder Technol.* **2016,** *27*, 1868-1873.

47.   Enayati, M. H.; Mohamed, F. A., Application of Mechanical Alloying/Milling for Synthesis of Nanocrystalline and Amorphous Materials. *Int. Mater. Rev.* **2014,** *59*, 394-416.

48.   Swihart, M. T., Vapor-phase Synthesis of Nanoparticles. *Curr. Opin. Colloid Interface Sci.* **2003,** *8*, 127-133.

49.   Thanh, N. T. K.; Maclean, N.; Mahiddine, S., Mechanisms of Nucleation and Growth of Nanoparticles in Solution. *Chem. Rev.* **2014,** *114*, 7610-7630.

50.   Ismail, R. A.; Sulaiman, G. M.; Abdulrahman, S. A., Preparation of Iron Oxide Nanoparticles by Laser Ablation in DMF Under Effect of External Magnetic Field. *Int. J. Mod. Phys. B* **2016,** *30*, 1650094/1- 1650094/ 8.

51.   Cho, Y. J.; Kim, C. H.; Im, H. S.; Myung, Y.; Kim, H. S.; Back, S. H.; Lim, Y. R.; Jung, C. S.; Jang, D. M.; Park, J.; Lim, S. H.; Cha, E. H.; Bae, K. Y.; Song, M. S.; Il Cho, W., Germanium-tin Alloy Nanocrystals for High-performance Lithium Ion Batteries. *Phys. Chem. Chem. Phys.* **2013,** *15*, 11691-11695.

52.   Chen, W. H.; Cabarrocas, P. R. I., Insights Into Gold-catalyzed Plasma-Assisted CVD Growth of Silicon Nanowires. *Appl. Phys. Lett.* **2016,** *109*, 043108-1 - 043108-4.

53.   Guo, S. J.; Wang, E. K., Noble Metal Nanomaterials: Controllable synthesis and Application in Fuel Cells and Analytical Sensors. *Nano Today* **2011,** *6*, 240-264.

54.   Banadaki, A. D.; Kajbafvala, A., Recent Advances in Facile Synthesis of Bimetallic Nanostructures: An Overview. *J. Nanomat.* **2014,** *2014*, 28.

55.   Zhu, C. Z.; Du, D.; Eychmuller, A.; Lin, Y. H., Engineering Ordered and Nonordered Porous Noble Metal Nanostructures: Synthesis, Assembly, and Their Applications in Electrochemistry. *Chem. Rev.* **2015,** *115*, 8896-8943.

56.   Biswas, S.; Doherty, J.; Saladukha, D.; Ramasse, Q.; Majumdar, D.; Upmanyu, M.; Singha, A.; Ochalski, T.; Morris, M. A.; Holmes, J. D., Non-equilibrium Induction of Tin in Germanium: Towards Direct Bandgap $Ge_{1-x}Sn_x$ Nanowires. *Nat. Commun.* **2016,** *7*.

57.   Hafiz, S. A.; Esteves, R. J. A.; Demchenko, D. O.; Arachchige, I. U.; Ozgur, U., Energy Gap Tuning and Carrier Dynamics in Colloidal $Ge_{1-x}Sn_x$ Quantum Dots. *J. Phys. Chem. Lett.* **2016,** *7*, 3295-3301.

58.   Barth, S.; Seifner, M. S.; Bernardi, J., Microwave-assisted Solution-liquid-solid Growth of $Ge_{1-x}Sn_x$ Nanowires with High Tin Content. *Chem. Commun.* **2015,** *51*, 12282-12285.

59.   Esteves, R. J.; Ho, M. Q.; Arachchige, I. U., Nanocrystalline Group IV Alloy Semiconductors: Synthesis and Characterization of $Ge_{1-x}Sn_x$ Quantum Dots for Tunable Bandgaps. *Chem. Mater.* **2015,** *27*, 1559-1568.

60.   Seifner, M. S.; Biegger, F.; Lugstein, A.; Bernardi, J.; Barth, S., Microwave-Assisted $Ge_{1-x}Sn_x$, Nanowire Synthesis: Precursor Species and Growth Regimes. *Chem. Mater.* **2015,** *27*, 6125-6130.

61.   Ruddy, D. A.; Erslev, P. T.; Habas, S. E.; Seabold, J. A.; Neale, N. R., Surface Chemistry Exchange of Alloyed Germanium Nanocrystals: A Pathway Toward Conductive Group IV Nanocrystal Films. *J. Phys. Chem. Lett.* **2013,** *4*, 416-421.

62.   Esteves, R. J. A.; Hafiz, S. A.; Demchenko, D. O.; Ozgur, U.; Arachchige, I. U., Ultra-small $G_{1-x}Sn_x$ Quantum Dots with Visible Photoluminscence. *Chem. Commun.* **2016,** *56*, 11665-11668.

63.   Ramasamy, K.; Kotula, P. G.; Fidler, A. F.; Brumbach, M. T.; Pietryga, J. M.; Ivanov, S. A., Sn_xGe_{1-x} Alloy Nanocrystals: A First Step toward Solution-Processed Group IV Photovoltaics. *Chem. Mater.* **2015,** *27*, 4640-4649.

64.   Ruddy, D. A.; Johnson, J. C.; Smith, E. R.; Neale, N. R., Size and Bandgap Control in the Solution-Phase Synthesis of Near-Infrared-Emitting Germanium Nanocrystals. *ACS Nano* **2010,** *4*, 7459-7466.

65.   Lee, D. C.; Pietryga, J. M.; Robel, I.; Werder, D. J.; Schaller, R. D.; Klimov, V. I., Colloidal Synthesis of Infrared-Emitting Germanium Nanocrystals. *J. Am. Chem. Soc.* **2009,** *131*, 3436-3437.

66.   Lee, M., *X-Ray Diffraction for Materials Research*. Apple Academic Press Inc.: Oakville, ON, 2016; p 289.

67.   Cullity, B. D., Elements of X-ray Diffraction. Addison-Wesley Publishing Company, Inc.: Reading, MA, 1956; p 514.

68.   Williams, D. B.; Carter, C. B., *Transmission Electron Microscopy A Textbook for Materials Science*. Plenum Press: New York, NY, 1996; p 729.

69.   Van Der Heide, P., *X-ray Photoelectron Spectroscopy An Introduction to Principles and Practices*. John Wiley & Sons, Inc.: Hoboken, NJ, 2012; p 241.

70.   Aroca, R., *Surface-Enhanced Vibrational Spectroscopy*. John Wiley & Sons Ltd: West Sussex, England, 2006; p 233.

71.   Tsuge, A.; Uwamino, Y.; Ishizuka, T.; Suzuki, K., Quantitative-Analysis of Powdery Sample by Diffuse Reflectance Infrared Fourier-Transform Spectrometry - Determination of the a-Component in Silicon-Nitride. *Appl. Spectrosc.* **1991,** *45*, 1377-1380.

72.   Nowak, M.; Kauch, B.; Szperlich, P., Determination of Energy Band Gap of Nanocrystalline SbSI Using Diffuse Reflectance Spectroscopy. *Rev. Sci. Instrum.* **2009,** *80*, 046107/1-046107/3.

73.   Tauc, J.; Grigorov.R; Vancu, A., Optical Properties and Electronic Structure of Amourphous Germanium. *Physica Status Solidi* **1966,** *15*, 627-637.

74.   Klimov, V. I., *Nanocrystal Quantum Dots*. 2nd ed.; Taylor and Francis Group, LLC: Boca Raton, FL, **2010**; p 469.

75.   Sahu, A.; Kang, M. S.; Kompch, A.; Notthoff, C.; Wills, A. W.; Deng, D.; Winterer, M.; Frisbie, C. D.; Norris, D. J., Electronic Impurity Doping in CdSe Nanocrystals. *Nano Lett.* **2012,** *12*, 2587-2594.

76.   Crooker, S. A.; Barrick, T.; Hollingsworth, J. A.; Klimov, V. I., Multiple Temperature Regimes of Radiative Decay in CdSe Nanocrystal Quantum Dots: Intrinsic Limits to the Dark-exciton Lifetime. *Appl. Phys. Lett.* **2003,** *82*, 2793-2795.

77.   Arachchige, I. U.; Kanatzidis, M. G., Anomalous Band Gap Evolution from Band Inversion in $Pb_{1-x}Sn_xTe$ Nanocrystals. *Nano Lett.* **2009,** *9*, 1583-1587.

78.	Arachchige, I. U.; Mohanan, J. L.; Brock, S. L., Sol-Gel Processing of Semiconducting Metal Chalcogenide Xerogels: Influence of Dimensionality on Quantum Confinement Effects in a Nanoparticle Network. *Chem. Mater.* **2005,** *17*, 6644-6650.

79.	Mensik, M.; Kral, K., Power-law Photoluminescence Decay in Indirect Gap Quantum Dots. *Microelectron. Eng.* **2013,** *111*, 170-174.

80.	Seker, F.; Meeker, K.; Kuech, T. F.; Ellis, A. B., Surface Chemistry of Prototypical Bulk II-VI and III-V Semiconductors and Implications for Chemical Sensing. *Chem. Rev.* **2000,** *100*, 2505-2536.

81.	Vandervelde, T. E.; Krishna, S., Progress and Prospects for Quantum Dots in a Well Infrared Photodetectors. *J. Nanosci. Nanotechnol.* **2010,** *10*, 1450-1460.

82.	Ellingson, R. J.; Beard, M. C.; Johnson, J. C.; Yu, P. R.; Micic, O. I.; Nozik, A. J.; Shabaev, A.; Efros, A. L., Highly Efficient Multiple Exciton Generation in Colloidal PbSe and PbS Quantum Dots. *Nano Lett.* **2005,** *5*, 865-871.

83.	Duan, H.; Jiang, Y.; Zhang, Y.; Sun, D.; Liu, C.; Huang, J.; Lan, X.; Zhou, H.; Chen, L.; Zhong, H., High Quantum-yield $CdSe_xS_{1-x}$/ZnS Core/shell Quantum Dots for Warm White Light-emitting Diodes with Good Color Rendering. *Nanotechnology* **2013,** *24*, 285201/1-285201/9.

84.	Lee, Y.; Cho, S. B.; Chung, Y., Tunable Indirect to Direct Band Gap Transition of Monolayer Sc_2CO_2 by the Strain Effect. *ACS Appl. Mater. Interfaces* **2014,** *6*, 14724-14728.

85.	Conley, H. J.; Wang, B.; Ziegler, J. I.; Haglund, R. F. J.; Pantelides, S. T.; Bolotin, K. I., Bandgap Engineering of Strained Monolayer and Bilayer MoS_2. *Nano Lett.* **2013,** *13*, 3626-3630.

86.   Cheng, R.; Wang, W.; Gong, X.; Sun, L. F.; Guo, P. F.; Hu, H. L.; Shen, Z. X.; Han, G. Q.; Yeo, Y. C., Relaxed and Strained Patterned Germanium-Tin Structures: A Raman Scattering Study. *ECS J. Solid State Sci. Technol.* **2013,** *2*, 138-145.

87.   Low, K. L.; Yang, Y.; Han, G.; Fan, W.; Yeo, Y., Electronic Band Structure and Effective Mass Parameters of $Ge_{1-x}Sn_x$ Alloys. *J. Appl. Phys.* **2012,** *112*, 103715/1-103715/9.

88.   Yang, Y.; Low, K. L.; Wang, W.; Guo, P.; Wang, L.; Han, G.; Yeo, Y., Germanium-tin n-channel Tunneling Field-effect Transistor: Device Physics and Simulation Study. *J. Appl. Phys.* **2013,** *113*, 194507/1-194507/7.

89.   Holman, Z. C.; Liu, C.; Kortshagen, U. R., Germanium and Silicon Nanocrystal Thin-Film Field-Effect Transistors from Solution. *Nano Lett.* **2010,** *10*, 2661-2666.

90.   Pillarisetty, R., Academic and Industry Research Progress in Germanium Nanodevices. *Nature* **2011,** *479*, 324-328.

91.   Assefa, S.; Xia, F.; Vlasov, Y. A., Reinventing Germanium Avalanche Photodetector for Nanophotonic On-chip Optical Interconnects. *Nature* **2010,** *464*, 80-91.

92.   Vaughn II, D. D.; Bondi, J. F.; Schaak, R. E., Colloidal Synthesis of Air-Stable Crystalline Germanium Nanoparticles with Tunable Sizes and Shapes. *Chem. Mater.* **2010,** *22*, 6103-6108.

93.   Borchert, H.; Shevehenko, E. V.; Robert, A.; Mekis, I.; Kornowski, A.; Grubel, G.; Weller, H., Determination of Nanocrystal Sizes: A Comparison of TEM, SAXS, and XRD Studies of Highly Monodisperse $COPt_3$ Particles. *Langmuir* **2005,** *21*, 1931-1936.

94.   Vaughn II, D. D.; Schaak, R. E., Synthesis, Properties and Applications of Colloidal Germanium and Germanium-based Nanomaterials. *Chem. Soc. Rev.* **2013,** *42*, 2861-2879.

95.   Kornowski, A.; Giersig, M.; Vogel, R.; Chemseddine, A.; Weller, H., Nanometer-Sized Colloidal Germanium Particles - Wet-Chemical Synthesis, Laser-Induced Crystallization and Particle Growth. *Adv. Mater.* **1993,** *5*, 634-636.

96.   Lu, X. M.; Korgel, B. A.; Johnston, K. P., High Yield of Germanium Nanocrystals Synthesized from Germanium Diiodide in Solution. *Chem. Mater.* **2005,** *17*, 6479-6485.

97.   Gerung, H.; Bunge, S. D.; Boyle, T. J.; Brinker, C. J.; Han, S. M., Anhydrous Solution Synthesis of Germanium Nanocrystals from the Germanium(II) Precursor Ge[N(SiMe$_3$)$_2$]$_2$. *Chem. Commun.* **2005**, 1914-1916.

98.   Chou, N. H.; Oyler, K. D.; Motl, N. E.; Schaak, R. E., Colloidal Synthesis of Germanium Nanocrystals Using Room-Temperature Benchtop Chemistry. *Chem. Mater.* **2009,** *21*, 4105-4107.

99.   Li, S. F.; Bauer, M. R.; Menendez, J.; Kouvetakis, J., Scaling Law for the Compositional Dependence of Raman Frequencies in SnGe and GeSi Alloys. *Appl. Phys. Lett.* **2004,** *84*, 867-869.

100.   Volodin, V. A.; Marin, D. V.; Sachkov, V. A.; Gorokhov, E. B.; Rinnert, H.; Vergnat, M., Applying an Improved Phonon Confinement Model to the Analysis of Raman Spectra of Germanium Nanocrystals. *J. Exp. Theor. Phys.* **2014,** *118*, 65-71.

101.   Naja, G.; Bouvrette, P.; Hrapovic, S.; Luong, J. H. T., Raman-based Detection of Bacteria using Silver Nanoparticles Conjugated with Antibodies. *Analyst* **2007,** *132*, 679-686.

102.   Lignie, A.; Menaert, B.; Armand, P.; Pena, A.; Debray, J.; Papet, P., Top Seeded Solution Growth and Structural Characterizations of alpha-Quartz-like Structure GeO$_2$ Single Crystal. *Cryst. Growth Des.* **2013,** *13*, 4220-4225.

103.   Lee, S.; Huang, S.; Conibeer, G.; Green, M., Lateral Growth of Ge Nanocrystals in a Thin Ge-rich Silicon Nitride Layer. *J. Cryst. Growth* **2013,** *383*, 36-42.

104.   Kalebaila, K. K.; Georgiev, D. G.; Brock, S. L., Synthesis and Characterization of Germanium Sulfide Aerogels. *J. Non-Cryst. Solids* **2006,** *352*, 232-240.

105.   Glidewell, C., Germanium-Carbon Versus Germanium-Nitrogen Double-Bond Formation in the Reactions Between Germylenes and Diazo Compounds. *Struct. Chem.* **1990,** *1*, 317-323.

106.   Palacios-Padros, A.; Caballero-Briones, F.; Diez-Perez, I.; Sanz, F., Tin Passivation in Alkaline Media: Formation of SnO Microcrystals as Hydroxyl Etching Product. *Electrochimi. Acta* **2013,** *111*, 837-845.

107.   Li, W.; Chen, Z.; Xu, L.; Yan, Y., A Solution-phase Synthesis Method to Highly Active Pt-Co/C Electrocatalysts for Proton Exchange Membrane Fuel Cell. *J. Power Sources* **2010,** *195*, 2534-2540.

108.   Aldakov, D.; Chappaz-Gillot, C.; Salazar, R.; Delaye, V.; Welsby, K. A.; Ivanova, V.; Dunstan, P. R., Properties of Electrodeposited CuSCN 2D Layers and Nanowires Influenced by their Mixed Domain Structure. *J. Phys. Chem. C* **2014,** *118*, 16095-16103.

109.   de Boer, W. D. A. M.; Timmerman, D.; Dohnalova, K.; Yassievich, I. N.; Zhang, H.; Buma, W. J.; Gregorkiewicz, T., Red Spectral Shift and Enhanced Quantum Efficiency in Phonon-free Photoluminescence from Silicon Nanocrystals. *Nat. Nanotechnol.* **2010,** *5*, 878-884.

110.   Biacchi, A. J.; Vaughn II, D. D.; Schaak, R. E., Synthesis and Crystallographic Analysis of Shape-Controlled SnS Nanocrystal Photocatalysts: Evidence for a Pseudotetragonal Structural Modification. *J. Am. Chem. Soc.* **2013,** *135*, 11634-11644.

111.   Zhang, H.; Bayne, M.; Fernando, S.; Legg, B.; Zhu, M.; Penn, R. L.; Banfield, J. F., Size-Dependent Bandgap of Nanogoethite. *J. Phys. Chem. C* **2011,** *115*, 17704-17710.

112.   Apopei, P.; Catrinescu, C.; Teodosiv, C.; Royer, S., Mixed-phase TiO2 photocatalysts: Crystalline Phase Isolation and Reconstruction, Characterization and Photocatalytic Activity in the Oxidation of 4-chlorophenol from Aqueous Effluents. *Appl. Catal., B* **2014,** *160*, 374-382.

113.   Ganguly, S.; Kazem, N.; Carter, D.; Kauzlarich, S. M., Colloidal Synthesis of an Exotic Phase of Silicon: The BC8 Structure. *J. Am. Chem. Soc* **2014,** *136,* 1296-1299.

114.   Prabakar, S.; Shiohara, A.; Hanada, S.; Fujioka, K.; Yamamoto, K.; Tilley, R. D., Size Controlled Synthesis of Germanium Nanocrystals by Hydride Reducing Agents and Their Biological Applications. *Chem. Mater.* **2010,** *22*, 482-486.

115.   Perdew, J. P.; Burke, K.; Ernzerhof, M., Generalized Gradient Approximation Made Simple. *Phys. Rev. Lett.* **1996,** *77*, 3865-3868.

116.   Blochl, P. E., Projector Augmented-wave Method. *Phys. Rev. B* **1994,** *50*, 17953-17979.

117.   Kresse, G.; Furthmuller, J., Efficient Iterative Schemes for Ab Initio Total-energy Calculations Using a Plane-wave Basis Set. *Phys. Rev. B* **1996,** *54*, 11169-11186.

118.   Jaouen, T.; Aebi, P.; Tricot, S.; Delhaye, G.; Lepine, B.; Sebilleau, D.; Jezequel, G.; Schieffer, P., Induced Work Function Changes at Mg-doped MgO/Ag(001)

Interfaces: Combined Auger Electron Diffraction and Density Functional Study. *Phys. Rev. B* **2014,** *90*, 11.

119.   Briggs, D.; Seah, P. M., *Practical Surface Analysis*. 2nd ed.; John Wiley & Sons: Great Britain, 1948; Vol. 1, Auger and X-ray photoelectron spectroscopy.

120.   Nolan, B. M.; Chan, E. K.; Zhang, X.; Muthuswamy, E.; Benthem K.; Kauzlarich, S. M., Sacrificial Silver Nanoparticles: Reducing GeI_2 To Form Hollow Germanium Nanoparticles by Electroless Deposition. *ACS Nano* **2016,** *10*, 5391-5397.

121.   Tonkikh, A. A.; Eisenschmidt, C.; Talalaev, V. G.; Zakharov, N. D.; Schilling, J.; Schmidt, G.; Werner, P., Pseudomorphic GeSn/Ge(001) Quantum Wells: Examining Indirect Band Gap Bowing. *Appl. Phys. Lett.* **2013,** *103*, 032106/1-032106/5.

122.   Ceperley, D. M.; Alder, B. J., Ground-state of the Electron-gas by a Stochastic Method. *Phys. Rev. Lett.* **1980,** *45*, 566-569.

123.   Heyd, J.; Scuseria, G. E.; Ernzerhof, M., Hybrid functionals based on a screened Coulomb potential. *J. Chem. Phys.* **2003,** *118*, 8207-8215.

124.   Oehme, M.; Kaschel, M.; Werner, J.; Kirfel, O.; Schmid, M.; Bahouchi, B.; Kasper, E.; Schulze, J., Germanium on Silicon Photodetectors with Broad Spectral Range. *J. Electrochem. Soc.* **2010,** *157*, 144-148.

125.   Moskalyk, R. R., Review of Germanium Processing Worldwide. *Miner. Eng.* **2004,** *17*, 393-402.

126.   Cheng, T. H.; Liao, M. H.; Yeh, L.; Lee, I. L.; Liang, M. S.; Liu, C. W., Digital Communication Using Ge Metal-insulator-semiconductor Light-emitting Diodes and Photodetectors. *J. Appl. Phys.* **2008,** *103*, 016103/1- 016103/3.

127.   Lee, M.; Liu, P.; Hong, Y.; Chou, Y.; Hong, J.; Siao, Y., Electronic Band Structures of $Ge_{1-x}Sn_x$ Semiconductors: A first-principles Density Functional Theory Study. *J. Appl. Phys.* **2013,** *113*, 063517/1- 063517/5.

128.   Moontragoon, P.; Ikonic, Z.; Harrison, P., Band Structure Calculations of Si-Ge-Sn Alloys: Achieving Direct Band Gap Materials. *Semicond. Sci. Technol.* **2007,** *22*, 742-748.

129.   Du, W.; Ghetmiri, S. A.; Conley, B. R.; Mosleh, A.; Nazzal, A.; Soref, R. A.; Sun, G.; Tolle, J.; Margetis, J.; Naseem, H. A.; Yu, S.-Q., Competition of Optical Transitions Between Direct and Indirect Bandgaps in $Ge_{1-x}Sn_x$. *Appl. Phys. Lett.* **2014,** *105*, 051104/1- 051104/4.

130.   Mathews, J.; Beeler, R. T.; Tolle, J.; Xu, C.; Roucka, R.; Kouvetakis, J.; Menendez, J., Direct-gap Photoluminescence with Tunable Emission Wavelength in $Ge_{1-y}Sn_y$ Alloys on Silicon. *Appl. Phys. Lett.* **2010,** *97*, 221912/1- 221912/3.

131.   Kasper, E.; Werner, J.; Oehme, M.; Escoubas, S.; Burle, N.; Schulze, J., Growth of Silicon Based Germanium Tin Alloys. *Thin Solid Films* **2012,** *520*, 3195-3200.

132.   Paier, J.; Marsman, M.; Kresse, G., Dielectric Properties and Excitons for Extended Systems from Hybrid Functionals. *Phys. Rev. B* **2008,** *78*, 121201/1- 121201/4.

133.   Robel, I.; Shabaev, A.; Lee, D. C.; Schaller, R. D.; Pietryga, J. M.; Crooker, S. A.; Efros, A. L.; Klimov, V. I., Temperature and Magnetic-Field Dependence of Radiative Decay in Colloidal Germanium Quantum Dots. *Nano Lett.* **2015,** *15*, 2685-2692.

134.   Wen, X.; Zhang, P.; Smith, T. A.; Anthony, R. J.; Kortshagen, U. R.; Yu, P.; Feng, Y.; Shrestha, S.; Coniber, G.; Huang, S., Tunability Limit of Photoluminescence in Colloidal Silicon Nanocrystals. *Sci. Rep.* **2015,** *5*, 1-10.

135.   Poem, E.; Kodriano, Y.; Tradonsky, C.; Lindner, N. H.; Gerardot, B. D.; Petroff, P. M.; Gershoni, D., Accessing the Dark Exciton with Light. *Nat. Phys.* **2010,** *6*, 993-997.

136.   Scholes, G. D.; Rumbles, G., Excitons in Nanoscale Systems. *Nat. Mater.* **2006,** *5*, 683-696.

137.   Efros, A. L.; Rosen, M.; Kuno, M.; Nirmal, M.; Norris, D. J.; Bawendi, M., Band-edge Exciton in Quantum Dots of Semiconductors with a Degenerate Valence Band: Dark and Bright Exciton States. *Phys. Rev. B* **1996,** *54*, 4843-4856.

138.   Leung, K.; Whaley, K. B., Electron-hole Interactions in Silicon Nanocrystals. *Phys. Rev. B* **1997,** *56*, 7455-7468.

139.   Lavallard, P.; Chamarro, M.; Perez-Conde, J.; Bhattacharjee, A. K.; Goupalov, S. V.; Lipovskii, A. A., Exchange Interaction and Acoustical Phonon Modes in CdTe Nanocrystals. *Solid State Commun.* **2003,** *127*, 439-442.

140.   Franceschetti, A.; Zunger, A., Direct Pseudopotential Calculation of Exciton Coulomb and Exchange Energies in Semiconductor Quantum Dots. *Phys. Rev. Lett.* **1997,** *78*, 915-918.

141.   Bawendi, M. G.; Wilson, W. L.; Rothberg, L.; Carroll, P. J.; Jedju, T. M.; Steigerwald, M. L.; Brus, L. E., Electronic-Structure and Photoexcited-carrier Dynamics in Nanometer-size CdSe Clusters. *Phys. Rev. Lett.* **1990,** *65*, 1623-1626.

142.   Oneil, M.; Marohn, J.; McLendon, G., Dynamics of Electron-hole Pair Recombination in Semiconductors Clusters. *J. Phys. Chem.* **1990,** *94*, 4356-4363.

143.   Kigel, A.; Brumer, M.; Maikov, G. I.; Sashchiuk, A.; Lifshitz, E., Thermally

Activated Photoluminescence in Lead Selenide Colloidal Quantum Dots. *Small* **2009,** *5*,

1675-1681.

144.   Wang, G.; Ji, J.; Li, C.; Yu, L.; Duan, W.; Wei, W.; You, X.; Xu, X., Type-II Core-

shell Si-CdS Nanocrystals: Synthesis and Spectroscopic and Electrical Properties.

Chem. Commun. **2014,** *50*, 11922-11925.

145.   Kovalenko, M. V.; Scheele, M.; Talapin, D. V., Colloidal Nanocrystals with

Molecular Metal Chalcogenide Surface Ligands. *Science* **2009,** *324*, 1417-1420.

Vita

Richard J Alan Esteves

1620 Kemper St Richmond, VA 23220 • 973-214-1725 • estevesrj@vcu.edu

EDUCATION

Ph.D. Nanoscience and Nanotechnology, December, 2016 (expected); GPA 3.71
Virginia Commonwealth University, Richmond, VA
Dissertation: The Dawn of New Quantum Dots: Synthesis and Characterization of $Ge_{1-x}Sn_x$ Nanocrystals for Tunable Bandgaps.

Bachelor of Science, Chemistry; May 2011; GPA 3.24/3.50
Temple University, Philadelphia, PA

RESEARCH EXPERIENCE

Virginia Commonwealth University, Richmond VA
Graduate Research Assistant   **August 2011–December 2016**
Advisor: Prof. Indika U. Arachchige

Temple University, Philadelphia PA
Undergraduate Researcher   **September 2009-May 2011**
Advisor: Prof. Stephanie Wunder

TEACHING AND MANAGING EXPERIENCE

Virginia Commonwealth University, Department of Chemistry, Richmond VA
Graduate Lab Manager   **January 2012-December 2016**

Chemical Hygiene Officer   **January 2012-December 2015**

Teaching Assistant   **September 2011-May 2015**

AWARDS

- Graduate School Dissertation Assistantship Award, 2016.

PUBLICATIONS

(1) **Esteves, R. J**; Ho, M. Q.; Arachchige, I. U. Nanocrystalline Group IV Alloy Semiconductors: Synthesis and Characterization of $Ge_{1-x}Sn_x$ Quantum Dots for Tunable Bandgaps, *Chem. Mater.* **2015,** 27**,** 1559–1568.

(2) **Esteves, R. J**; Hafiz, S.; Demchenko, D. O.; Özgür, Ü.; Arachchige, I. U. Ultra-small $Ge_{1-x}Sn_x$ Quantum Dots with Visible Photoluminescence, *Chem. Commun.* **2016,** 52, 11665-11668.

(3) Tallapally, V.;≠ **Esteves, R. J;**≠ Nahar, L.; Arachchige, I. U. Nanocrystalline Multivariate Synthesis of Tin Phosphide Nanoparticles: Temperature, Time, and Ligand Control of Size, Shape, and Crystal Structure, *Chem. Mater.* **2016**, 28, 5406-5414. **(≠Co-first authored publication)**

(4) Shopan, H.; **Esteves, R. J**; Demchenko, D. O.; Özgür, Ü.; Arachchige, I. U. Energy Gap Tuning and Carrier Dynamics in Colloidal $Ge_{1-x}Sn_x$ Quantum Dots, *Phys. Chem. Lett.* **2016,** 7, 3295-3301.

(5) Sahoo, N. G.; **Esteves, R. J**; Punetha, V. D.; Pestov, D.; Arachchige, I. U.; McLeskey, J. T. Jr. Schottky Diodes from 2D Germanane, *Appl. Phys. Lett.* **2016,** 109, 023507/1 – 023507/4.

(6) Gao, X.; **Esteves R. J,** Nahar, L.; Nowaczyk, J.; Arachchige, I. U. Direct Cross-Linking of Au/Ag Alloy Nanoparticles into Monolithic Aerogels for Application in Surface-Enhanced Raman Scattering, *ACS, Appl. Mater. Interface,* **2016,** 8, 13076-13085.

(7) Nahar, L.; **Esteves, R. J**; Hafiz, S.; Özgür, Ü.; Arachchige, I. U. Metal−Semiconductor Hybrid Aerogels: Evolution of Optoelectronic Properties in a Low-Dimensional CdSe/Ag Nanoparticle Assembly *ACS Nano*, **2015,** 9, 9810-9821.

(8) Ho, M. Q.; **Esteves R. J,** Arachchige, I. U Size Dependent Optical Properties of Luminescent Zn_3P_2 Nanocrystals *J. Phys. Chem. C*, **2015,** 119, 10576-10584.

(9) Gao, X.; **Esteves R. J,** Luong, T. T. H.; Arachchige, I. U Oxidation-Induced Self-Assembly of Ag Nanoshells into Transparent and Opaque Ag Hydrogels and Aerogels, *J. Am. Chem. Soc.* **2014,** 136, 7993−8002.

CONFERENCES PRESENTATIONS

(1) **Esteves, R. J**; Hafiz, S.; Demchenko, D. O.; Özgür, Ü.; Arachchige, I. U. "Ultra-small $Ge_{1-x}Sn_x$ Quantum dots with Orange-Red Photoluminescence" *252th ACS National Meeting,* Philadelphia, PA, 08/21/16–08/25/16, *oral presentation.*

(2) **Esteves, R. J**; Hafiz, S.; Demchenko, D. O.; Özgür, Ü.; Arachchige, I. U. "Photoluminescence from Ultra-Small $Ge_{1-x}Sn_x$ Quantum Dots" *252th ACS National Meeting,* Philadelphia, PA, 08/21/16–08/25/16, *poster presentation.*

(3) **Esteves, R. J**; Hafiz, S.; Demchenko, D. O.; Özgür, Ü.; Arachchige, I. U. "Semiconductor Alloy Nanocrystals: Band Structure Evolution and Optoelectronic Properties" *International Symposium on Clusters and Nanomaterials 2015, Richmond, VA,* 10/26/15-10/29/15, *poster presentation.*

(4) **Esteves, R. J**; Arachchige, I. U. "Semiconducting Group IV Quantum Dots for Tunable Bandgaps" 250th ACS National Meeting, Boston, MA, 08/16/15-08/20/15, *oral presentation.*

(5) **Esteves R. J,** Arachchige, I. U. 'Bandgap Engineering of Germanium Nanoparticles through Tin Alloying and Quantum Confinement Effects" *South East Regional Meeting of American Chemical Society, 2013*, Atlanta, GA, 011/12/13-011/16/13, *oral presentation.*

(6) **Esteves R. J,** Arachchige, I. U. Composition Tunable Absorption and Emission Properties of $Ge_{1-x}Sn_x$ Alloy Nanocrystals *South East Regional Meeting of American Chemical Society 2012*, Raleigh, NC, 011/14/12-011/17/12, *poster presentation.*

COMMUNITY OUTREACH

- Provided nanoscience focused demonstrations to Richmond Public Schools high school students through a Summer Research Experience for Educators and Students program developed by Dr. Arachchige and a local high school science teacher Mr. Rajendra Jaini.

- <u>Assistant Scoutmaster</u>, Troop 444　　　　　　　　　　　　　　　**March 2013-Present**
  Boy Scouts of America, Richmond Va